Electronic Thesis and Dissertation Repository

12-15-2022 10:00 AM

Enhanced performance of 3D electroactive polymer transducers via hierarchical structures

Frederick B. Holness, *The University of Western Ontario*

Supervisor: Aaron D. Price, *The University of Western Ontario*
A thesis submitted in partial fulfillment of the requirements for the Doctor of Philosophy degree in Mechanical and Materials Engineering
© Frederick B. Holness 2022

Follow this and additional works at: https://ir.lib.uwo.ca/etd

Part of the Polymer and Organic Materials Commons

Recommended Citation

Abstract

Conjugated polymers (CPs) are a class of polymers that exhibit a change in size or shape in response to electrical stimuli. The unique combination of electrical and mechanical properties facilitates the fabrication of novel devices in a broad range of applications including: sensors, actuators, and lab-on-a-chip systems. The alternating single and double bonds along the polymer chain of CPs enables their electroactive properties but is also responsible for processability associated with CPs that has limited fabrication methods. Recently, a photosensitive CP composite enabling additive manufacturing (AM) of 3D CP structures was developed. However, the introduction of a copolymer for mechanical stability resulted in a commensurate loss in electroactive performance, and this loss needs to be addressed to unlock to potential of 3D CP devices.

This work has identified two main themes for the advancement of 3D CP devices. First, improvement of AM approaches for 3D CP devices is conducted through the development of extrusion-based direct ink writing (DIW) of passive support structures as well as the further development of existing photosensitive CP resin formulations for use in vat polymerization of 3D CP-composite structures. Secondly, the improvement of electroactive performance of 3D CP-composite devices is explored through methods to increase surface area and reduce diffusion path lengths by the deposition of hierarchical CP structures.

Development of a DIW process leveraging a support gel improved resolution and quality of 3D polydimethylsiloxane (PDMS) structures enabling the fabrication of 3D CP bilayer devices. The DIW process has also been paired with the development of a PDMS-carbon nanotube composite to produce 3D tubular strain sensors for applications in fluidic networks. The electrical conductivity of CP photosensitive resin formulations has been improved through the integration of polypyrrole (PPy) func-

tionalized carbon nanotubes. This improvement to the material properties enabled the development of a soft-template polymerization process to deposit hierarchical PPy structures on vat polymerized CP composite films. Films with hierarchical PPy features demonstrated improved electrical conductivity compared to those deposited with conventional 2D PPy films. Development of these fabrication methods and improved material properties further advances the potential of 3D CP devices and bridges the gap between the micro- and nanoscales towards controllable nanoscale CP features.

Keywords: Electroactive polymers, conjugated polymers, polypyrrole, additive manufacturing, direct ink writing, vat polymerization, hierarchical structures, polydimethylsiloxane, carbon nanotubes, sensor, actuator, transducer.

Summary for Lay Audience

Conjugated polymers (CPs) are a class of polymers that exhibit a change in size or shape, in response to electrical input. The unique combination of electrical and mechanical properties facilitates the fabrication of novel devices in a broad range of applications including: sensors, actuators, and lab-on-a-chip systems. The alternating single and double bonds along the polymer chain of CPs enables their electroactive properties but is also responsible for processability associated with CPs that has limited fabrication methods. Recent work in the Organic Mechatronics and Smart Materials Laboratory developed a light-sensitive CP composite enabling additive manufacturing (AM) of 3D CP structures. However, the introduction of a secondary material for mechanical stability resulted in a loss in electroactive performance limiting potential applications.

This work has identified two main themes for the advancement of 3D CP devices. First, improvement of AM approaches for 3D CP devices is conducted through the development of extrusion-based direct ink writing (DIW) of passive support structures as well as the further development of existing light-sensitive CP material compositions for use in vat polymerization of 3D CP-composite structures. Secondly, the improvement of electroactive performance of 3D CP-composite devices is explored through methods to increase surface area and reduce minimum feature size by the deposition of hierarchical CP structures.

Development of a DIW process using a support gel improved resolution and quality of 3D polydimethylsiloxane (PDMS) structures enabling the fabrication of 3D CP bilayer devices. The DIW process has also been paired with the development of a PDMS-carbon nanotube composite to produce 3D tubular strain sensors for applications in fluidic systems. The electrical conductivity of CP photosensitive resin formulations has been improved through the integration of polypyrrole (PPy) func-

tionalized carbon nanotubes. This improvement to the material properties enabled the development of a soft-template polymerization process to deposit hierarchical PPy structures on vat polymerized CP composite films. Films with hierarchical PPy features demonstrated improved electroactive performance compared to those deposited with conventional 2D PPy films. Development of these fabrication methods and improved material properties further advances the potential of 3D CP devices and bridges the gap between the micro- and nanoscales towards controllable nanoscale CP features.

Co-Authorship Statement

This PhD thesis has been carefully prepared by F. Benjamin Holness and reviewed by Dr. A.D. Price according to the regulations for a monograph format thesis stipulated by the Faculty of Graduate and Postdoctoral Studies at Western University and has been co-authored as follows:

Chapter 3: Exploratory work in 3D EAP

All experimental work, and manuscript preparation were conducted by F.B. Holness. Manuscript revision was provided by Matthew Lawrence and A.D. Price.

Chapter 4: DIW of PDMS-PEDOT:PSS Actuators

All experimental work, and manuscript preparation were conducted by F.B. Holness. Manuscript revision was provided by Dr. Nicholas Lanigan. Results presented in this chapter have been featured in the publication:
F. B. Holness, Tamie L. Poepping, and Aaron D. Price (Apr. 2019). In: *Electroactive Polymer Actuators and Devices (EAPAD) XXI* 10966, p. 1096606

Chapter 5: DIW of 3D PDMS-CNT

All experimental work, and manuscript preparation were conducted by F.B. Holness. Manuscript revision was provided by Dr. Nicholas Lanigan and A.D. Price.

Chapter 6: 3D PPy composite transducers

All experimental work, and manuscript preparation were conducted by F.B. Holness. Manuscript revision was provided by Matthew Lawrence and A.D. Price. Results presented in this chapter have been featured in the publication:

F. Benjamin Holness, Gerardo Patino Guillen, and Aaron D. Price (Mar. 2021). "Hierarchical electroactive polypyrrole-carbon nanotube composite microstructures by high resolution vat polymerization and soft template electropolymerization." In: *Electroactive Polymer Actuators and Devices (EAPAD) XXIII* 11587, p. 1158711

Chapter 7: Hierarchical 3D PPy

Experimental work for the fabrication of hierarchical PPy structures on flat substrates was conducted in part by Iryna Liubchak, Matthew Lawrence, and F.B. Holness. Experimental work for the soft-template polymerization process for 3D PPy-BEMA-PEGMA substrates was conducted by F.B. Holness. Manuscript preparation was prepared by F.B. Holness. Manuscript revision was provided by Iryna Liubchak and A.D. Price. Portions of the results presented in this chapter have been featured in the publication:

Iryna Liubchak et al. (2020). "Soft template electropolymerization of polypyrrole for improved ph-induced drug delivery." In: *International Journal of Molecular Sciences* 21.21

The way you learn anything is that something fails, and you figure out how not to have it fail again.

J.A. Kobak
NASA Lewis Research Center
Cleveland, 2009

Dedication

Dedicated to my parents. Without you, none of this is possible.

Acknowledgements

Thanks to the members of my Advisory Committee, Prof. Robert Klassen and Prof. Eric Johlin for their insightful guidance throughout the duration of the project.

Special thanks to my thesis supervisor Prof. Aaron Price for his continual support and guidance, and his generosity with his time and advice. Your dedication to your research, students, and family is inspiring.

Thank you to my colleagues in the Organic Mechatronics and Smart Materials Laboratory, past and present, the opportunity to collaborate with you all has made me a better student, teacher, and friend. I would like to extend a special thank you to my labmates, Iyrna Liubchak and Matthew Lawrence, your friendship throughout our studies has been invaluable. Thank you to Dr. Nicholas Lanigan for all of your insight, and guidance.

A thank you must be given to my dog, Murphy, man's best friend and often greatest annoyance, you helped me get through the most challenging of days. Finally, thanks to my dearest friends and family. I owe my deepest gratitude to my parents who are always there for support and guidance, unconditionally, without your help I would not be where I am today.

I am forever grateful for your friendship, guidance, and support. Thank you all.

Equity, Diversity & Inclusion (EDI)

As a commitment to research be accessible to everyone, I have chosen to include a section on Equity, Diversity, and Inclusion (EDI) and my commitments to EDI in research. EDI in research should work to remove barriers to success for equity-deserving groups, which include but are not limited to women, Indigenous peoples (First Nations, Inuit, and Métis), members of racialized groups, persons with disabilities, and members of the LGBTQ2S+ community. This responsibility falls upon students, trainees, postdoctoral fellows, collaborators, and principal investigators to instigate and sustain change. I, as a student, have worked to increase the EDI of my faculty, and Western as a whole for future student success.

Contents

List of Tables

List of Figures

List of Acronyms and Symbols

Acronyms

2D	two-dimensional
3D	three-dimensional
AM	additive manufacturing
ASEM	atmospheric scanning electron microscopy
BCA	bifurcated carotid artery
BEMA	bisphenol A ethoxylate dimethacrylate
COOH	carboxyl
CNT	carbon nanotube
CNC	computer numerical control
CE	counter electrode
CP	conjugated polymer
CSA	camphorsulfonic acid
CV	cyclic voltammetry
DBS	dodecylbenzene sulfonate
DMF	dimethylflormamide
DMSO	dimethyl sulfoxide
DIW	direct ink writing
DLP	digital light processing
DLS	dynamic light scattering
EAP	electroactive polymer
EBL	electron beam lithography
EG	ethylene glycol
FFF	fused filament fabrication
GF	gauge factor
IPA	isopropyl alcohol
LiTFSI	lithium bis(trifluoromethanesulfonyl)imide
MEP	methyl terminated polydimethylsiloxane
MEMS	microelectromechanical
MS	microstructure
MWCNT	multi-walled carbon nanotube
OS	onium salt
PA	polyacetylene

PANI	polyaniline
PIV	particle image velocimetry
PDMS	polydimethylsiloxane
PEDOT	poly(3,4-ethylenedioxythiophene)
PEGMA	poly(ethylene glycol) methyl ether methacrylate
PHEDOT	3,4-phenylenedioxythiophene
PPy	polypyrrole
PSS	polystyrene sulfonate
Py	pyrrole
RE	reference electrode
SEM	scanning electron microscopy
SMU	source measure unit
THF	tetrahydrofuran
TGA	thermogravimetric analysis
TPO	2,4,6-trimethylbenzoyl-diphenyl-phosphineoxide
UV	ultraviolet
WE	working electrode

Greek symbols

σ	electrical conductivity
ϵ	strain
ϕ	volume fraction

Latin symbols

ΔR	change in resistance
I	electric current
R	resistance
V	applied voltage
E	Young's modulus

Subscript symbols

f	filler
0	initial measured value
s	surface

Chapter 1

Introduction

Electroactive polymers (EAPs) exhibit a change in properties, typically size or shape, in response to electrical stimuli (Bar-Cohen, 2005). These materials combine the electrical properties of semiconductors with the mechanical properties of polymers, and this unique combination facilitates the fabrication of novel devices in a broad range of applications including: sensors, actuators, energy harvesters, and lab-on-a-chip systems (Long et al., 2011). The main focus of this work is a class of EAPs called conjugated polymers (CPs), these materials are characterized by their alternating single and double bonds along the polymer chain. This unique bonding structure enables the polymer to be electroactive through alteration of oxidation state. One scheme for CP actuation is described by a neutral polymer chain in the reduced state which swells as the polymer is oxidized, this results in bond reorientation which causes positive charges to form at sites along the chain (Wallace et al., 2009). This unbalanced charge causes anions from the electrolyte to diffuse into the polymer and neutralize the charge once again, this results in both an increased conductivity due to increased mobility of electrons along the polymer chain as well as a volume change which can be exploited for actuation. The conjugated structure that allows CPs to exhibit these semiconductor capabilities can also be attributed with issues of solution or melt processability of CPs which has, until recently, limited CP device fabrication techniques to the formation of powders and films. Recent work in the

Organic Mechatronics and Smart Materials Laboratory has led to the fabrication of 3D CP structures through the development of a photosensitive composite polymer system consisting of electroactive CP and passive support polymers (Cullen and Price, 2019). This composite CP formulation is then used with custom additive manufacturing (AM) techniques to realize 3D component geometries. However, to achieve these 3D structures a passive copolymer was added to improve mechanical stability but has a commensurate loss in electroactivity.

This work aims to further address the processabilty issues of CPs by developing AM approaches to fabricate flexible, conductive 3D structures which may be used as substrates in the post hoc deposition of CP polymers. Furthermore, a critical limitation when developing devices composed of EAPs is the exploitation of ion diffusion as the primary transduction mechanism, reducing the feature sizes to the nanoscale is anticipated to greatly improve transducer response times due to reduced diffusion distances. However, the production of accurate structures on the nanoscale remains elusive (Lewis, 2006). The proposed research aims to bridge the gap between current micro- and nano-scale fabrication technologies by developing AM techniques specifically designed for hierarchical EAPs formulated for the post hoc deposition of controllable nanoscale features.

While great advances have been made in the fabrication of 3D CP structures further investigation is required in both material, and process development to improve the performance of these transducers.

1.1   Objectives

This research project aims to advance the fabrication methods currently developed for EAP transducers and investigate techniques for improving performance of these devices. This goal is encompassed by the following research objectives:

- *Development of additive manufacturing processes for 3D EAP transducers.*
  The first objective is to further develop techniques additive manufacturing
  techniques to create 3D passive support structures for EAP transducers.

- *Combine additive manufacturing techniques with composite material prepa-
  ration to create 3D transducers.* The second objective is to combine additive
  manufacturing processes with novel electroactive composite materials to pro-
  vide new capabilities to sensing systems.

- *Investigate methods to improve the fabrication and material properties of 3D
  polypyrrole composite transducers.* The third objective is to investigate meth-
  ods which can overcome reduced performance of polypyrrole transducers
  associated with the composite materials.

- *Demonstrate post hoc techniques to improve the performance of polypyrrole
  composite transducers.* The final objective aims to demonstrate the post hoc
  deposition of polypyrrole on transducers fabricated by additive manufacturing
  methods will result in improved electrochemical response.

1.2   Major contributions

This thesis conveys the following major contributions to the scientific body of knowl-
edge:

- *Improved resolution and quality of PDMS DIW structures.* Improvements made
  to the AM system and process settings enabled the fabrication of vascular-like
  structures that have applications in fluidics and as passive layers in 3D EAP
  actuators.

- *Development of 3D tubular piezoresistive PDMS-CNT sensors.* The first study demonstrating flexible, 3D PDMS-CNT strain sensor fabricated by DIW.

- *Improvement of PPy-BEMA-PEGMA composite electrical properties.* Developed a refined resin preparation process and incorporated functionalized carbon nanotubes were employed to regain electrical conductivity lost due to the passive copolymers required for mechanical stability.

- *Developed process for the post hoc electrochemical deposition of polypyrrole onto 3D printed PPy-BEMA-PEGMA structures.* Flat films were deposited onto the surface of 3D printed PPy-BEMA-PEGMA films to improve the electrochemical performance of the device. Further improvements were made by applying the technique soft-template electropolymerization to create microspherical structures on the printed CP surface.

1.3   Organization of the thesis

The following chapter, chapter 2 provides the relevant background and current state of the art in the use of carbon nanotubes in 3D EAP devices, a review of AM approaches for the fabrication 3D EAP strucutes with a focus on direct ink writing and digital light processing, a review of CPs is provided to further explore the transduction mechanism and limitations of these materials, finally, a review of approaches for the fabrication of hierarchical CP structures is explored. In accordance with the aforementioned objectives, the remainder of the thesis is organized as follows: chapter 3, *Exploratory work in 3D EAP* summarizes the most influential experimental results of the initial exploratory phase to assess potential for applicable techniques in material and process development to improve performance of 3D EAP transducers. Chapter 4, *DIW of PDMS-PEDOT:PSS Actuators* explores the development of

direct ink writing of 3D PDMS structures and the post hoc deposition of PEDOT:PSS to fabricate bilayer actuators. Next, chapter 5, *DIW of 3D PDMS-CNT* extends upon the direct ink writing process through the development of a PDMS-CNT composite to directly fabricate functional 3D devices. The applications of planar cast sensors and 3D tubular piezoresistive sensors are explored. Chapter 6, *3D PPy composite transducers* explores potential routes to improve the electrical and ionic conductivity of PPy-BEMA-PEGMA composite devices through the fabrication and incorporation of PPy functionalized CNTs. Chapter 7 discusses the soft-template polymerization approach developed to produced both planar hierarchical polypyrrole films as well as the first case of hierarchical polypyrrole structures. Finally, chapter 8, *Concluding remarks* summarizes the primary conclusions of the work, reiterates the main contributions to knowledge, and provides recommendations for future research. Figure 1.1 summarizes the research path taken to accomplish these objectives through the main streams of improving AM techniques and the post hoc deposition of hierarchical structures.
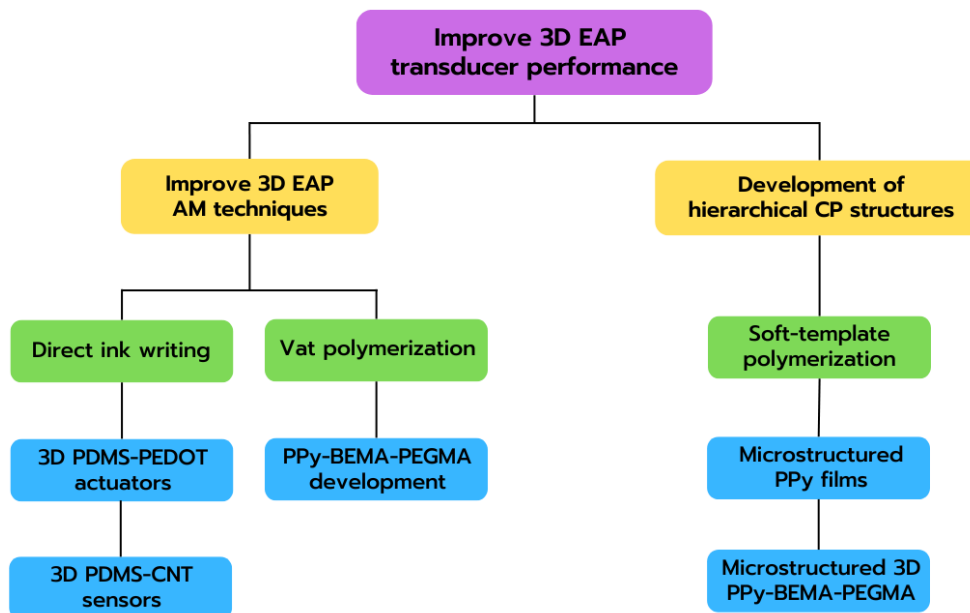
Figure 1.1:   The research streams undertaken in the work to improve 3D electroactive polymer device performance focused on improving additive manufacturing approaches and the post hoc deposition of hierarchical structures.

1.4   References

Bar-Cohen, Yoseph (2005). "Current and future developments in artificial muscles using electroactive polymers." In: *Expert Review of Medical Devices* 2.6, pp. 731–740.

Cullen, Andrew T and Aaron D Price (2019). In: *Smart Materials and Structures* 28.10, p. 104007.

Lewis, J. A. (Nov. 2006). "Direct Ink Writing of 3D Functional Materials." In: *Advanced Functional Materials* 16.17, pp. 2193–2204.

Long, Yun-Ze, Meng-Meng Li, Changzhi Gu, Meixiang Wan, Jean-Luc Duvail, Zongwen Liu, and Zhiyong Fan (Oct. 2011). "Recent advances in synthesis, physical properties and applications of conducting polymer nanotubes and nanofibers." In: *Progress in Polymer Science* 36.10, pp. 1415–1442.

Wallace, Gordon G, Peter R Teasdale, Geoffrey M Spinks, and Leon A P Kane-Maguire (2009). *Conductive Electroactive Polymers: Intelligent Polymer Systems*. 3rd. CRC Press.

Chapter 2

Background and state of the art

This chapter will summarize the relevant background information for topics discussed in this work. First a review of carbon nanotubes is provided and their application as a conductive filler towards 3D EAP devices is explored. This is followed by a review of conjugated polymers, specifically polypyrrole and poly(3,4-ethylenedioxythiophene), as these are the materials of main interest to this work. A review of additive manufacturing techniques such as direct ink writing and vat polymerization is provided with a specific focus on existing approaches to fabricate 3D EAP structures. Finally, the various techniques for fabricating CP hierarchical features is discussed.

2.1 Carbon nanotubes

2.1.1 Structure and properties

Carbon nanotubes (CNTs) are highly structured, carbon-based materials that exhibit interesting mechanical, electrical, and thermal properties(Baughman, Zakhidov, and Heer, 2002). These properties have led to widespread use of CNTs in various applications including structural composites, energy storage, thermal conductors, medical devices, sensors, and many more (Chu et al., 2013; Ma et al., 2010; Snook,

7

Kao, and Best, 2011). While research interest into carbon nanotubes has been widespread, there are challenges in realization of applications due to poor dispersion of entangled CNTs. These challenges arise due to the high aspect ratio of the CNT geometry resulting in incredibly high surface areas which in combination with high electrostatic interaction and van der Waals force requiring attention to overcome. These agglomerates have been shown to negatively impact the electrical and mechanical properties of the CNTs and reduce their effectiveness as a filler (Thostenson, Ren, and Chou, 2001). Challenges in dispersion of CNTs are typically addressed through means of dispersion technique as well as chemical modification or functionalization. While early dispersion of CNTs in a polymer matrix were achieved through manual mixing with a mortar and pestle, more efficient and effective techniques have been developed (Fukushima et al., 2006).

Mechanical techniques for creating dispersions of CNTs include: ultrasonication, three roll milling, ball milling, and high shear mixing. Ultrasonication is the most common of these methods where ultrasonic waves are created by a transducer and passed through a dispersing fluid. These waves cause acoustic cavitation and high pressure regions in the fluid creating high shear forces which enable the disentanglement of CNT bundles. Ultrasonication is usually performed by a bath sonicator where high frequency (40 kHz), lower power waves are produced in a bath in which glassware containing the solution to disperse can be suspended. Alternatively, a probe sonicator can be used where a metal probe is placed directly into the dispersing fluid and sonication waves of 20 kHz are produced at the tip of the probe (Gupta et al., 2013). These highly directional, high powered waves can provide more effective dispersion but also risks damaging the CNTs, thus, careful consideration must be given to the amplitude and length of time of the sonication. However, both techniques can be appropriate in creating well-dispersed and stable CNT solutions depending on the CNT concentration and solvent.

Another common mechanical method for the creation of CNT dispersions is the three roll mill. Where ultrasonication may be used with lower viscosity solvents, the three roll mill provides a dispersion technique for more viscous materials. The three roll mill consists of three adjacent rollers where the direction of rotation alternates between rollers. This opposing rotation draws material in-between the first two rollers and back up to the final roller where the material is scraped off the roller for final use or is recycled to the beginning for further processing. The gaps between adjacent rollers can be adjusted from 1 µm to 500 µm, this narrow gap creates high shear stress regions which can adequately disentangle CNT bundles. These gaps have spacing of similar dimension to typical CNT length but are much larger than the typical CNT diameter, leaving potential for reducing the size of CNT bundles but not complete disentanglement of individual CNTs (Gojny et al., 2004). However, the advantages of the three roll mill procedure is the potential for solvent-free dispersion and the ability to easily control the energy applied to the CNTs limiting mechanical deformation and defect production during dispersion.

Finally, ball milling and high shear mixing have also been used to create dispersions of CNTs in polymer matrices. Ball milling is a grinding method where the rotation of vessel filled with small rigid balls creates high pressure collisions that decrease the size of the filler particles. In the case of ball milling of CNTs there can be significant damage resulting in the shortening of CNTs and even the transformation of the CNTs to carbon nanoparticles (Li et al., 1999). High shear mixers may also be employed for creating dispersion of CNTs directly in thermosetting polymers however they lack the stability of other techniques as re-agglomerations have been observed.

While dispersion method has a great impact on the quality of the composite that can be produced, another key factor in the dispersion quality is the functionalization of CNTs. Through functionalization of CNTs greater attraction can be made between

the CNTs and the polymer matrix improving the interfacial interaction. Chemical functionalization of the CNT sidewalls results in the modification of covalent bonding from sp^2 to sp^3 by treating the CNTs with a highly reactive substance like fluorine. Fluorination of CNTs results in the weak covalent C-F bonds that can then be substituted with the desired functionalization such as amino and hydroxyl groups (Mickelson et al., 1998). Another common functionalization approach is through defect functionalization. In this approach defects are formed on the sidewalls or open ends of CNTs by oxidation in strong acids like HNO_3 and H_2SO_4 or strong oxidants like $KMnO_4$. These defects are then stabilized with the addition of functional groups such as hydroxyl groups or carboxyl (COOH) groups by treatment with COOH acid (Saito, Matsushige, and Tanaka, 2002). These functionalizations can be critical in improving mechanical and electrical properties of composite materials by firstly improving the dispersion quality by adjusting the CNT polarity to suit the solvent employed as well as improving the interfacial interaction between the CNTs and the composite matrix polymer.

These techniques have been widely applied in the development of CNT composite materials using thermoplastics, thermosetting polymers, epoxies, and elastomers. In each case the percolation of the conductive network can be identified as a critical factor in the performance of the composite material. In the case of CNTs the quality of dispersion affects the percolation threshold and the electrical properties of the composite can be related to percolation theory where a transition from insulator to conductor occurs as the CNT loading percentage and dispersion quality is such that a continuous electron path can be formed (fig. 2.1). This path results in a significant increase in the electrical conductivity of the composite and is denoted as the percolation threshold.
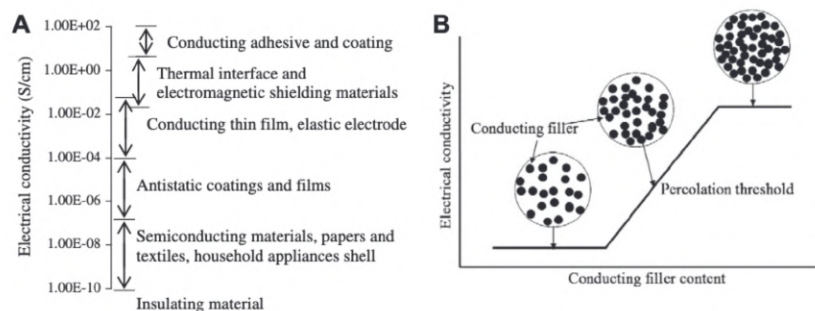
Figure 2.1:   (a) Typical applications and their associated electrical conductivity ranges cover a wide range where these conductivities depend upon the carbon nanotube percolation theory depicted in (b). © Ma et al. (2010), included with permission.

2.1.2   Carbon nanotube elastomer composites

These principles have been applied in the development of CNT-based elastomeric composites which they have been implemented as wearable sensors due to their flexibility, biocompatibility, and sensitivity (Rajendran et al., 2021). A common elastomer explored in CNT composites is polydimethylsiloxane (PDMS), where the general procedure involves the dispersion of CNTs in a solvent, the addition of PDMS elastomer, removal of solvent and addition of curing agent. One of the challenges associated with this process is the selection of a solvent that is effective in both the creation of a stable CNT dispersion free of agglomerations as well as a good solvent the for the PDMS elastomer. In a study conducted by Liu and Choi (2012) solvents toluene, chloroform, tetrahydrofuran (THF), and dimethylflormamide (DHF) were analyzed as suitable candidates for the fabrication of a CNT composite with the commercial PDMS formulation Sylgard 184. This work highlighted the importance of solvent selection where THF and chloroform were identified as strong candidates due to their ability to disperse CNTs and PDMS separately but when the two solutions were combined, the THF solutions were not stable and visible separation was observed after 30 min, whereas the chloroform solutions maintained a stable

dispersion of PDMS and CNTs even after 42 h. Additionally, it was found that COOH functionalized CNTs exhibited more stable performance than pristine CNTs when dispersed in chloroform. However, Ramalingame et al. (2018) conducted a study on the solvent effect on the capacitive-pressure response of a CNT-PDMS composite device which demonstrated that higher sensitivities could be achieved using toluene or isopropyl alcohol (IPA) as a solvent despite less stable performance of the created dispersions. In this work it was shown that devices prepared using chloroform as a solvent exhibited the lower sensitivity but less noisy response. From these works and it can be seen that the solvent selection is a major contributing factor to the device performance but other factors in the fabrication process can greatly impact the outcome. An alternative approach to employing functionalized CNTs has been reported by J. H. Kim et al. (2018) where highly elastic and conductive CNT-PDMS composite material was fabricated by addition of methyl terminated PDMS (MEP). In this process, pristine MWCNTs were first dispersed in IPA by ultrasonication at which point MEP was added with further sonication. The MEP then penetrates the IPA dispersion and adheres to the hydrophobic surface of the CNTs, this creates preferred attachment points for Sylgard 184 elastomer which results in a high quality, stable dispersion of CNT-MEP-PDMS (fig. 2.2).

In these examples the PDMS-CNT composites are typically forced into moulds to create 2D films which can then be analyzed as piezoresistive or capacitive sensors for biomedical and wearable applications. However, there has also been work into the development of architected films through the introduction of sacrificial sugar templates. Michel et al. (2020) developed an open-celled foam sacrificial sugar template for the fabrication of piezoresistive sensors to reduce the stiffness of the devices. The stiffness of the device is modified by adjusting the weight fraction of sugar template in the PDMS-CNT dispersion (fig. 2.3). This work demonstrated that piezoresistive sensors with more porous structures exhibited reduced sensitivity
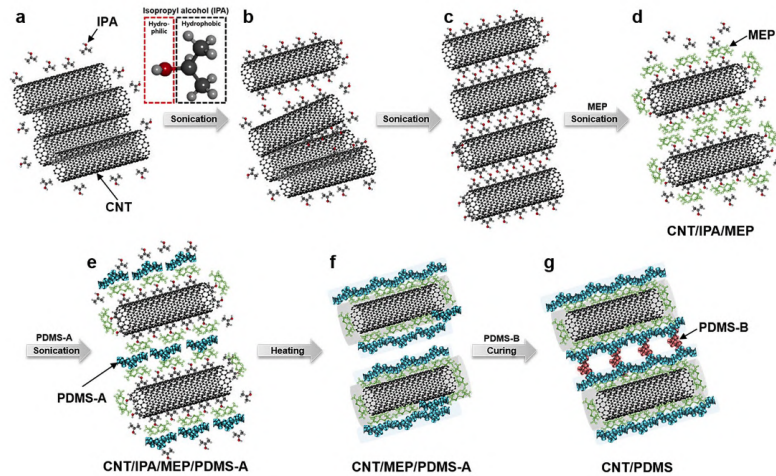
Figure 2.2: Schematics of PDMS-MEP-CNT hybrid nanocomposite fabrication. (a–c) Detachment and dispersion of aggregated CNT bundles in IPA by hydrophobic regions of IPA and ultrasonication, (d) wrapping of IPA attached CNTs by MEP, (e) attachment of PDMS-A to MEP, (f) evaporation of IPA by heating, followed by entanglement of CNT/PDMS complexes, and (g) fabrication of PDMS-MEP-CNT composite materials after mixing with curing agent for cross-linking of PDMS. © J. H. Kim et al. (2018) CC BY-NC 4.0.
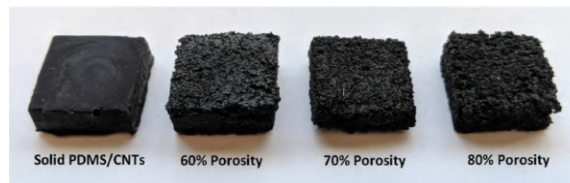
Figure 2.3: PDMS-CNT foam porosity is controlled by varying the weight ratio of the sacrificial sugar template. © Michel et al. (2020) included with permission.

likely due to collapsing of pores contributing to strain more than deformation of the PDMS-CNT network. Jeon et al. (2019) further examined these porous sensors as piezocapacitive sensors to incorporate the capacitance change observed as a function of strain and incorporated this factor in the impedance gauge factor further improving the sensitivity of these sensors.

While there has been extensive work completed towards the development of the PDMS-CNT composite materials and casting of 2D-films, there has been limited but growing investigation in the additive manufacturing of these materials to fabricate 3D devices. A common application in additive manufacturing of PDMS-CNT compos-

ites is to employ direct ink writing to fabricate simple and complex 2D patterns of the material onto a passive substrate. Abshirini et al. (2019) applied this technique to create encapsulated PDMS-CNT strain sensors by directly extruding the composite material onto a PDMS film which was then fully encapsulated by pouring uncured PDMS over the top of the printed pattern. This technique enables the fabrication of complex 2D patterns that can be modified to improved the sensitivity of the device as well as fully encapsulating the active materials while maintaining the flexibility of PDMS. In the work conducted by Emon et al. (2019) a multi-material extrusion system was developed to enable the direct fabrication of piezoresitive sensors by first depositing a flexible photocurable base layer followed by an ionic liquid based pressure sensitive layer before finally depositing PDMS-CNT as a flexible electrode. While this example does not employ PDMS-CNT as the sensing material, it demonstrates the potential for multi-material sensing systems exploiting the flexibility and conductivity of the composite material for transducer fabrication. While this system is capable of fabrication of complex 3D multi-material structures, the fabricated transducers introduced are limited to multi-layered 2D, however, this will likely be the aim of future development of the fabrication process. The final DIW example to be discussed is by Fekiri, H. C. Kim, and Lee (2020) where a PDMS-CNT composite is developed by a process similar to J. H. Kim et al. (2018) with the introduction of MEP to aide in the dispersion of CNTs in PDMS. In this work a DIW system is employed to fabricate 3D structures ranging from 3D rings and tetrahedral pyramids (fig. 2.4). These structures demonstrate that PDMS-CNT 3D transducers are achievable by extrusion-based additive manufacturing approaches. However, given that these structures are self-supported, the complexity of achievable structures may be limited by the maximum overhanging feature that can be produced. Finally, characterization of the devices fabricated in this work is limited to 2D structures deposited on flexible substrates.
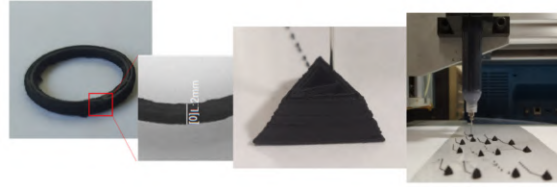
Figure 2.4: Direct ink writing was employed to fabricate 3D PDMS-CNT nanocomposite structures represented by 10 layer rings and tetrahedral pyramids. © Fekiri, H. C. Kim, and Lee (2020) CC BY-NC 4.0.

Another additive manufacturing technique employed in the fabrication of 3D PDMS-CNT transducers is digital light processing (DLP), which will be discussed in further detail below. Xiao et al. (2007) developed a photosensitive elastomer composite comprised of epoxy aliphatic acrylate, aliphatic urethane diacrylate, and 2 % MWCNTs. The development of this flexible photosensitive resin enabled the use of a multi-material DLP-based fabribracation system and the production of high-resolution 3D structures. The multi-material capabilites of the system were leveraged to directly fabricate a 4 × 4 strain sensor array with active CNT-Composite sensing material deposited onto a passive flexible base layer. These examples demonstrate the growing exploration of the application of well-studied CNT-containing composite materials to additive manufacturing techniques, however, there exists a knowledge gap in the application of 3D sensors to further broaden the reach of these devices.

2.1.3 Conjugated Polymers

This work will focus on a class of EAPs called conjugated polymers (CPs), these materials are characterized by their alternating single and double bonds along the polymer chain as shown in fig. 2.5. This structure enables the polymer to be electroactive through alteration of oxidation state. The redox reaction shown in fig. 2.6, demonstrates one scheme for CP actuation where the polymer chain is neutral
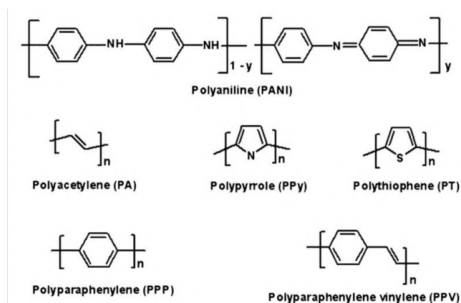
Figure 2.5: The chemical structure diagrams of a group conjugated polymers demonstrates the alternating single and double bonds of the polymer chain. © Bhadra et al. (2009) included with permission.

in the reduced state. As the polymer is oxidized, bond reorientation causes positive charges to form at sites along the chain. This unbalanced charge causes anions from the electrolyte to diffuse into the polymer and neutralize the charge once again, this results in both an increased conductivity due to the increased mobility of electrons along the polymer chain, a volume change which can be exploited for actuation. Early research into CPs conducted by Shirakawa et al. (1977) led to the discovery of the polyacetylene (PA) as shown in fig. 2.5, which was soon followed by the expansion of this group to include a number of other CPs with several common materials being: polythiophene, polyaniline, polypyrrole, and poly(3,4-ethylenedioxythiophene) (PEDOT). Discovery of this new class of materials which exhibited semi-conductor electrical properties combined with the mechanical properties of polymers led to applications of CPs including: energy storage, anti-static coatings, actuators, and sensors (Crowley et al., 2008). However, the conjugated structure of the polymer chain which provides the electrical properties contributes to limited solubility and inability to be melt-processed. These factors have contributed to fabrication methods which focus on 2D deposition methods, however, there have been more recent advances to enable fabrication of 3D CP structures.
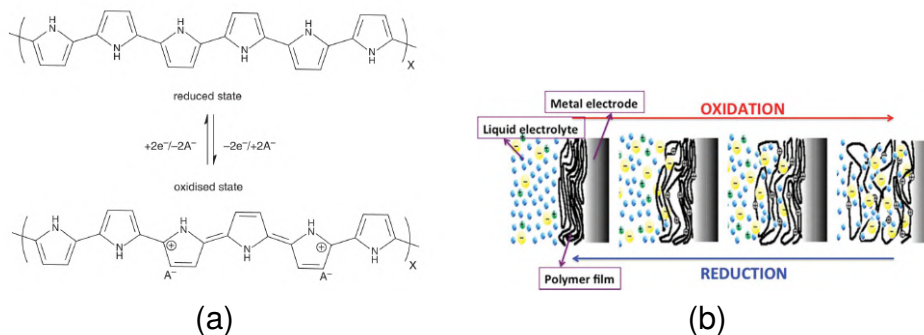
Figure 2.6: (a) Depicts the oxidized and reduced states of the conjugated polymer polyprrole and (b) shows a scheme for the volumetric change associated with the diffusion of ions into or out of the polymer chain to reach charge and osmotic balance. © Otero (2017) CC BY-NC 4.0.

Polypyrrole

PPy is one of the commonly studied CPs based on a suitable combination of reasonably high conductivity combined with suitable stability and processability. The redox reaction associated with PPy is shown in fig. 2.6 (a), where in the reduced state PPy is neutral polymer, however, when oxidized, bond reorientation occurs resulting in the formation of positive charge along the polymer. This change initiates the travel of anions from a surrounding electrolyte to diffuse into the polymer network and neutralize the charge, while the large size of these ions causes a volumetric change in the material. To this end, the choice of anion in the electrolyte should be carefully considered to maximize this volume change with common choices for PPy being lithium bis(trifluoromethanesulfonyl)imide (LiTFSI) and dodecylbenzene sulfonate (DBS) due to high molecular weight functional groups. In the work conducted by Spinks et al. (2009) there has been reported volume changes in PPy of 35 % when doped with LiTFSI. This volume change can be exploited in the fabrication of actuators by deposition of PPy on a passive structure to create a bilayer actuator which can be electrochemically controlled. The operation of a PPy bilayer actuator is shown in fig. 2.7 where a change in the applied potential in an electrochemical cell

17
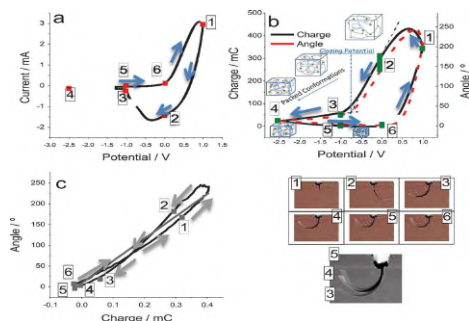
Figure 2.7: Controllable electrochemical response of polypyrrole-tape bilayer actuator is shown where the relation between applied potential and current is connected to the associated volumetric change and bending angle of the actuator. © Otero (2017) CC BY-NC 4.0.

will result in the ingress or egress of ions into and out of the PPy film. The volume change of the PPy film in combination with the lack of volume change in the passive layer creates a stress gradient that results in bending of the film and controllable tip deflection. As also shown in fig. 2.7 these actuators can operate at low voltages, typically ±1 V. An advancement of the bilayer design where bending is limited to the side with the PPy film is a trilayer design with PPy films deposited on either side of a porous, passive film, which are then connected as opposing electrodes such that an applied potential difference results in diffusion of ions from one film to the other along with the commensurate expansion and contraction. This results in actuation towards the side with the contracting film until the potential is switched. The trilayer design enables improved range of motion and the potential for encapsulation of the actuator. These examples highlight the importance of the ion diffusion within the polymer for actuator performance both to ensure all doping sites are accessible and increase actuation frequency. This research aims to improve CP transducer performance by reducing the diffusion distances required.

As discussed above the processability issues associated with CPs excludes many conventional polymer processing techniques, however, complex devices have been fabricated by direct polymerization of PPy. The basic polymerization mechanism for PPy consists of the oxidation of the monomer pyrrole (Py) to generate reac-

tive Py radicals. These radicals then react to form dimers and oligomers continually to allow for chain propagation of PPy, this oxidation source is typically either supplied by electrochemical methods or chemical methods. In electrochemical polymerization of PPy the monomer is oxidized at the anode surface resulting in the formation of a PPy film at the electrode surface. Alternatively, in chemical oxidative polymerization a chemical oxidant is placed in solution with the Py monomer. This technique typically produces PPy particles but can be controlled by the addition of surfactant molecules or solvent selection to create oxidant-monomer interfaces to direct the polymerization reaction. While chemical oxidative polymerization techniques are able to produce nano-scale particles and electrochemical polymerization methods allow for selective polymerization of PPy to fabricate complex micro-scale devices, these processes are difficult to apply towards the fabrication of complex 3D devices (Jager, Smela, and Inganäs, 2000). However, recent developments in photosensitive PPy formulations have unlocked the potential for the fabrication of 3D PPy composite structures. In photopolymerization of PPy typically a weak oxidant is included which without external input either cannot polymerize or very slowly polymerizes PPy, but with exposure to light the oxidation strength increases to photochemically initiate the oxidative polymerization of PPy. Weak oxidants previously used in photosensitive polymerization of PPy include the copper complex $[Cu(dpp)]^{2+}$ (dpp = 2,9-Diphenyl-1,10-phenanthroline), the ruthenium complex $[Ru(bpy)_3]^{2+}$ (bpy = 2,2'-Bipyridine), and commercial photoinitiators which produce Fe^{3+} ions to initiate the polymerization reaction (Kern and Sauvage, 1989; Rabek et al., 1992; K. Yamada, Y. Yamada, and Sone, 2014). Another common method is the use of a silver salt to create sliver ions to initiate the photopolymerization process. These ions are typically weak oxidants but can have their oxidation potential greatly increased through exposure to ultraviolet (UV) light (Mohandass et al., 2012). Additionally, the use of these systems with longer wavelength light source can be achieved through the

addition of an ancillary photoinitiator as shown by Oliver J Murphy et al. (2001). While relatively high electrical conductivities can be achieved, especially for silver ion containing formulations due to the formation of silver ions, there still remains issues with the brittle nature of the photopolymerized PPy. Thus, attempts to improve the mechanical properties have been made throughout the development of photosensitive PPy composite formulations where a secondary polymer is simultaneously polymerized to provide mechanical stability (Asmussen, Arenas, and Vallo, 2015). Recent work conducted in the Organic Mechatronics and Smart Materials Laboratory by Andrew T Cullen and Aaron D Price (2019) developed a hybrid PPy formulation using Bisphenol A ethoxylate dimethacrylate (BEMA) and poly(ethylene glycol) methyl ether methacrylate (PEGMA) as secondary polymers to provide mechanical stability. Additionally, BEMA is a commonly used solid electrolyte in conjunction with PEGMA as a diluent to obtain the desired viscosity (Ijeri et al., 2010). This photosensitive PPy resin formulation also includes the photoinitiator 2,4,6-Trimethylbenzoyl-diphenyl-phosphineoxide (TPO), Tinuvin 477 as a UV absorber, as well as Py and silver nitrate in a 8:1 molar ratio where silver nitrate acts as the weak oxidant which is further sensitized by UV exposure. This formulation demonstrated similar electrical conductivity to earlier photopolymerized PPy while incorporating 40 % BEMA-PEGMA for improved mechanical stability. This formulation was then used for the fabrication of 3D structures by a custom additive manufacturing system discussed in detail below.

PEDOT:PSS

Another widely studied CP is PEDOT, specifically when doped with the polyanion poly(styrenesulfonate) (PSS) to form PEDOT:PSS. This material is of interest for its high conductivity, thermal stability, and transparency while also being readily commercially available as an aqueous colloidal dispersion. These qualities have

led to applications of PEDOT:PSS in flexible displays, solar cells, and soft actuators (Kirchmeyer and Reuter, 2005; Pei et al., 1994). Greco et al. (2011) employed PEDOT:PSS in the fabrication of free-standing PEDOT:PSS nanofilms through a layer-by-layer spin coating fabrication process. Free-standing films as thin as 40 nm could be fabricated by first depositing PDMS as a release layer followed by PE-DOT:PSS and finally a supportive layer of water soluble Poly(vinyl alcohol) (PVA). This work provided the first characterization of the mechanical properties of PE-DOT:PSS nanofilms showing that when in water they can be manipulated without cracking as well as can be transferred to a variety of substrates including: PDMS, paper, and human skin. This work led to futher development of PEDOT:PSS based actuators by Taccola et al. (2013) where bilayer PEDOT:PSS-SU8 were fabricated by a similar spin coating procedure. This deposition process was combined with photolithography whereby the negative photoresist SU8 becomes insoluble to the developer in regions exposed to UV light. This allows for complex thin-film patterns to be produced, structures are shown in fig. 2.8 where cantilever beam actuators can be formed along with electrode surface, enabling electrical contact with the micro-actuators. These actuators were then shown to actuate in an electrochemical cell in an aqueous solution of NaDBS from 0.4 V to −0.8 V demonstrating bending in the oxidated state due to the expulsion of Na^+ ions form the PEDOT:PSS polymer chain.

Finally, further development in PEDOT:PSS actuators by Silvia Taccola et al. (2015) led to the fabrication of PEDOT:PSS-PDMS bilayer actuators that leveraged the hygroscopic properties of PEDOT:PSS to allow for actuation to be initiated either through joule heating or a change in humidity in the surroundings. The fabrication process remains similar to previous works where spin coating is leveraged to pro-duce uniform, thin-film structures however in this work the PDMS layer typically employed as a release layer due to poor adhesion is used as a passive layer. Adhe-
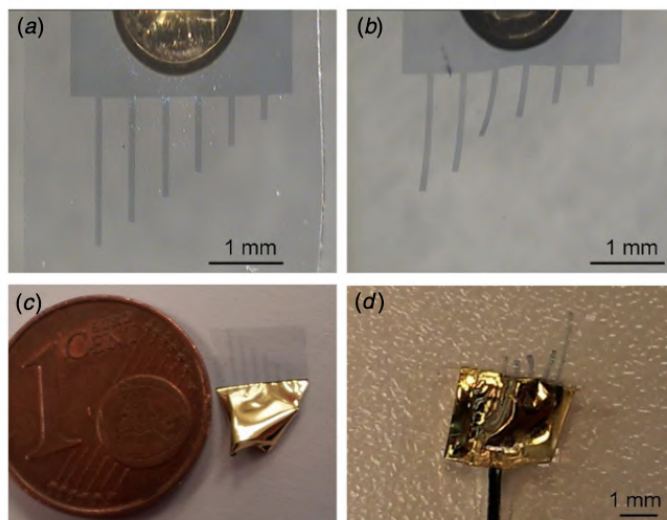
Figure 2.8:   Micro-scale PEDOT:PSS/SU8 bilayer actuators in the dry state supported by a sacrificial Poly(vinyl alcohol)film (a), in water following removal of the support film (b), the actuator device equipped with sputter coated gold electrode (c), and the actuator in water with electrical contact (d). © Taccola et al. (2013) included with permission.

sion of PEDOT:PSS to the PDMS base layer is achieved through plasma treatment of the cured PDMS base layer by increasing the surface energy of the film and allowing improved wetting and adhesion of subsequent PEDOT:PSS layers. Figure 2.9 demonstrates the operating principals for these actuators where by an application of electrical contacts at either end of a resistive PEDOT:PSS path will result in joule heating of the film and the subsequent evaporation of water contained with the PEDOT:PSS, resulting in a contraction of the film and a bending of the bilayer actuator. Upon cooling of the film, water vapour in the environment will be reabsorbed by the PEDOT:PSS returning the actuator to the original position. Interestingly, these actuators were shown to exhibit similar behaviour by controlling the relative humidity of the environment. While these examples of PEDOT:PSS-based actuators demonstrate complex structures and promising performance, they are currently limited to 2D thin film techniques. This work will aim to build off upon the existing knowledge to develop 3D PEDOT:PSS actuation systems.
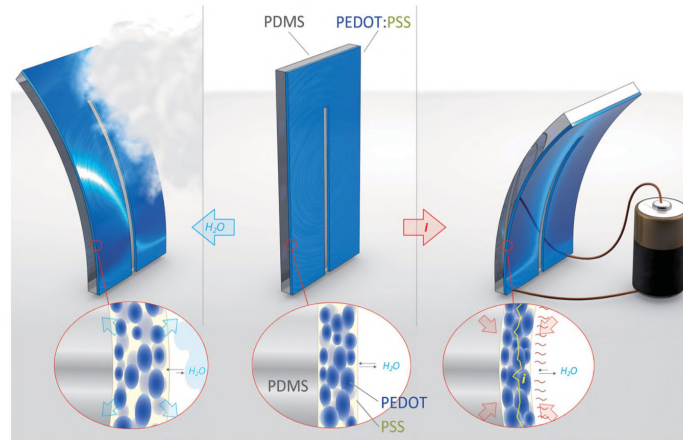
Figure 2.9: Schematic of PEDOT:PSS-PDMS bilayer actuators based on humidity and joule heating where the addition of humidity causes water absorption, and a volume expansion causing actuation or the application of applied potential results in heating of the film, a desorption of water, and decrease in volume causing actuation. © Silvia Taccola et al. (2015) CC BY-NC 4.0.

2.2   Additive Manufacturing

Additive Manufacturing (AM), more commonly known as 3D printing, refers to a process in which a 3D object is fabricated by the successive formation of 2D layers using computer generated 3D model data to control an automated fabrication system (Committee, 2012). This is a fundamental difference from subtractive manufacturing methods where material is a removed from a stock work piece. AM allows for waste reduction in AM processes as well as the ability to fabricate geometries otherwise not possible by conventional manufacturing processes. The four main classifications for AM techniques based on the mechanism for layer deposition are: photopolymerization, power-based, lamination, and extrusion (Ambrosi and Pumera, 2016). This work will explore the potential of photopolymerization-based and extrusion-based techniques for the fabrication of 3D EAP transducers.

2.2.1   Direct ink writing

The main focus of this research is the fabrication of nano-scale features on 3D CP structures. However, the conjugated structure of the polymer chain that enables conductivity also greatly limits the processability of the material. For example, these polymers are not melt-processable or soluble in common solvents. Until recently, this general intractability has limited advances in fabrication technologies to monolithic 2D film deposition techniques (Ung et al., 2013). Recent advances in Organic Mechatronics and Smart Materials Laboratory have helped overcome these obstacles through the development of AM approaches for creating high-resolution 3D CP structures and devices. The first technique employed Direct Ink Writing (DIW) in combination with a chemical processing method of the CP polyaniline (PANI) (Holness and Aaron D Price, 2018). The DIW process involves the layer-by-layer extrusion of an ink or paste using computer numerical controlled (CNC) motion and pneumatic extrusion systems. The DIW system allowed for the fabrication of high-resolution 3D conductive PANI structures with overhanging features as well as the development of a multi-material extrusion system which enable the production of a piezoresistive PANI-based strain sensor. While this initial demonstration was successful, further work is required in material development to improve both the electrical and mechanical properties. The development of the fabrication system enables an alternative approach to achieving 3D CP transducers by the fabrication of compliant, 3D passive substrates which may then be coated with a CP film. The 3D structure of the passive structure may still allow for interesting new actuation modes beyond what is currently achievable. This idea has been adapted from the work done in bio-printing where the ink is printed directly into a gel support bath (Bliley et al., 2022; Hinton et al., 2015). This bath behaves as a Bingham plastic, yielding under an applied shear stress by the nozzle but regaining its stiffness when the stress is removed, allowing extruded material to be supported until it is cured,

and the cured 3D structure can be removed from the support bath.

2.2.2   Light-based additive manufacturing

Digital Light Processing (DLP) is a vat polymerization technique whereby photocurable resins are selectively cured in a layer by layer process through the projection of a high-resolution image on the resin liquid interface. While commercial DLP systems are available, a system has been developed by Andrew T. Cullen and Aaron D. Price (2018) specially designed for multi-material fabrication of CP transducers for use in the Organic Mechatronics and Smart Materials Laboratory. Figure 2.10 demonstrates the DLP fabrication process along with standard calibration structures fabricated at a height of 2.5 mm with both a conventional photopolymer blend and a hybrid PPy formulation. The key advantages of this system are the high-resolution 385 nm light engine with a pixel size of 5 µm and layer resolution of 10 µm which is a substantial improvement over extrusion-based techniques and allows for the fabrication of more complex transducer designs. This system also includes the potential for multi-material fabrication capabilities allowing for direct fabrication of both passive and active structures. This recent development in CP AM opened up a field of new transducer technologies with the ability to fabricate microscale CP structures. However, with the novelty of the technology there is great room for refinement of both the process parameters and resin formulation. Previous photosensitive formulations based on PPy alone have poor mechanical properties and cannot achieve 3D structures (Hodko, Gamboa-Aldeco, and Oliver J. Murphy, 2009), creating the requirement for a copolymer to provide the structural integrity but may also limit channels for ion diffusion.
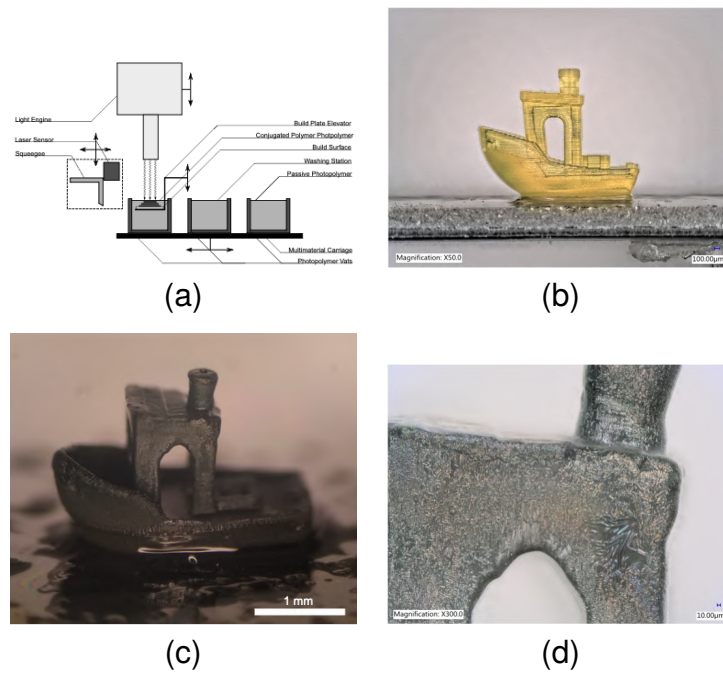
Figure 2.10: The schematic of the digital light processing fabrication system (a) is calibrated with standard benchmarking model fabricated with conventional photopolymer (b), and polypyrrole composite (c,d). © Andrew T Cullen and Aaron D Price (2019) included with permission.

2.3 Hierarchical structure fabrication techniques

2.3.1 Vapour phase deposition

After establishing a base structure from which to build hierarchical structures, post-processing techniques for fabrication of those structures must be considered. An example of this technique has been developed by Santino et al. (2017) where a fibre mesh substrate is saturated in oxidant solution and placed under competing flows of humid nitrogen gas and monomer/chlorobenzene vapour. The interaction between the chlorobenzene vapour and the oxidant results in a nucleation site comprised of a water droplet surrounded by a thin film of oxidant and polymerization occurs at the vapour-liquid interface, fig. 2.11. As the polymerization progresses, the droplet is remains at the tip of the tube allowing for continued growth at the interface. The tube morphology is driven by the polymerization rate which is a function of the mass flow rates of monomer and water vapours. While this process has only reported tubes in the microscale, there is a secondary polymerization which occurs perpendicular to the microtube resulting in a hierarchical scheme. This procedure yields stable hierarchical structures that grow perpendicular to the substrate surface regardless of geometry which is promising for 3D substrates, however, the polymerization reaction is dependent upon the saturation of oxidant in the mesh and its ability to diffuse to the liquid-vapour interface.

2.3.2 Soft-template polymerization

The next deposition techniques to be considered is called soft-template polymerization. As mentioned above, a common route for synthesis of CPs is electropolymerization. In this system an electrochemical cell is formed with the desired monomer and anionic dopant salt contained in a solution with a suitable solvent. At the ap-
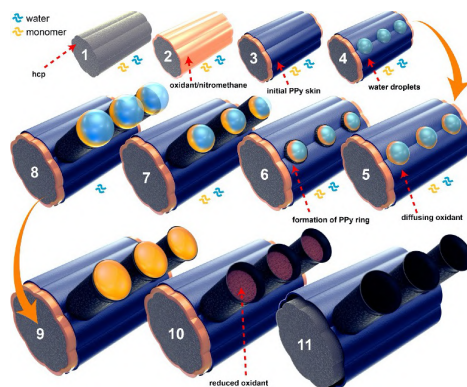
Figure 2.11: Hard carbon fibre paper is used a substrate for the formation of poly-pyrrole microtubes via vapour phase deposition by first saturating the substrate in oxidant to allow polymerization a thin polypyrrole film, increased humidity causes water droplets to form which are then used as template to dictate polymerization of polypyrrole microtubes. © Santino et al. (2017) included with permission.

plied oxidation potential of the monomer, radical cations are formed, which react to form oligomers and the polymer (Sabouraud, Sadki, and Brodie, 2000). This technique is most commonly used to create films on planar substrates with controllable thicknesses, however, work by Qu et al. (2004). demonstrated the ability to create PPy microstructures such as bowls, cups, and bottles through the control of electrochemical polymerization conditions by using a gas bubble template on the working electrode (fig. 2.12). Gas bubble templates of both hydrogen and oxygen gas were used to produce these microstructures on the order of 50 μm in diameter; however, gas bubble size and distribution was found to be dependent upon adaptation of the experimental conditions. Due to the increased surface area these films possess a larger double layer capacitance and improved electrochemical performance. Using this work as a basis, many other groups have pursued electropolymerization of PPy and other CPs around gas bubble templates. One of these studies has demonstrated improved stabilization of the gas bubbles to achieve 3,4-phenylenedioxythiophene (PhEDOT) nanotubes of approximately 300 nm but also demonstrated the high dependence of monomer selection on the resultant structures given that monomers with the same moiety showed differences in the
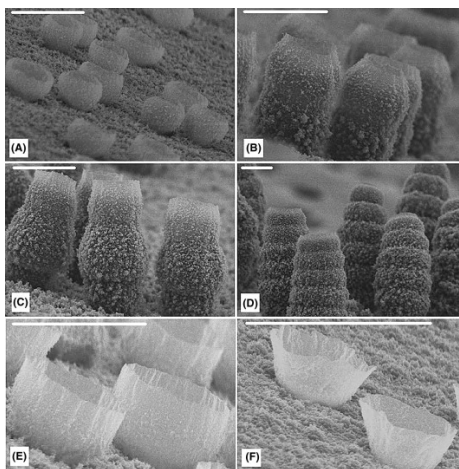
Figure 2.12: SEM images (scale bar 100 µm) of polypyrrole microcups achieved by electrochemical polymerization with soft-templates of suspended gas bubbles where the resultant structure can be tuned with adjustment of process parameters using a scan rate of 20 mV/s in the potential range of 0 V to 1.2 V for different cycles (A, 1; B, 2; C, 3; D, 7) or at different scan rates (E, $50\,\text{mV} \cdot \text{s}^{-1}$; F, $150\,\text{mV} \cdot \text{s}^{-1}$) for 3 cycles. © Qu et al. (2004) included with permission.

deposited structures (fig. 2.13)(Darmanin and Guittard, 2016; Szczepanski et al., 2016). The electrodeposition of CP hierarchical structures by gas bubble templating is very promising however adaptation for 3D substrates must be considered as the reported literature uses standard, planar working electrodes with high conductivity.

Other techniques have been employed to create hierarchical structures at the molecular level either through the addition of secondary dopants to create higher ordered structures or supramolecular templates to self-assemble monomers followed by polymerization (Frauenrath and Jahnke, 2008; Horii et al., 2018). These methods will be vital in creating highly ordered structures which demonstrate improved conductivity due to polymer chain alignment, but may not be well suited for deposition of structures.
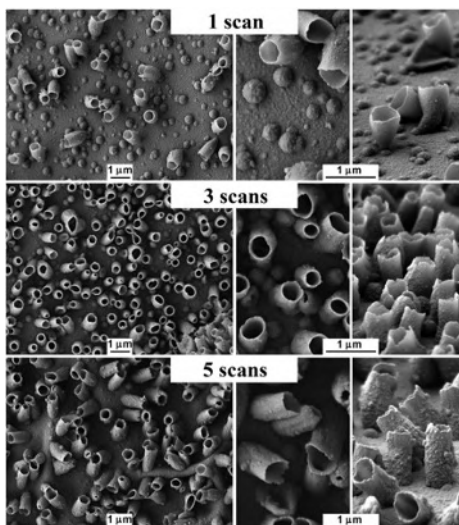
Figure 2.13: SEM images of PolyNaphDOT nanotubes fabricated electrodeposition at $10\,000\times$ without substrate inclination (left), and at $25\,000\times$ with substrate inclination (right), under different numbers of cyclic voltammetry scans show increased density of features with increasing cycles. © Darmanin and Guittard (2016) included with permission.

2.4   Chapter summary

This chapter has provided a review of CNTs as conductive fillers in PDMS composite materials, as well as techniques for improving the quality of CNT dispersions towards the fabrication of 3D EAP devices based upon PDMS-CNT composites. A review of CPs was discussed with a focus on PPy and PEDOT:PSS due to their promising application to 3D EAP devices. Existing AM techniques were discussed in reference to their applicability to the fabrication of 3D EAP devices. DIW into a support gel and vat polymerization were presented as techniques that have the greatest potential for 3D EAP structures. Finally, a review of techniques for the fabrication of hierarchical CP structures was provided and soft-template polymerization route was identified as a candidate for the post hoc deposition of CP structures on 3D substrates to create hierarchical features.

2.5   References

Abshirini, Mohammad, Mohammad Charara, Parisa Marashizadeh, Mrinal C. Saha, M. Cengiz Altan, and Yingtao Liu (2019). "Functional nanocomposites for 3D printing of stretchable and wearable sensors." In: *Applied Nanoscience* 9.8, pp. 2071–2083.

Ambrosi, Adriano and Martin Pumera (May 2016). "3D-printing technologies for electrochemical applications." English. In: *Chemical Society Reviews* 45.10, pp. 2740–2755.

Asmussen, Silvana, Gustavo Arenas, and Claudia Vallo (Aug. 2015). "Photopolymerization of pyrrole/methacrylate mixtures using α-cleavage type photoinitiators in combination with iodonium salt." In: *Synthetic Metals* 209, pp. 304–312.

Baughman, Ray H., Anvar A. Zakhidov, and Walt A. de Heer (Aug. 2002). "Carbon Nanotubes–the Route Toward Applications." In: *Science* 297, pp. 787–792.

Bhadra, Sambhu, Dipak Khastgir, Nikhil K Singha, and Joong Hee Lee (Aug. 2009). "Progress in preparation, processing and applications of polyaniline." English. In: *Progress in Polymer Science* 34.8, pp. 783–810.

Bliley, Jacqueline, Joshua Tashman, Maria Stang, Brian Coffin, Daniel Shiwarski, Andrew Lee, Thomas Hinton, and Adam Feinberg (2022). "FRESH 3D bioprinting a contractile heart tube using human stem cell-derived cardiomyocytes." In: *Biofabrication* 14.2, p. 024106.

Chu, Kunmo, Dongouk Kim, Yoonchul Sohn, Sangeui Lee, Changyoul Moon, and Sunghoon Park (May 2013). "Electrical and Thermal Properties of Carbon-Nanotube Composite for Flexible Electric Heating-Unit Applications." In: *IEEE Electron Device Letters* 34, pp. 668–670.

Committee, F42 (June 2012). Tech. rep. ASTM International, pp. 1–3.

Crowley, Karl, Eimer O'Malley, Aoife Morrin, Malcolm R. Smyth, and Anthony J. Killard (2008). "An aqueous ammonia sensor based on an inkjet-printed polyaniline nanoparticle-modified electrode." In: *Analyst* 133.3, pp. 391–399.

Cullen, Andrew T and Aaron D Price (2019). In: *Smart Materials and Structures* 28.10, p. 104007.

— (2018). "Digital light processing for the fabrication of 3D intrinsically conductive polymer structures." In: *Synthetic Metals* 235.

Darmanin, Thierry and Frédéric Guittard (2016). "A one-step electrodeposition of homogeneous and vertically aligned nanotubes with parahydrophobic properties (high water adhesion)." In: *Journal of Materials Chemistry A* 4.9, pp. 3197–3203.

Emon, Md Omar Faruk, Faez Alkadi, Daryl George Philip, Da-Hye Kim, Kyung-Chang Lee, and Jae-Won Choi (2019). "Multi-material 3D printing of a soft pressure sensor." In: 28, pp. 629–638.

Fekiri, Chaima, Ho Chan Kim, and In Hwan Lee (2020). "3D-Printable Carbon Nanotubes-Based Composite for Flexible Piezoresistive Sensors." In: *Materials* 13.23, p. 5482.

Frauenrath, Holger and Eike Jahnke (2008). "A general concept for the preparation of hierarchically structured pi-conjugated polymers." In: *Chemistry* 14.10, pp. 2942–2955.

Fukushima, Takanori, Atsuko Kosaka, Yohei Yamamoto, Takuji Aimiya, Shunsuke Notazawa, Toshikazu Takigawa, Tamotsu Inabe, and Takuzo Aida (2006). "Dramatic Effect of Dispersed Carbon Nanotubes on the Mechanical and Electroconductive Properties of Polymers Derived from Ionic Liquids." In: *Small* 2.4, pp. 554–560.

Gojny, F H, M H G Wichmann, U Köpke, B Fiedler, and K Schulte (Nov. 2004). "Carbon nanotube-reinforced epoxy-composites: enhanced stiffness and fracture toughness at low nanotube content." In: *Composites Science and Technology* 64.15, pp. 2363–2371.

Greco, Francesco, Alessandra Zucca, Silvia Taccola, Arianna Menciassi, Toshinori Fujie, Hiroki Haniuda, Shinji Takeoka, Paolo Dario, and Virgilio Mattoli (Nov. 2011). "Ultra-thin conductive free-standing PEDOT/PSS nanofilms." English. In: *Soft Matter* 7.22, pp. 10642–10650.

Gupta, Murari L, Stefanie A Sydlik, Jan M Schnorr, Dong Jin Woo, Sebastian Osswald, Timothy M Swager, and Dharmaraj Raghavan (Mar. 2013). English. In: *Journal of Polymer Science, Part B: Polymer Physics* 51.6, pp. 410–420.

Hinton, Thomas J, Quentin Jallerat, Rachelle N Palchesko, Joon Hyung Park, Martin S Grodzicki, Hao-Jan Shue, Mohamed H Ramadan, Andrew R Hudson, and Adam W Feinberg (2015). "Three-dimensional printing of complex biological structures by freeform reversible embedding of suspended hydrogels." English. In: *Science advances* 1.9, e1500758.

Hodko, Dalibor, Maria Gamboa-Aldeco, and Oliver J. Murphy (2009). "Photopolymerized silver-containing conducting polymer films. Part I. An electronic conductivity and cyclic voltammetric investigation." In: *Journal of Solid State Electrochemistry* 13.7.

Holness, F Benjamin and Aaron D Price (Jan. 2018). "Direct ink writing of 3D conductive polyaniline structures and rheological modelling." In: *Smart Materials and Structures* 27, p. 015006.

Horii, Tatsuhiro, Hanae Hikawa, Masato Katsunuma, and Hidenori Okuzaki (Mar. 2018). "Synthesis of highly conductive PEDOT:PSS and correlation with hierarchical structure." English. In: *Polymer* 140, pp. 33–38.

Ijeri, Vijaykumar S., Jijeesh R. Nair, Claudio Gerbaldi, Renato S. Gonnelli, Silvia Bodoardo, and Roberta M. Bongiovanni (2010). In: *Soft Matter* 6.19, pp. 4666–4668.

Jager, Edwin W. H., Elisabeth Smela, and Olle Inganäs (Nov. 2000). "Microfabricating Conjugated Polymer Actuators." English. In: *Science* 290.5496, pp. 1540–1545.

Jeon, Dae-Young, Heeju Kim, Min Wook Lee, So Jeong Park, and Gyu-Tae Kim (2019). "Piezo-impedance response of carbon nanotube/polydimethylsiloxane nanocomposites." In: *APL Materials* 7.4, p. 041118.

Kern, Jean-Marc and Jean-Pierre Sauvage (1989). "Photochemical deposition of electrically conducting polypyrrole." In: *J. Chem. Soc., Chem. Commun.* 10, pp. 657–658.

Kim, Jeong Hun, Ji-Young Hwang, Ha Ryeon Hwang, Han Seop Kim, Joong Hoon Lee, Jae-Won Seo, Ueon Sang Shin, and Sang-Hoon Lee (Jan. 2018). "Simple and cost-effective method of highly conductive and elastic carbon nanotube/ polydimethylsiloxane composite for wearable electronics." In: *Nature Publishing Group*, pp. 1–11.

Kirchmeyer, Stephan and Knud Reuter (2005). "Scientific importance, properties and growing applications of poly(3,4-ethylenedioxythiophene)." In: *J. Mater. Chem.* 15.21, pp. 2077–2088.

Li, Y B, B Q Wei, J Liang, Q Yu, and D H Wu (Feb. 1999). "Transformation of carbon nanotubes to nanoparticles by ball milling process." In: *Carbon* 37.3, pp. 493–497.

Liu, Chao-Xuan and Jin-Woo Choi (Oct. 2012). "Improved Dispersion of Carbon Nanotubes in Polymers at High Concentrations." In: *Nanomaterials* 2.4, pp. 329–347.

Ma, Peng-Cheng, Naveed A. Siddiqui, Gad Marom, and Jang-Kyo Kim (2010). *Dispersion and functionalization of carbon nanotubes for polymer-based nanocomposites: A review*. Vol. 41.

Michel, Taissa R., Michael J. Capasso, Muhammet E. Cavusoglu, Jeremy Decker, Danilo Zeppilli, Cheng Zhu, Smitesh Bakrania, Jennifer A. Kadlowec, and Wei Xue (Apr. 2020). "Evaluation of porous polydimethylsiloxane/carbon nanotubes (PDMS/CNTs) nanocomposites as piezoresistive sensor materials." In: *Microsystem Technologies* 26.4, pp. 1101–1112.

Mickelson, E T, C B Huffman, A G Rinzler, R E Smalley, R H Hauge, and J L Margrave (Oct. 1998). "Fluorination of single-wall carbon nanotubes." In: *Chemical Physics Letters* 296.1-2, pp. 188–194.

Mohandass, C, A S Vijayaraj, R Rajasabapathy, S Satheeshbabu, S V Rao, C Shiva, and I De-Mello (2012). "Biosynthesis of Silver Nanoparticles from Marine Seaweed Sargassum cinereum and their Antibacterial Activity." In: *Indian journal of pharmaceutical sciences* 75.5, pp. 606–10.

Murphy, Oliver J, G Duncan Hitchens, Bryan Dalibor, D Hodko, and Eric T Clarke (Apr. 2001). *Method of forming electronically conducting polymers on conducting and nonconducting substrates*. US-PATENT-6,210,537.

Otero, Toribio Fernández (Oct. 2017). "Artificial muscles driven by the cooperative actuation of electrochemical molecular machines. Persistent discrepancies and challenges." In: *International Journal of Smart and Nano Materials* 8.4, pp. 125–143.

Pei, Qibing, Guido Zuccarello, Markus Ahlskog, and Olle Inganäs (1994). "Electrochromic and highly stable poly(3,4-ethylenedioxythiophene) switches between opaque blue-black and transparent sky blue." In: *Polymer* 35.7, pp. 1347–1351.

Qu, Liangti, Gaoquan Shi, Jinying Yuan, Gaoyi Han, and Feng'en Chen (2004). "Preparation of polypyrrole microstructures by direct electrochemical oxidation of pyrrole in an aqueous solution of camphorsulfonic acid." In: *Journal of Electroanalytical Chemistry* 561 (SUPPL. 1).

Rabek, J. F., J. Lucki, M. Zuber, B. J. Qu, and W. F. Shi (1992). "Photopolymerization of Pyrrole Initiated by the Ferrocene- and Iron-Arene Salts-Chlorinated Solvents Complexes." In: *Journal of Macromolecular Science, Part A* 29.4-5, pp. 297–310.

Rajendran, Dhivakar, Bilel Ben Atitallah, Rajarajan Ramalingame, Roberto Bautista Quijano Jose, and Olfa Kanoun (2021). "Ultra Thin Nanocomposite In-Sole Pressure Sensor Matrix for Gait Analysis." In: *Advanced Sensors for Biomedical Applications*. Ed. by Olfa Kanoun and Nabil Derbel. Cham: Springer International Publishing, pp. 33–45.

Ramalingame, Rajarajan, Dhivakar Rajendran, Amoog Lakshmanan, and Olfa Kanoun (Mar. 2018). "Effect of Organic Solvent on MWCNT-PDMS Nanocomposite Based Capacitive Pressure Sensors." In: *2018 15th International Multi-Conference on Systems, Signals & Devices (SSD)*, pp. 1208–1211.

Sabouraud, Guillaume, Säid Sadki, and Nancy Brodie (2000). "The mechanisms of pyrrole electropolymerization." In: *Chemical Society Reviews* 29.5, pp. 283–293.

Saito, T., K. Matsushige, and K. Tanaka (Oct. 2002). "Chemical treatment and modification of multi-walled carbon nanotubes." In: *Physica B: Condensed Matter* 323.1-4, pp. 280–283.

Santino, Luciano M., Erica Hwang, Yifan Diao, Yang Lu, Hongmin Wang, Qisheng Jiang, Srikanth Singamaneni, and Julio M. D'Arcy (Nov. 2017). "Condensing Vapor Phase Polymerization (CVPP) of Electrochemically Capacitive and Stable Polypyrrole Microtubes." In: *ACS Applied Materials & Interfaces* 9.47, pp. 41496–41504.

Shirakawa, Hideki, Edwin J. Louis, Alan G. MacDiarmid, Chwan K. Chiang, and Alan J. Heeger (1977). "Synthesis of electrically conducting organic polymers: halogen derivatives of polyacetylene, (CH)." In: *J. Chem. Soc., Chem. Commun.* 16, pp. 578–580.

Snook, Graeme A., Pon Kao, and Adam S. Best (Jan. 2011). "Conducting-polymer-based supercapacitor devices and electrodes." In: *Journal of Power Sources* 196, pp. 1–12.

Spinks, Geoffrey M., Gursel Alici, Scott McGovern, Binbin Xi, and Gordon G. Wallace (2009). "Conjugated Polymer Actuators: Fundamentals." In: *Biomedical Applications of Electroactive Polymer Actuators*. John Wiley & Sons, Ltd. Chap. 10, pp. 193–227.

Szczepanski, Caroline R., Inès M'Jid, Thierry Darmanin, Guilhem Godeau, and Frédéric Guittard (2016). "A template-free approach to nanotube-decorated polymer surfaces using 3,4-phenylenedioxythiophene (PhEDOT) monomers." In: *Journal of Materials Chemistry A* 4.44, pp. 17308–17323.

Taccola, S, F Greco, B Mazzolai, V Mattoli, and E W H Jager (Nov. 2013). "Thin film free-standing PEDOT:PSS/SU8 bilayer microactuators." In: *Journal of Micromechanics and Microengineering* 23.11, p. 117004.

Taccola, Silvia, Francesco Greco, Edoardo Sinibaldi, Alessio Mondini, Barbara Mazzolai, and Virgilio Mattoli (Mar. 2015). "Toward a New Generation of Electrically Controllable Hygromorphic Soft Actuators." In: *Advanced Materials* 27.10, pp. 1668–1675.

Thostenson, Erik T, Zhifeng Ren, and Tsu-Wei Chou (2001). "Advances in the science and technology of carbon nanotubes and their composites: a review." In: *Composites Science and Technology* 61.13, pp. 1899–1912.

Ung, Benjamin S.-Y., Bo Weng, Roderick Shepherd, Derek Abbott, and Christophe Fumeaux (Sept. 2013). "Inkjet printed conductive polymer-based beam-splitters for terahertz applications." In: *Optical Materials Express* 3.9, p. 1242.

Xiao, Yinghong, Jianfei Che, Chang Ming Li, Chang Q. Sun, Yek T. Chua, Vee S. Lee, and John H.T. Luong (2007). "Preparation of nano-tentacle polypyrrole with pseudo-molecular template for ATP incorporation." In: *Journal of Biomedical Materials Research Part A* 80A.4, pp. 925–931.

Yamada, Katsumi, Yumiko Yamada, and Junji Sone (2014). "Three-dimensional photochemical microfabrication of poly(3,4-ethylene- dioxythiophene) in transparent polymer sheet." In: *Thin Solid Films* 554, pp. 102–105.

Chapter 3

Exploratory work toward fabrication of 3D EAP devices

This chapter will cover a selection of exploratory studies intended to identify a range of potential techniques and the applicability of this research. Initially, improvements in the material preparation of the PPy-BEMA-PEGMA photosensitive resin developed by Andrew T Cullen and Aaron D Price (2019) were investigated to identify the role of the preparation process, as well as the photoinitiator composition and concentration on the electrical conductivity of cured samples. The development of a PPy-BEMA-PEGMA photosensitive resin provided a promising outlook to the fabrication of 3D electroactive devices. The sensitivity to UV radiation of this formulation led to the idea that other radiation sources may also be effective in initiating polymerization of the PPy composite. In an effort to further reduce the diffusion path lengths, high-resolution electron beam irradiation was explored as a potential system for the fabrication of 3D EAP devices.

3.1 PPy-BEMA-PEGMA formulation investigation

As discussed in chapter 2, the photosensitive PPy-BEMA-PEGMA resin formulation used in this work was previously developed by Andrew T Cullen and Aaron D Price (2019). However, given the novelty of this resin design, it was necessary to explore

potential routes to improve the material properties of the resultant photopolymerized EAP devices. It was determined that to effectively use PPy-BEMA-PEGMA specimen as substrates for the post hoc deposition of hierarchical PPy structures, the electrical conductivity of the photopolymerized PPy-BEMA-PEGMA would need to be improved. Exploration of improvement to the PPy-BEMA-PEGMA electrical conductivity followed two main routes; modifications to the preparation procedure, and modifications to the photoinitiating system.

3.1.1 Process parameter effect on electrical conductivity

A critical component for the photopolymerization of PPy was the sensitization of the Ag^+ ions, a suspected limitation to the electrical conductivity observed previously was due to the poor solubility of silver nitrate in Py as evidenced by the formation of agglomerations of silver in fabricated PPy-BEMA-PEGMA specimen. The existing preparation method relied upon dissolution of silver nitrate in Py by vortex mixing. While this technique provided suitable mixing for well-refined silver nitrate crystals, it was apparent larger particles did not sufficiently dissolve. To overcome the poor solubility of silver nitrate in Py a probe homogenizer (Fisher) was employed to more effectively breakdown larger particles and increase the mechanical energy provided to aid in the dissolution of silver nitrate in Py, thus creating a higher concentration of Ag^+ ions available to participate in the polymerization reaction. Following this change in the material preparation process a 4-point probe conductivity of $1 \cdot 10^{-3}\,S \cdot cm^{-1}$ was recorded and compared to $3 \cdot 10^{-4}\,S \cdot cm^{-1}$ in the previous work showing the improved dissolution of silver nitrate led to an increase in electrical conductivity (Andrew T. Cullen and Aaron D. Price, 2018a).

The next stage in the material preparation process under investigation was the solvent employed to wash uncured resin from the photopolymerized samples. An investigation of standard solvents IPA and acetone was conducted. The standard resin

formulation consisting of 41.8 % (w/w) Py, 40 % (w/w) BEMA-PEGMA, 13.2 % (w/w), and 5 % (w/w) TPO was investigated. The resin formulation was mixed by probe homogenizer for 10 min and cast in PDMS moulds to fabricate ASTM D1708 tensile specimen. Curing was conducted under 405 nm UV LEDs for 20 min, where this UV range falls within the absorbance spectrum reported for TPO. Following curing, specimen were rinsed in either IPA or acetone and dried at ambient conditions for 48 h. Conductivity measurements were collected using a two-point measurement technique with the tensile specimen mounted in the tensile grips a known distance of 22 mm apart. The electrical conductivity (σ) of the specimen was calculated by:

$$\sigma = \frac{I \cdot L}{V \cdot A} \tag{3.1}$$

Where I is the set current, V is the measured potential difference, L is the sample length, and A is the cross-sectional area of the specimens. The results of these tests showed that the conductivity of tensile specimens rinsed in IPA was $(2.85 \pm 0.61) \cdot 10^{-4}\,\mathrm{S \cdot cm^{-1}}$ while specimen rinsed in acetone had conductivity of $(5.59 \pm 1.30) \cdot 10^{-5}\,\mathrm{S \cdot cm^{-1}}$. It was expected that the more aggressive solvent such as acetone more effectively removes any uncured Py in the BEMA-PEGMA matrix, whereas IPA sufficiently cleaned the surface of the sample while allowing any in-progress polymerization to continue during the drying process. Additionally, PPy has been shown to exhibit a decrease in conductivity when exposed to acetone vapours which could be contributing to the loss in conductivity observed here (Ruangchuay, Sirivat, and Schwank, 2004). The previous preparation method by Andrew T Cullen and Aaron D Price (2019) prescribed rinsing cured samples in acetone, based upon the improvements to electrical conductivity found in this study the preparation of PPy-BEMA-PEGMA structures throughout the rest of this work were rinsed in IPA.

3.1.2   Impact of photoinitiator on electrical conductivity

One potential issue with the PPy-BEMA-PEGMA formulation as previously developed was a disagreement between the polymerization rate of the BEMA-PEGMA and the PPy systems. Though the implementation of TPO as the sole photoinitiator in the resin formulation has yielded suitable results, an exploratory investigation into the potential for a two-component photoinitiation system was examined. First, an assessment of the single-photoinitiator system was investigated where the standard resin formulation was employed with the same materials and methods as described above, including rinsing the cured tensile specimen with IPA. To investigate the effect of TPO concentration on electrical conductivity, PPy-BEMA-PEGMA resin formulations were prepared with 0.5 % (w/w), 1 % (w/w), 3 % (w/w) and 5 % (w/w) of TPO where the BEMA-PEGMA concentration was maintained at 40 % and the Py and silver nitrate concentrations were varied while a molar ratio of $8 : 1$ was maintained. Samples were cured for, 1 min, 3 min, 5 min, 8 min, 10 min and 15 min to investigate the impact of photoinitiator concentration on the cure time. The 2-point resistance measurement method described above was employed to obtain the electrical properties of these cast PPy-BEMA-PEGMA tensile specimen. The average resistances of the specimen as a function of cure time is shown in fig. 3.1 where it can be seen that there was no obvious relationship between the curing time and measured resistance. However, examining the resistance by TPO concentration showed that samples from the 5 % TPO formulation exhibited the lowest measured resistance on average while also producing the most stable resistance across the range of curing times. Based on this exploratory test a TPO concentration of 5 % was maintained for future tests.

Following the investigation of the one-component photoinitiator system, a two-component photoinitiator system investigated was explored. The two-component system was based upon the concept of combining a radical photoinitiator with a
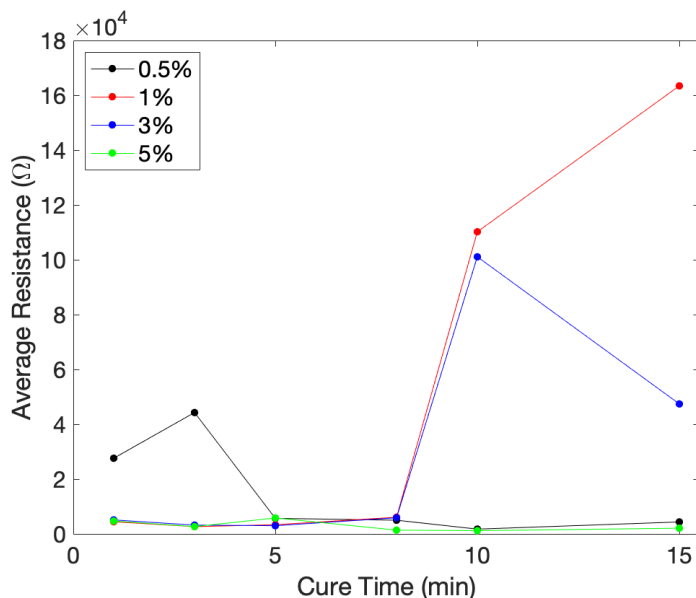
Figure 3.1: Average 2-point resistance measurements for cast PPy-BEMA-PEGMA tensile specimen show no clear relationship between photoinitator (TPO) concentration or cure time, however, specimen with 5 % (w/w) TPO demonstrated the most stable resistance measurements.

cationic photoinitiator where the methacrylate copolymers are polymerized by the free radical route and Py was polymerized by the cationic mechanism (Asmussen, Arenas, and Vallo, 2015). The PPy-BEMA-PEGMA formulation developed in the Organic Mechatronics and Smart Materials Laboratory employs TPO as the free radical photoinitator to polymerize the BEMA-PEGMA components while simultaneously sensitizing the silver ions to initiate the cationic polymerization of the Py monomer. A potential issue with this photoinitiation system was the observed disagreement between the polymerization of the BEMA-PEGMA copolymers when compared to the delayed polymerization of the PPy as observed by the translucent nature of samples immediately following curing which transitions to the black colour associated with PPy over approximately 24 h. Thus, to increase the polymerization rate of Py, a two-component photoinitiation system consisting of TPO and the onium salt (OS), p-(octyloxyphenyl)phenyliodonium hexafluoroantimonate (Ph_2ISbF_6), was investigated. The oniom salt (Ph_2ISbF_6), has had previous investigation in dual-

photoinitiation of Py and methacrylate composites with promising results, as such futher investigation is undertaken here (Asmussen, Arenas, and Vallo, 2015). The standard resin formulation was employed using a TPO concentration of 5 % (w/w) along with a two-component formulation consisting of 5 % (w/w) TPO and 5 % (w/w) Ph_2ISbF_6. Tensile specimens following ASTM D1708 ($n = 5$) were cast and cured for 20 min under 405 nm UV LEDs. Conductivity measurements were taken by placing 4-point probe on the top of each sample which was exposed to ambient conditions during curing, as well as on the bottom of the samples, which are contacting the PDMS mould surface. The average conductivity for these specimen is outlined in table 3.1. It can be seen that the single-component photoinitiator system resulted in higher conductivity on both top and bottom surfaces of the specimen in comparison to the two-component system. It is worth noting that the conductivity at the top of the cast films for the TPO specimen exhibited significantly higher conductivity than the bottom of the sample, this may be due to the disagreement in curing times for the BEMA-PEGMA and PPy components. In the work conducted by Ijeri et al. (2010), a dispersion of silver nanoparticles was also observed at the upper surface of photopolyermized PPy-BEMA films suggesting a lower electrical conductivity below the upper surface. The aim of this exploratory study was to improve the electrical conductivity of the formulation, therefore no further analysis was conducted on the two-component photoinitiator formulation. However, these samples did exhibit more uniform conductivity at the top and bottom of the cast samples suggesting a more uniform material composition. These samples also exhibited a more matte black surface in comparison to the TPO specimen, which may suggest a different morphology of PPy exists at the surface and is worthy of further investigation in future work.

Investigation into the process parameters and composition of the PPy-BEMA-PEGMA formulation have led to the improvement of the electrical conductivity of

Measurement location	5 % TPO, 0 % OS Conductivity ±SE $(S \cdot cm^{-1})$	5 % TPO, 5 % OS Conductivity ±SE $(S \cdot cm^{-1})$
Top	$(4.98 \pm 1.01) \cdot 10^{-4}$	$(1.920 \pm 0.018) \cdot 10^{-5}$
Bottom	$(1.150 \pm 0.021) \cdot 10^{-4}$	$(3.270 \pm 0.039) \cdot 10^{-5}$

Table 3.1: Conductivity of PPy-BEMA-PEGMA cast samples consisting of single or dual-photoinitiator systems.

cured samples. However, a main objective of this work is the fabrication of hierarchical structures composed of EAPs which may require further improvement to the PPy-BEMA-PEGMA electrical conductivity and will be explored in chapter 6 through the incorporation of CNTs to the polymer formulation.

3.2 Electron beam polymerization of PPy composites

The favourable actuation performance of PPy is well suited for microelectrochemical systems (MEMS). However, since typical PPy polymerization techniques such as electropolymerization, and chemical oxidative polymerization, are primarily limited to planar films or powders, alternative polymerization techniques have been explored. The development of a photosensitive PPy-BEMA-PEGMA resin formulation in the ultraviolet range lead to the idea that other radiation sources may be used to initiate photopolymerization of this resin formulation. In an effort to further reduce the diffusion path of potential devices this study introduces modifications to the PPy-BEMA-PEGMA formulation for use with electron beam lithography (EBL). EBL is a maskless lithography technique where a focused beam of electrons is used to expose a photoresist. A photoresist is a photosensitive polymer that is combined with a sensitizer and solvent to allow the proprieties of the resist to be modified by the

irradiation source and following exposure the pattern can be revealed by developing in the solvent. Classifications of photoresists are positive and negative, a positive photoresist will degrade upon exposure increasing the solubility of exposed regions to the solvent. Conversely, a negative photoresist will polymerize upon exposure making exposed regions less soluble to the solvent allowing the exposed regions to remain following developing (Barclay, 2001). EBL was an especially interesting lithography technique for the resolution capability in the sub 10 nm range making the direct fabrication of hierarchical features in the nanoscale achievable (Quero, Perdigones, and Aracil, 2018).

3.2.1 PPy negative photoresist development

A resin formulation with $8 : 1$ molar ratio of Py to silver nitrate, 5 % TPO, and 40 % BEMA-PEGMA in a 7:3 mass ratio blend was explored as a negative photoresist in the EBL process (Andrew T. Cullen and Aaron D. Price, 2018b). This formulation was combined with varying ratios of the solvent acetonitrile to lower the viscosity sufficiently for fabrication of thin films by a spin coating process. Film fabrication was conducted by spin coating onto corona treated glass or silicon wafers. Corona treatment was conducted using a high voltage corona discharge probe to increase the surface energy of the substrate surface and improve adhesion and wettability of the resin formulations to the substrate. Following preparation of the substrates, films were spin coated at speeds ranging from 500 rpm to 4000 rpm to optimize film thickness.

The development of the PPy-BEMA-PEGMA negative photoresist was initiated with the PPy-BEMA-PEGMA photosensitive formulation discussed above, however, in EBL the thickness of the resist layer can limit the resolution of the process or hinder proper function of the system. Typical EBL resist layers range from 200 nm to 500 nm with rare cases exploring resists up to 5 μm. During the spin coating process

it was determined that the viscosity of the resin formulation did not allow for creation of sufficiently thin films. To overcome this issue solvents were incorporated into the formulation to reduce the viscosity of the films and allow thinner films to be produced. The addition of 20 % acetonitrile to the PPy-BEMA-PEGMA formulation improved the quality of films produced by spin coating, but also highlighted an additional issue with this formulation where the BEMA-PEGMA copolymers do not sufficiently dry to use under high-vacuum. In the EBL process films must be stable under the high-vacuum conditions associated with scanning electron microscopy (SEM), as such the PPy-BEMA-PEGMA films could not be employed as negative photoresists.

In an attempt to overcome the volatility issues discovered with the PPy-BEMA-PEGMA formulation, the negative photoresist composition was simplified to include Py and silver nitrate in an $8 : 1$ molar ratio along with 5 % TPO. This formulation was diluted with acetonitrile to further lower the viscosity and reduce the thickness of the cast films. Films were spin coated at 1000 rpm and allowed to dry at ambient conditions for 48 h. During the drying process partial polymerization of the Py was observed as demonstrated by the development of semi-opaque films for both 20 % and 40 % acetonitrile films shown in fig. 3.2(a) and fig. 3.3. The surface morphology of the Py-AgNO$_3$ films was examined by SEM and is shown in fig. 3.2(c) and fig. 3.3(c). It can be seen that both films exhibit voids where the substrate was exposed but these regions are more prevalent in the 40 % acetonitrile film.

EDX analysis was conducted on the ambient cured Py-AgNO$_3$ films cast on a silicon wafer which showed the chemical composition of the films (fig. 3.4). This analysis demonstrated that there was a consistent dispersion of silver particles throughout the film along with larger islands of silver agglomerations. These silver particles, while playing a critical role in the polymerization of Py, likely also contribute to the electrical conductivity of the film. The final observation obtained from this study is shown in fig. 3.5 where it can be seen that the polymerization of Py was incomplete
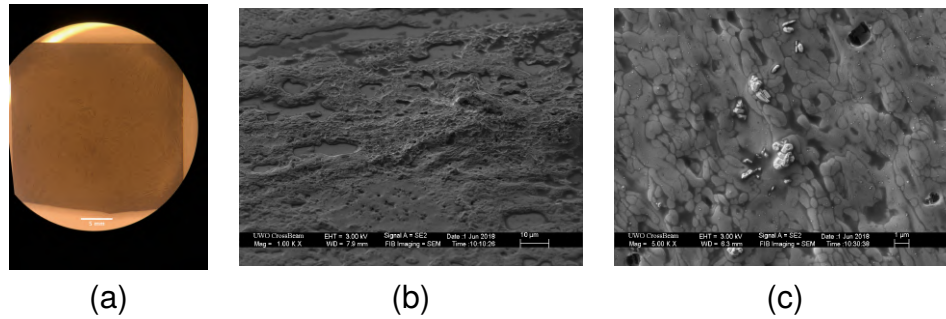
Figure 3.2: Optical microscopy images (a) and SEM images (b) of a photosensitive pyrrole and silver nitrate formulation diluted with 20 % (w/w) acetonitrile show a relatively coated surface with islands of silver particles.
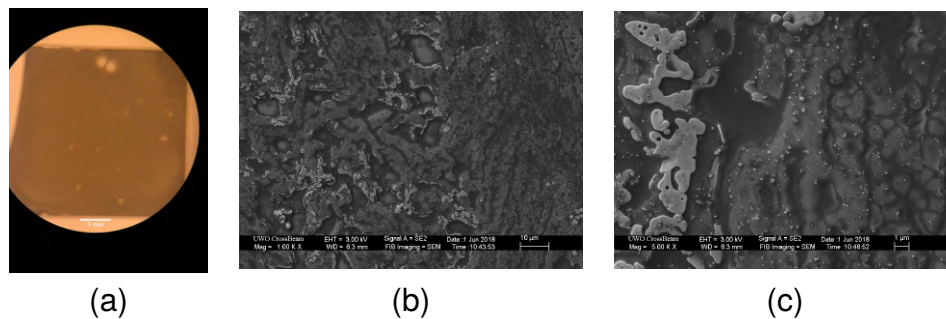
Figure 3.3: Optical microscopy images (a) and SEM images (b) of a photosensitive pyrrole and silver nitrate formulation diluted with 40 % (w/w) acetonitrile show a uneven film with clear porosities exposing the glass substrate below.
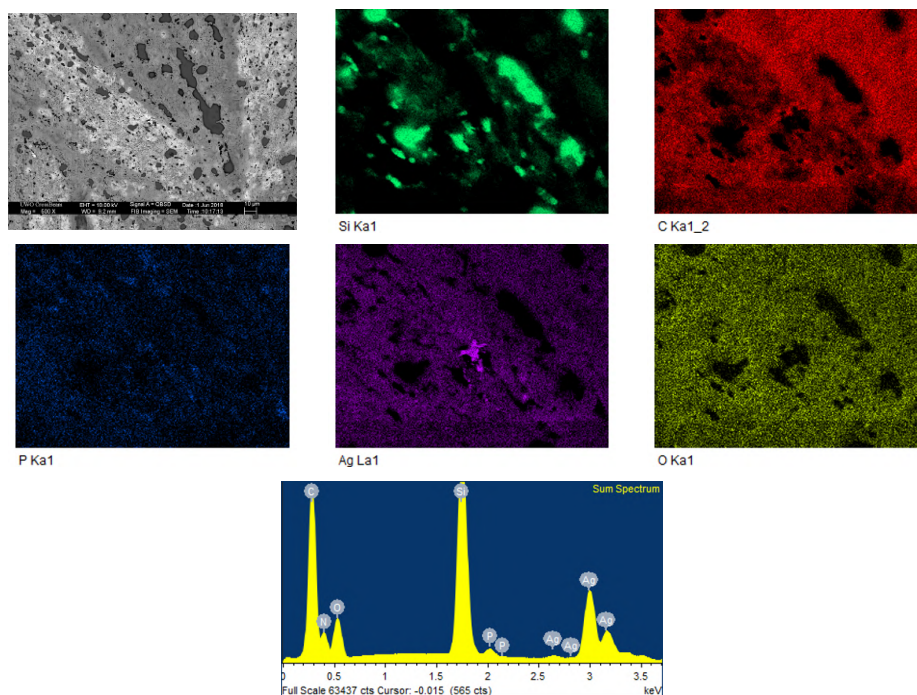
Figure 3.4:   Energy dispersive X-ray analysis results for the pyrrole-silver nitrate-TPO resin show even distribution of the pyrrole constituents however the poor film uniformity was highlighted by the exposure of the silicon substrate and the existence of silver islands suggest modifications to the preparation process are required.

due to the ablation of the film where it has been exposed to the electron beam of the SEM. This issue highlights the complexity of modifications required to develop a resin formulation suitable for EBL, and while a worthwhile endeavour, it is beyond the scope of this work. One potential route of investigation is the use of atmospheric SEM (ASEM) where liquid specimen can be examined under atmospheric conditions. Higuchi et al. (2015) successfully achieved the polymerization of PPy, and PANi nanorods with diameters of 200 nm by electron beam exposure in an ASEM system. While this technique may result in reduced resolution it may be the suitable next step in the fabrication of nanoscale PPy-BEMA-PEGMA composite structures.
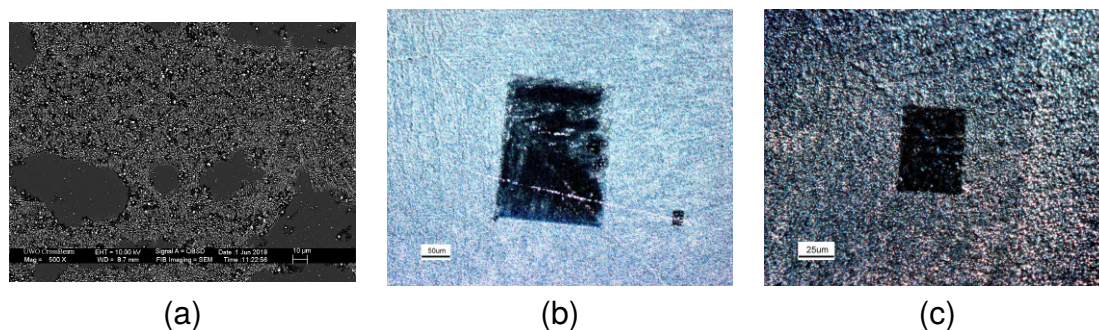
Figure 3.5: Comparison of SEM images of the pyrrole, silver nitrate, TPO polymer formulation in the cured (a) and uncured (b, c) states demonstrate that upon prolonged SEM irradiation the uncured films are ablated, exposing silicon substrate below and confirming the volatility of the formulation under SEM conditions.

3.3 Chapter summary

This chapter detailed the exploratory investigations undertaken in an effort to inform the direction of future work towards the development of hierarchical EAP structures. It was demonstrated that the electrical conductivity of the PPy-BEMA-PEGMA formulation was improved through homogenization of the Py-AgNO$_3$ solution and replacing the rinsing solvent with IPA rather than acetone. Investigations into the photoiniating system provided interesting results where no significant effect on cured PPy-BEMA-PEGA electrical conductivity was determined based upon TPO concentration and curing time. However, more stable electrical conductivity results were obtained with formulations containing 5 % (w/w) TPO. Exploration into a dual-photoiniating system leveraging both free radical and cationic polymerization mechanisms yielded PPy-BEMA-PEGMA samples with lower electrical conductivity but more consistent measurement data on the top and bottom of the film. Due to poor electrical conductivity, the dual-photoiniating system was not investigated further and it was determined that a single photoinitator, TPO, with a concentration of 5 % (w/w) would be suitable for further development of the PPy-BEMA-PEGMA resin formulation. Investigations into EBL as an alternative method for the photopolymer-

ization of PPy-BEMA-PEGMA structures on the nanoscale were unsuccessful due to the material instability under vacuum conditions. Additionally, a Py-AgNO$_3$-TPO resist was developed but stability issues remained as exhibited by the ablation of the film under SEM imaging. This chapter has provided insight to inform the future direction of this work as well as future projects in the field.

3.4   References

Asmussen, Silvana, Gustavo Arenas, and Claudia Vallo (Aug. 2015). "Photopolymerization of pyrrole/methacrylate mixtures using α-cleavage type photoinitiators in combination with iodonium salt." In: *Synthetic Metals* 209, pp. 304–312.

Barclay, G.G. (2001). "Photoresists, Specialty." In: *Encyclopedia of Materials: Science and Technology*. Ed. by K.H. Jürgen Buschow, Robert W. Cahn, Merton C. Flemings, Bernhard Ilschner, Edward J. Kramer, Subhash Mahajan, and Patrick Veyssière. Oxford: Elsevier, pp. 6978–6980.

Cullen, Andrew T and Aaron D Price (2019). In: *Smart Materials and Structures* 28.10, p. 104007.

— (2018a). "Digital light processing for the fabrication of 3D intrinsically conductive polymer structures." In: *Synthetic Metals* 235, pp. 34–41.

— (2018b). "Digital light processing for the fabrication of 3D intrinsically conductive polymer structures." In: *Synthetic Metals* 235.

Higuchi, Takeshi, Hidetoshi Nishiyama, Mitsuo Suga, Hirohmi Watanabe, Atsushi Takahara, and Hiroshi Jinnai (2015). "One-step nanopatterning of conjugated polymers by electron-beam-assisted electropolymerization." In: *Microscopy* 64.3, pp. 205–212.

Ijeri, Vijaykumar S., Jijeesh R. Nair, Claudio Gerbaldi, Renato S. Gonnelli, Silvia Bodoardo, and Roberta M. Bongiovanni (2010). In: *Soft Matter* 6.19, pp. 4666–4668.

Quero, José M., Francisco Perdigones, and Carmen Aracil (2018). "11 - Microfabrication technologies used for creating smart devices for industrial applications." In: *Smart Sensors and MEMs (Second Edition)*. Ed. by Stoyan Nihtianov and Antonio Luque. Second Edition. Woodhead Publishing Series in Electronic and Optical Materials. Woodhead Publishing, pp. 291–311.

Ruangchuay, Ladawan, Anuvat Sirivat, and Johannes Schwank (2004). "Electrical conductivity response of polypyrrole to acetone vapor: effect of dopant anions and interaction mechanisms." In: *Synthetic Metals* 140.1, pp. 15–21.

Chapter 4

Direct ink writing of PDMS-PEDOT:PSS arterial phantom actuators

As discussed in chapter 2, the fabrication of CP actuators has been limited to planar devices. To overcome these limitations and develop 3D CP actuators there is a requirement to further develop the fabrication of 3D substrates that can act as the passive layer in the CP actuator device. Consequently, this chapter investigates the development of 3D PDMS-PEDOT:PSS bilayer actuators. The first stage of this process is to refine the fabrication of complex 3D PDMS structures. In this work, DIW in combination with a carbomer support gel is employed to fully support the uncured extruded PDMS while curing. The support of the carbomer gel enables the printing of overhanging features that would not otherwise be possible. The fabrication of patient-specific arterial phantoms for particle image velocimetry (PIV) were fabricated. Subsequently, the fabrication of bilayer PDMS-PEDOT:PSS actuators was investigated for planar cast PDMS films and non-planar DIW PDMS structures with the aim of developing phantom vascular networks equipped with addressable actuators for fluid pumping or simulation of stenosis and dilation of the artery.

4.1 Materials and Methods

4.1.1 Chemicals

The PDMS elastomer used in this study is Sylgard 184 (Dow Corning). This is a 2-part system consisting of the elastomer base and curing agent, a mixing ratio of 10:1 base to curing agent was employed. Carbopol 940 (Lubrizol) was used as the support gel. The PEDOT:PSS used in actuator fabrication is commercially available 1.3% PEDOT:PSS in aqueous solution (Sigma Aldrich), surfactants fluorosurfactant FC-4430 (3M), and Triton X-100 (Sigma Aldrich). Dimethyl sulfoxide (DMSO), ethylene glycol (EG) and sodium hydroxide (NaOH) were used as received (Sigma Aldrich).

4.1.2 PDMS arterial phantom fabrication

The fabrication process is enabled by the application of a modified fused filament fabrication (FFF) 3D printer (DeltaMaker) that was equipped with a CNC pneumatic valve (Nordson EFD) to accurately control extrusion pressures and locations (fig. 4.1a) (Holness and Price, 2018). Extrusion paths are generated via conventional AM slicing software enabling the adjustment of process parameters, and simple creation of GCODE files containing toolpath and extruder signals. This GCODE file is then loaded onto the 3D printer control board and executed to control the toolhead position. The signal normally designated to extrude filament is then passed to an external microcontroller, which processes the extruder signal and controls the pneumatic valve to dispense material as required. Several test models were fabricated to calibrate the system, assess print fidelity, and identify the process parameters required to fabricate complex 3D structures. Initial calibration of the process was conducted on circular tube modelled with a diameter of 8 mm and

height of 10 mm. Overhanging features and print fidelity were tested on a simplified tube bifurcation with tube diameters of 8 mm and total height of 20 mm as well as on a constricted tube model which had an initial diameter of 30 mm that constricted down to 15 mm before returning to the initial diameter over a 10 mm length. Finally, the capability of the system to reproduce complex structures was analyzed by fabricating a bifurcated carotid artery (BCA) model. Currently, arterial phantoms for PIV flow imaging are fabricated by lost-core casting in a micro-machined mould which when compared to DIW requires significant cost and time resources (Smith, Rutt, and D W Holdsworth, 1999). The model was obtained from a computed tomography scan of patient's carotid artery and was modified for the fabrication process by reducing the overall length to the highly featured region of the bifurcation. Additionally, a flange connecting the internal and external carotid arteries was added to allow the fabrication process to be completed with a single extrusion. All models were fabricated with a metal nozzle of diameter 250 µm and length 38 mm. Toolhead speeds and extrusion pressures were varied to assess print quality.

During the printing process, the PDMS was extruded into a carbomer gel. The carbomer gel was prepared by dispersing various weight ratios of powdered carbomer, Carbopol 940, in water using an overhead mixer Eurostar 60 Control (IKA). After mixing, the carbomer solution was transferred into the printing vessels and the pH of each vessel was adjusted to approximately pH 7 using an aqueous sodium hydroxide solution ($3.5 \, \text{mol} \cdot \text{L}^{-1}$). Neutralization of the carbomer solution causes the carbomer polymer chains to swell resulting in a significant increase in viscosity. The final viscosity of the solution is controlled by the concentration of carbomer in the solution (Jin et al., 2016). These carbomer solutions are then thoroughly mixed and degassed in a planetary mixer, DAC 330-100 SE (SpeedMixer), to ensure consistent mechanical properties and to minimize voids to prevent the extruded material from flowing post-printing. The carbomer gel behaves as a Bingham plastic, deforming

(a)   (b)
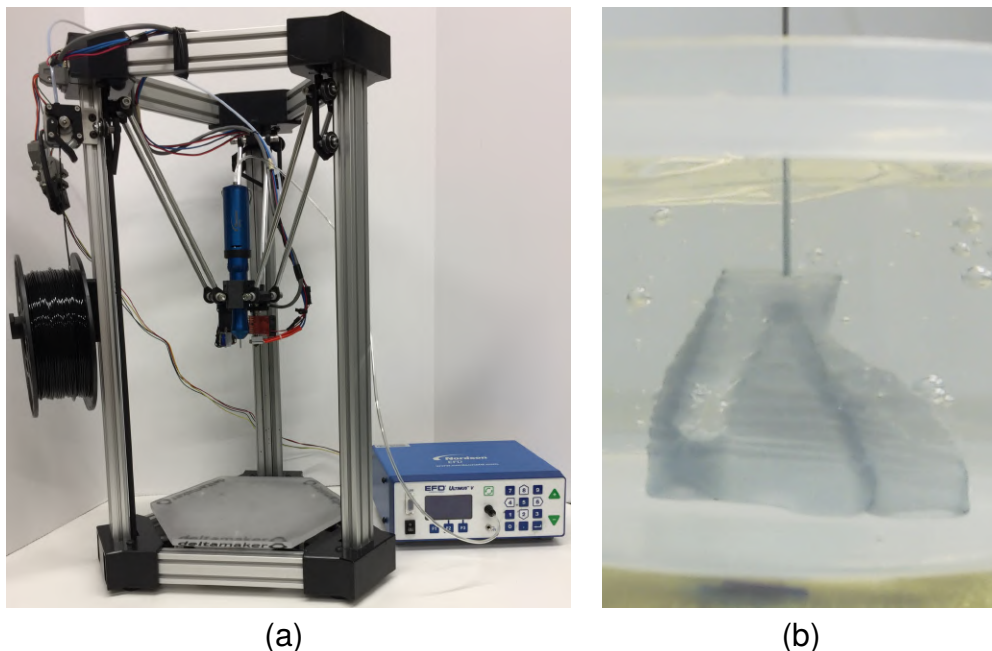
Figure 4.1: (a) Modified FFF delta robot equipped with pneumatic paste extrusion system and (b) PDMS arterial phantom fabrication in Carbopol support gel (PDMS dyed for imaging).

under the shear stress of the nozzle but maintaining its shape in a zero stress state (see fig. 4.1b). As a result, the nozzle can move freely through the gel but the extruded PDMS is fully supported (Hinton et al., 2015). Following extrusion, fabricated samples are cured for 12 h at 70 °C. Once cured, the samples are removed from the support gel by addition of the sodium chloride which lowers the viscosity of the gel allowing for easy removal and washing of the PDMS part.

4.1.3   PEDOT:PSS Films

One of the challenges associated with the fabrication of bilayer PDMS-PEDOT:PSS actuators is the interaction of the hydrophobic PDMS surface and the aqueous PEDOT:PSS solution. To investigate this interaction, various surface treatments and formulation compositions were studied. The surface treatment methods employed included the use of an UV ozone cleaner (UVOCS Inc.) and a handheld laboratory

corona treater (Electro-Technic Products Inc.). Both of these methods increase the PDMS film surface energy through the creation of ozone which reacts with the film's surface to create high energy oxide groups and improve the hydrophilic properties of the surface (Sun, Zhang, and Wadsworth, 1999). The formulation composition was studied by introducing alternative secondary dopants and surfactants. The first formulation used a combination of DMSO and FC-4430 as dopant and surfactant and the second formulation investigated a combination of EG and and Trition X-100 (Cruz-Cruz et al., 2010) as dopant and surfactant. These formulations were used to prepare films that were subsequently exposed to UV-ozone cleaning. After UV-ozone treatment the wettability of the films surface was characterized by measuring the contact angle of a single droplet (DSA30E Drop Shape Analyzer). In both cases the PEDOT:PSS formulation was thoroughly mixed, ultrasonicated for 30 min (Branson) and used immediately.

Based on the work of Silvia Taccola et al. (2015), spin coating was employed to fabricate bilayer PDMS-PEDOT:PSS films. First, PDMS films were cast by spin coating on a glass substrate at 500 rpm for 60 s, successive PEDOT:PSS layers were then spin coated at 2000 rpm. Between each layer, the films were exposed to an ozone treatment and annealed in an oven at 170 °C. The second fabrication technique employed was spray coating an identical PEDOT:PSS formulation directly onto 3D PDMS structures. The coating was applied using an air brush (Iwata), equipped with a 0.5 mm nozzle, to lightly coat samples with 4 layers of PEDOT:PSS. The films were annealed at 170 °C between the application of successive layers. Finally, conductivity of the films were measured for different dopant concentrations using the 4-point probe technique with a custom test stand connected to a Keithley 2611 sourcemeter.

4.2   Results and Discussion

4.2.1   PDMS structures and arterial phantoms

To calibrate the fabrication parameters for the process, a tube structure was modelled with a diameter of 8 mm and height of 10 mm, and sliced at 200 µm, the tube wall is comprised of a single extrusion width (fig. 4.2). Initial assessment of the geometric accuracy was performed using ImageJ. The printed structure was found to be smaller than modelled with an outer diameter of 7.8 mm and height of 9.7 mm. As previously mentioned, the nozzle diameter of 250 µm was used and the tube walls were expected to be one extrusion width. However, the tube wall thickness was measured to be approximately 820 µm. The significant disparity between nozzle diameter and extrusion width is due to increased extrusion pressure required to achieve sufficient layer adhesion. In tests with a programmed layer thicknesses varying from 200 µm to 400 µm, wall failures were observed using layer thicknesses above 300 µm, suggesting that over extrusion is required to achieve sufficient layer adhesion. The over extrusion of PDMS enables good adhesion between successive layers but appears to have negative effects on the surface finish of the resultant structures. Figure 4.3 shows a rippling effect on the outer surface of the structure and a section view (not pictured) revealed that the same effect is present on the interior wall of the tube. This is highly undesirable due to the potential impact of the surface irregularities on the flow characteristics through a phantom artery and the added difficulty of achieving a uniform electroactive polymer coating on the uneven surface. There appears to be some layer effects in the expected 200 µm range in accordance with modelled layer thickness, however, there is also a ridge-valley structure visible with a total thickness of approximately 800 µm and a peak-valley height of 145 µm. This undulating structure may be explained due the over-extrusion of PDMS being injected into previously deposited material. Despite the irregularities
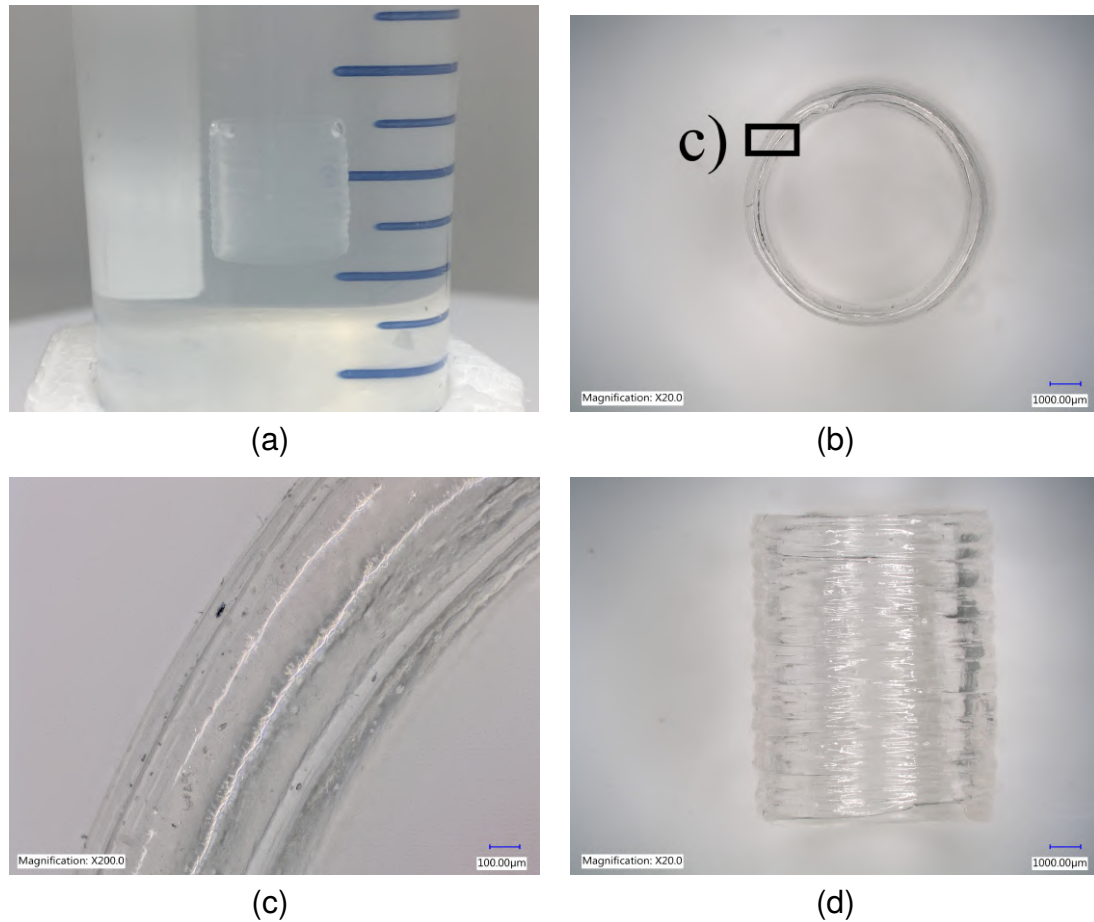
Figure 4.2: A PDMS calibration tube with a diameter of 8 mm and height of 10 mm was fabricated by DIW into carbomer support and is shown in a) uncured PDMS calibration tube in carbomer, b) and c) top views and d) front view of released structure. Images of released tube structure were used for validation of print fidelity in ImageJ.

of the surface, the fabrication method is capable of producing flexible, transparent, single-wall PDMS tubes as a basis for expansion to more complex geometries. After reliably producing the calibration structures more complex geometries were attempted using single walled cones that were easily reproducible with overhanging angles up to 30° (fig. 4.4).

The next stage in the DIW process development was to attempt the fabrication of highly complex, patient-specific vascular structures. Figure 4.5(a) and (b) show the 3D model of the modified segment of the BCA and the fabricated 3D PDMS
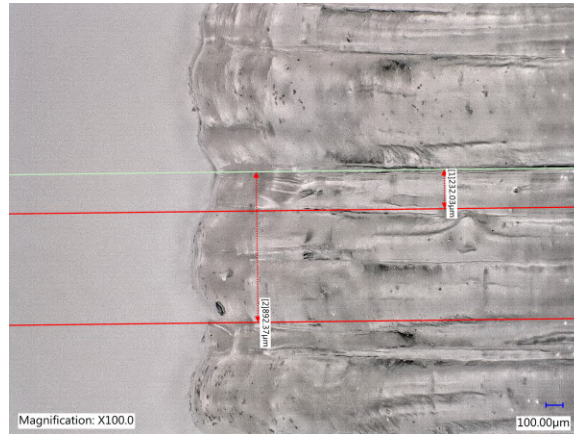
Figure 4.3: The layered structure of the DIW PDMS calibration tube demonstrates surface variations at heights significantly larger than the prescribed layer height of 200 µm.
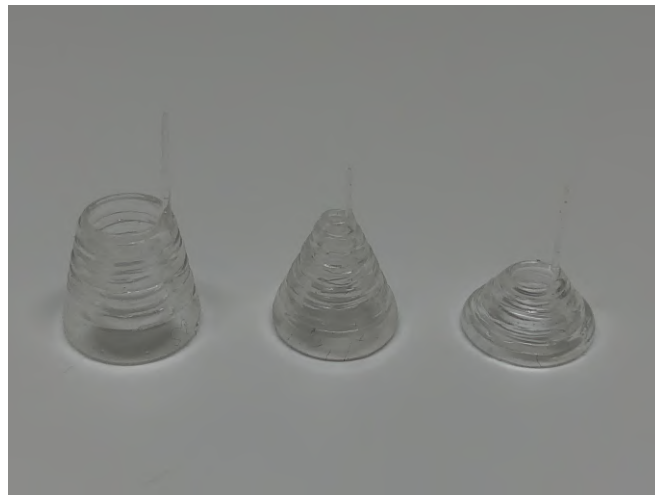
Figure 4.4: Fabrication of PDMS cones with incline angles of 10°, 20° and 30° demonstrate the carbomer gel is capable of supporting steep overhanging PDMS structures without introduction of wall defects.

replica of this structure. It can be seen that the PDMS structure exhibits significant wall failure defects and at this time it was determined that the DeltaMaker 3D printer was not maintaining the programmed print speed throughout the printing process which could be creating irregularities in the extrusion width and causing these failures. Notwithstanding the fact that these wall defects would not allow use of these structures as arterial phantoms preliminary investigation into the optical properties of the DIW structures was examined. Optical clarity of these structures is a critical factor in PIV analysis as any optical aberrations can introduce errors into the measurement system (Kefayati, David W Holdsworth, and Poepping, 2014). Figure 4.5(c) shows the PDMS BCA structure placed in a refractive index matching fluid along with no obvious distortion of the image behind the PDMS BCA structure (Poepping, Rankin, and David W Holdsworth, 2010). While improvements to the DIW process are required to fabricate structures of higher complexity, there are positive indicators that the surface roughness associated with the DIW structures will not significantly alter the optical properties of the printed component. This suggests that the technique may be used to prepare arterial phantoms for PIV analysis. However, successful implementation of DIW for the fabrication of patient specific arterial phantoms requires both improved surface roughness to limit optical aberrations as well as improved geometric fidelity to ensure an accurate model is produced.

As a result of discovering speed control issues with the DeltaMaker system a new motion system was adopted by retrofitting a paste extrusion fixture to a Prusa MK3S FFF 3D printer (Prusa Research). While this system was not equipped with automatic triggering of paste extrusion it provided reliable motion and in combination with manual extrusion to reliably print single extrusion models (i.e. without any interruptions in the extrusion once commenced). Figure 4.6 demonstrates the improvements achieved using the new motion system through the replication of a simplified bifurcated tube structure with 2 hollow tubes combining to 1. This demon-

(a)   (b)   (c)
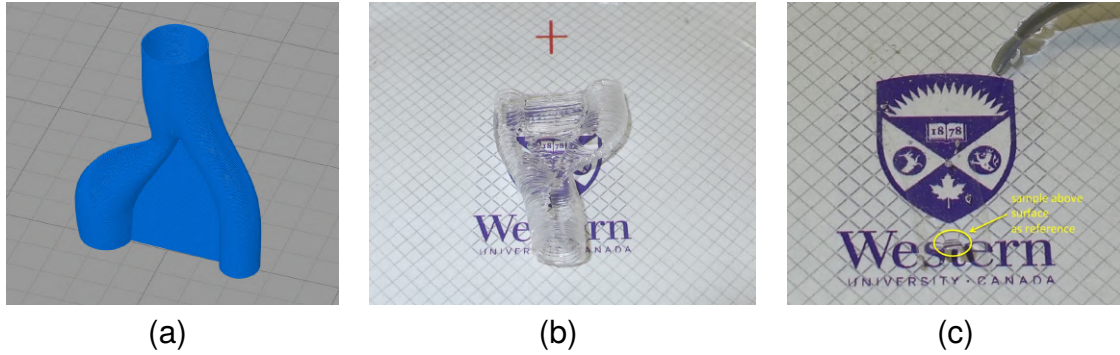
Figure 4.5: The fabrication of a bifurcated arterial phantom model (a) by DIW demon-
strated significant wall defects upon release from the carbomer gel (b), however
the surface roughness associated with the DIW process did not introduce optical
aberrations when the printed phantom was submerged in refractive index matching
fluid (c).

strates the potential to fabricate more complex vascular networks. The fabrication

of a constricted tube model demonstrates the capability to create steep overhanging

features as they can be easily supported by the carbomer gel. Samples fabricated

on the Prusa DIW system exhibited superior surface quality to previous examples,

however, some evidence of poor surface quality due to over-extrusion is still evident.

Further investigation of single PDMS extrusions demonstrated that for a print

speed of $10\,\mathrm{mm\cdot s^{-1}}$ and pressure of $35\,\mathrm{psi}$ the extrusion has an elliptical cross-

section with an approximate height of $555\,\mathrm{\mu m}$ and width of $340\,\mathrm{\mu m}$. As a result,

the slicing parameters were adjusted to have a layer height of $350\,\mathrm{\mu m}$. This height

provided sufficient overlap between successive layers to ensure sufficient adhe-

sion, while resulting in a smoother surface finish compared to analogous additive

manufacturing processes. Figure 4.7 shows the results of the updated printing

parameters in replication of the constricted tube model, demonstrating vastly im-

proved surface finish with regular layer effects at length scales associate with the

prescribed layer thickness. Layer effects were measured by optical microscopy

for using the image shown in fig. 4.7(b), where there average layer thickness was

$(346.8 \pm 12.0)\,\mathrm{\mu m}$ ($n = 6$). A limitation of these settings is that the aspect ratio of a

(a)   (b)
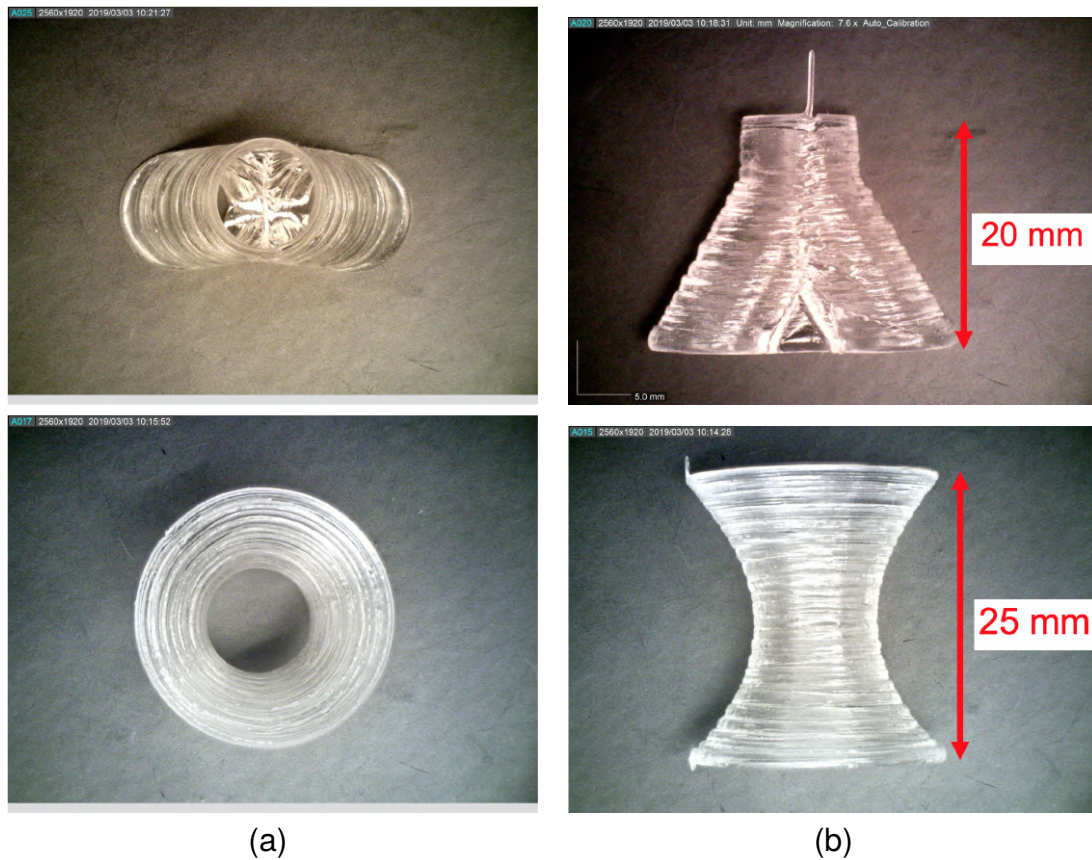
Figure 4.6: Through replacement of the motion system to the Prusa MK3 the PDMS DIW process was able to produce more complex geometries free of voids in the walls shown by, a) a constricted tube model with overhanging features, and b) a simplified bifurcated tube model.

(a)   (b)
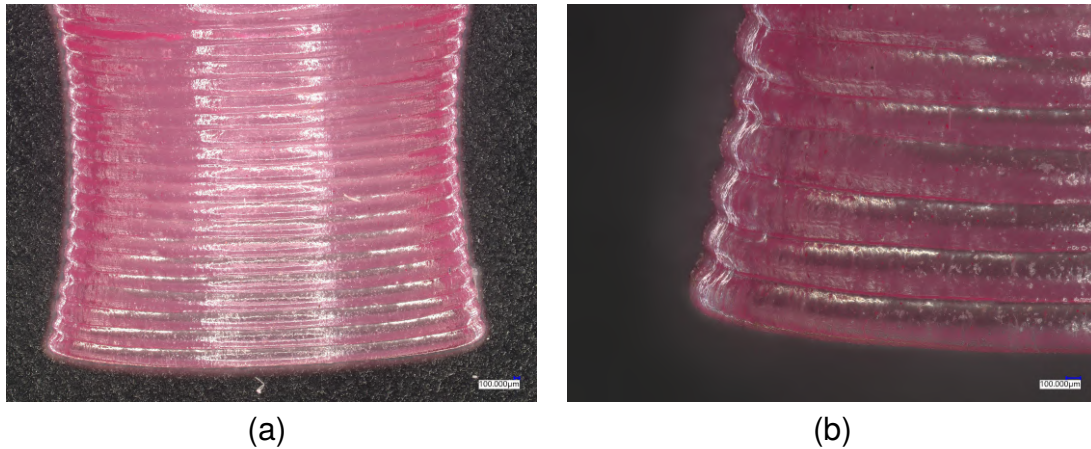
Figure 4.7:   Fabrication of 3D PDMS structures was optimized by adjustment of the print speed, extrusion pressure, and layer thickness to achieve a higher quality surface finish and resulting in less pronounced visibility of layer effects shown by optical microscopy at a) 20×, and b) 50×.

single extrusion skewing to the vertical dimension creates a lower angle of achievable overhang for a single-walled structure. This is illustrated in fig. 4.7 by the failure of the constricted tube model at the steeper angled portion of the model.

Currently, through a modification of programmed process settings it is a possible to achieve either a more refined surface finish for structures with low overhanging features or sacrifice surface quality to produce structures with steeper overhangs. These results demonstrate improved surface quality in tubular structures compared to that of Abdollahi et al. (2018), where an expert-guided optimization study was conducted to improve the quality of printed PDMS structures, however, similar defects are observed for more complex structures. A potential route for improvement of this process is to study a range of materials which may produce more complex 3D structures without defects.

4.2.2   PDMS-PEDOT:PSS film characterization

To identify the impact of secondary dopant and surfactant selection on the wettability of the PEDOT:PSS formulation 2 batches were investigated. The first formulation consisted of 5 % (w/w) DMSO, 1 % (w/w) FC440, and 94 % (w/w) PEDOT:PSS solution, while the second formulation used 5 % (w/w) EG, 0.5 % (w/w), and 93.5 % (w/w) PEDOT:PSS solution (Okuzaki, 2012; Taccola et al., 2013). Surfactant ratios were selected to avoid foaming during mixing while secondary dopant concentrations were kept equal. Following treatment of PDMS films in the UV ozone cleaner for 0 min, 5 min, 10 min, 20 min and 30 min the contact angle of a single droplet of PEDOT:PSS solution on the treated PDMS films was measured. Analysis of the droplets show that both formulations provided stable contact angle over time. Over the 1 min measuring time period, the DMSO formulation showed greater change in contact angle. Figure 4.8 shows that for each exposure time the DMSO-FC4430 formulation out-performed the EG-X100 combination and was more significantly affected by the increased UV exposure time. After demonstrating superior wettability, the DMSO-FC4430 formulation was investigated in more detail to improve the electrical properties of the formulation.

To test the impact of secondary dopant concentration, PDMS-PEDOT:PSS actuators were prepared as previously described consisting of 12 successive layers of PEDOT:PSS with the addition as a secondary dopant in either 5 % (w/w) or 17 % (w/w). It was shown that actuators containing 17 % (w/w) DMSO demonstrated conductivity of $(1.8 \pm 0.1) \cdot 10^{-3}\,\mathrm{S \cdot cm^{-1}}$ compared to $(9 \pm 2) \cdot 10^{-4}\,\mathrm{S \cdot cm^{-1}}$ for the 5 % DMSO composition. This increase in conductivity with secondary dopant concentration is in agreement with previous reported behaviour however conductivities achieved here remain lower than the product specification (Cruz-Cruz et al., 2010; Horii et al., 2018). Examination of the actuators by optical microscopy revealed an irregular film consisting of small islands rather than a continuous film. The inability to form a
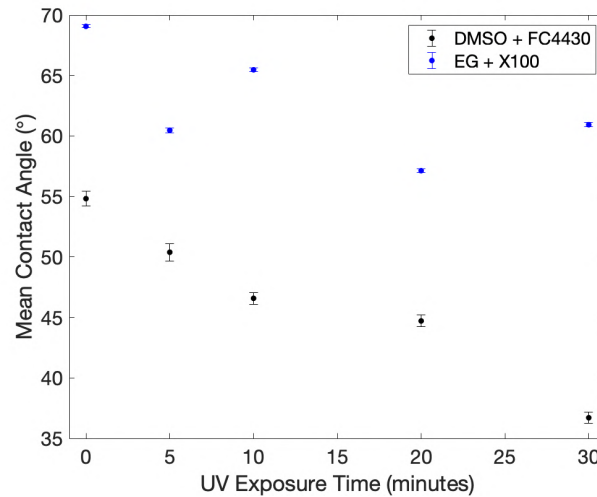
Figure 4.8: PEDOT:PSS solutions containing secondary dopant and surfactant combinations of either DMSO and FC4430 or EG and Triton X100 both demonstrated a reduction in contact, angle indicating improved wettability, with increased UV cleaning of the substrate. However, the solution containing DMSO and FC4430 provided lower contact angle measurements at each exposure time.

continuous film results in poor wettabillity of the PEDOT:PSS solution and prevents the resulting devices from reaching their full potential (fig. 4.9).

Nevertheless, PEDOT:PSS films, actuators were cut into a 4 mm × 5 mm sections and fixtured using spring clips acting as both mechanical supports and electrodes. A potential difference of 20 V was applied between electrodes, but due to the low conductivity of the actuator no motion was observed. To validate the concept of the actuator an external heat source was used to quickly heat the actuator to approximately 120 °C and thermomechanical actuation was observed with an approximate angular stroke of 24° (fig. 4.10). The actuation of the film demonstrates that the current PEDOT:PSS formulation could be used in the future to prepare actuators if the film uniformity can be improved.

(a)   (b)
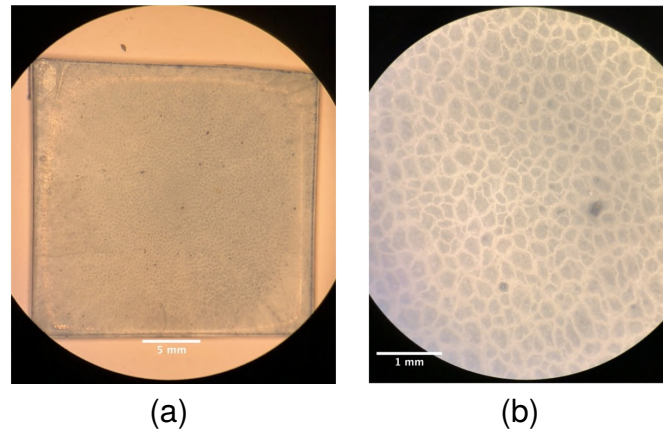
Figure 4.9: (a)Optical microscopy of bilayer PDMS-PEDOT:PSS shows inconsistent film morphology where the existence of PEDOT:PSS islands is clearly visible at higher magnificaiton (b).

(a)   (b)   (c)
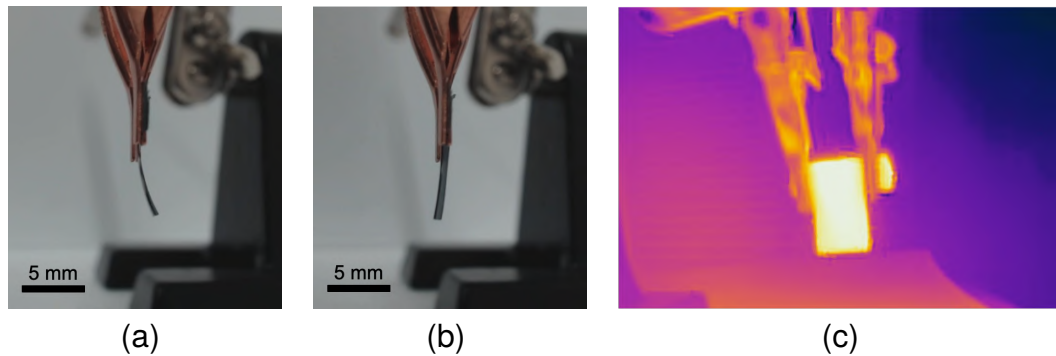
Figure 4.10: An external heat source was applied to a (4 mm × 5 mm spin coated PEDOT:PSS-PDMS bilayer actuator to demonstrate the thermomechanical actuation which can be seen by the change in bending angle in the (a) relaxed, and b) contracted states. Infrared imaging was used to measure peak temperatures of 120 °C (c).

4.2.3   3D PDMS-PEDOT:PSS actuators

Towards fabrication of 3D PEDOT:PSS-PDMS actuators the feasibility of coating the 3D printed surface was assessed. A wall of a 3D printed PDMS square tube model was cut and mounted to provide a flat section which could be more easily handled and coated. Figure 4.11 shows an example of an uncoated printed structure and a printed structure that was spray coated with 4 layers of the PEDOT:PSS formulation. While, these sections could be evenly coated, the manual nature of the spray process made achieving thin films on the required scale challenging. However, spray coating offers the potential to provide an even film on the curved surfaces of printed samples as demonstrated by the coating of a semicircular tube with a diameter of 10 mm (fig. 4.12a). However, due to their thickness, spray coated films demonstrated a tendency to crack, and were no longer transparent, further reinforcing the need to automate the spray coating process (fig. 4.12b). Spray coating remains a promising application technique for PEDOT:PSS films, however, a coating system which allows for more fine control should be investigated. Improved flow control would allow for deposition of thin films and avoiding the observed cracking due to large film thicknesses. Further control in the PEDOT:PSS deposition process maybe be acheived through aerosol printing systems where the atomized solution can be deposited in distinct traces to directly produces electroactive films with complex structures (Tarabella et al., 2020).

(a)   (b)   (c)
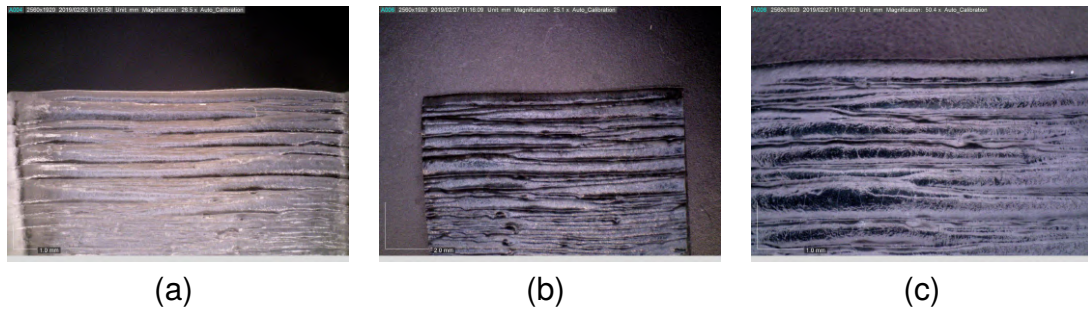
Figure 4.11: Printed square tubes were sectioned to provide a flat sample to characterize the spray coating process on the rough surface of printed samples (before (a) and after (b, c) coating) the opacity and cracking of the coated samples indicate deposited PEDOT:PSS layers are too thick.

(a)   (b)

Figure 4.12: The spray coating of PEDOT:PSS onto a curved section of 3D DIW circular tube demonstrates a uniform coating accommodating both the curvature and surface roughness, however, PEDOT:PSS film cracking indicates the spray coating process requires further modification to produce thinner layers.

4.3   Chapter summary

This chapter developed a DIW process that used a carbomer support bath to realize the fabrication of 3D PDMS structures. Refinement of the fabrication process parameters and apparatus resulted in the production of high-quality tubular structures with steep overhanging features and minimal sacrifices to surface finish. The DIW was used to fabricate patient-specific arterial phantoms and preliminary tests demonstrated that the optical properties of DIW structures were suitable for further evaluation. However, wall defects in the complex BCA structure indicated that further refinement of the DIW process is required for more complex geometries. Finally, the fabrication of 3D PDMS-PEDOT:PSS actuators was explored through the deposition of a custom PEDOT:PSS formulation on both planar and 3D PDMS structures. Further work is required in the improvement of the PEDOT:PSS film quality and to develop alternative approaches to coat 3D structures. This chapter achieved the objective of further development of AM approaches for fabrication of passive 3D structures for use in EAP devices.

4.4   References

Abdollahi, Sara, Alexander Davis, John H Miller, and Adam W Feinberg (2018). "Expert-guided optimization for 3D printing of soft and liquid materials." English. In: *PLoS ONE* 13.4. Ed. by Feng Zhao, e0194890.

Cruz-Cruz, I, M Reyes-Reyes, M A Aguilar-Frutis, A G Rodriguez, and R Lopez-Sandoval (July 2010). "Study of the effect of DMSO concentration on the thickness of the PSS insulating barrier in PEDOT:PSS thin films." English. In: *Synthetic Metals* 160.13-14, pp. 1501–1506.

Hinton, Thomas J, Quentin Jallerat, Rachelle N Palchesko, Joon Hyung Park, Martin S Grodzicki, Hao-Jan Shue, Mohamed H Ramadan, Andrew R Hudson, and Adam W Feinberg (2015). "Three-dimensional printing of complex biological structures by freeform reversible embedding of suspended hydrogels." English. In: *Science advances* 1.9, e1500758.

Holness, F Benjamin and Aaron D Price (Jan. 2018). "Direct ink writing of 3D conductive polyaniline structures and rheological modelling." In: *Smart Materials and Structures* 27, p. 015006.

Horii, Tatsuhiro, Hanae Hikawa, Masato Katsunuma, and Hidenori Okuzaki (Mar. 2018). "Synthesis of highly conductive PEDOT:PSS and correlation with hierarchical structure." English. In: *Polymer* 140, pp. 33–38.

Jin, Yifei, Ashley Compaan, Tapomoy Bhattacharjee, and Yong Huang (June 2016). "Granular gel support-enabled extrusion of three-dimensional alginate and cellular structures." English. In: *Biofabrication* 8.2, p. 025016.

Kefayati, Sarah, David W Holdsworth, and Tamie L Poepping (Jan. 2014). "Turbulence intensity measurements using particle image velocimetry in diseased carotid artery models: effect of stenosis severity, plaque eccentricity, and ulceration." English. In: *Journal of biomechanics* 47.1, pp. 253–263.

Okuzaki, Hidenori (Oct. 2012). "Hierarchical structure of PEDOT/PSS and applications to transparent electrodes." In: Proceedings of the 19th International Workshop on Active-Matrix Flatpanel Displays and Devices - TFT Technologies and FPD Materials, AM-FPD 2012, pp. 53–56.

Poepping, Tamie L, Richard N Rankin, and David W Holdsworth (July 2010). "Flow patterns in carotid bifurcation models using pulsed doppler ultrasound: Effect of concentric vs. eccentric stenosis on turbulence and recirculation." English. In: *Ultrasound in Medicine and Biology* 36.7, pp. 1125–1134.

Smith, R F, B K Rutt, and D W Holdsworth (Oct. 1999). "Anthropomorphic carotid bifurcation phantom for MRI applications." English. In: *Journal of magnetic resonance imaging : JMRI* 10.4, pp. 533–544.

Sun, Christine (Qin), Dong Zhang, and Larry C Wadsworth (Jan. 1999). "Corona treatment of polyolefin films—A review." In: *Advances in Polymer Technology* 18.2, pp. 171–180.

Taccola, S, F Greco, B Mazzolai, V Mattoli, and E W H Jager (Nov. 2013). "Thin film free-standing PEDOT:PSS/SU8 bilayer microactuators." In: *Journal of Micromechanics and Microengineering* 23.11, p. 117004.

Taccola, Silvia, Francesco Greco, Edoardo Sinibaldi, Alessio Mondini, Barbara Mazzolai, and Virgilio Mattoli (Mar. 2015). "Toward a New Generation of Electrically Controllable Hygromorphic Soft Actuators." In: *Advanced Materials* 27.10, pp. 1668–1675.

Tarabella, Giuseppe, Davide Vurro, Stefano Lai, Pasquale DAngelo, Luca Ascari, and Salvatore Iannotta (2020). "Aerosol jet printing of PEDOT:PSS for large area flexible electronics." In: *Flexible and Printed Electronics* 5.1, p. 014005.

Chapter 5

Direct ink writing of PDMS-CNT 3D transducers

This chapter explores the development and characterization of a PDMS-CNT composite that is compatible with the DIW process outlined in chapter 4. The preparation of the PDMS-CNT composite is discussed. Cast PDMS-CNT specimens were prepared to characterize the electrical conductivity, CNT distribution, and mechanical and piezoresistive properties of the composite. Subsequently, DIW was employed using the PDMS-CNT composite to fabricate 3D structures with complex geometries and overhanging features. Finally, tubular 3D piezoresistive sensors were fabricated and connected to a pneumatic system to measure the resistance change of the sensor for applied air pressures. This work demonstrates the potential applications of 3D PDMS-CNT devices. While not explicitly explored in this work, the development of this fabrication process has the potential for directly printing 3D conductive structures that could be used as electrodes during the electrochemical deposition of conjugated polymers such as PEDOT and PPy.

5.1   Materials and Methods

5.1.1   Chemicals

The PDMS used as the elastomer matrix in the PDMS-CNT composite. Sylgard 184 (Dow) is a 2-part system resin consisting of the resin base (PDMS-A) and curing agent (PDMS-B). Two different types of Carboxyl (COOH) functionalized CNTs were used to prepare the PDMS-CNT composite. The first type had dimensions 10 nm to 20 nm diameter and were 10 μm to 30 μm in length. The second type had diameters from 8 nm to 15 nm and were 10 μm to 50 μm in length. Chloroform (Fisher) was used as received. Finally, a platinum-cylcomethylvinylsiloxane complex (3 % platinum in cylcomethylvinylsiloxanes) (Gelest) was used as a supplemental catalyst to cure the PDMS matrix.

5.1.2   PDMS-CNT composite preparation

Elastomer-based CNT composites have been widely studied for various applications (Diekmann, Omelan, and Giese, 2021; Jeon et al., 2019; Kim et al., 2018; Ramalingame et al., 2018). As discussed in chapter 2 these preparation methods typically consider 4 key factors: CNT dimension, CNT functionalization, dispersing solvent, and dispersal method. In the development of the procedure utilized herein a range of options in each category was investigated where it was found the most critical consideration involves the dispersing solvent and method. Early attempts to prepare the composite employed an ultrasonic bath to disperse the CNTs in combination with various dispersing solvents IPA, acetone, toluene, and tetrahydrofuran. To improve the dispersion of the CNTs, a Q700 probe sonicator (Qsonica) was used to provide more localized sonication energy than the ultrasonic bath. Dispersing the CNTs using the probe sonicator improved the dispersion of the CNTs; however,

the open-loop resistance or resistance values of the resultant composites were significantly higher than expected. The high resistance of the composites suggested that the CNTs are not well dispersed in the final PDMS-CNT composite. The poor dispersion of the CNTs in the final matrix was attributed to a combination of the poor stability of CNTs in the dispersing solvent and the limited solubility of the dispersing solvent in the PDMS matrix (in the case of IPA and Acetone). To address these challenges, chloroform was used as the dispersing solvent due to its ability to form stable CNT dispersion and its solubility in the PDMS resin Liu and Choi (2012). The combination of chloroform and probe sonication enabled the production of stable CNT dispersions in chloroform and PDMS/chloroform solutions.

PDMS-CNT composite with CNT loading of 4 % (w/w), 6 % (w/w) and 8 % (w/w) were prepared according to the following procedure (fig. 5.1). The applicable mass of CNTs was added to 50 mL of chloroform, sonicated for 15 min at 30 % amplitude to disperse the CNTs. A PDMS-A solution was prepared by adding 4.5 g of PDMS-A to 20 mL of chloroform while stirring at 400 rpm. Then the PDMS-A/chloroform solution is added to the CNT-chloroform dispersion and sonicated for 10 min at 35 % amplitude. After sonication, the chloroform is removed from the solution via evaporation by placing the solution in a heated water bath at 70 °C. After 2 h, the beaker is placed directly on a hotplate at 80 °C until 10 % chloroform is remaining. At this stage, PDMS-B is added to the PDMS-A/CNT solution, in a 10:1 ratio of PDMS-A to PDMS-B, including an additional 50 μL of platinum catalyst. The additional catalyst ensured the curing reaction rate was sufficiently increased to limit interaction between the extruded PDMS-CNT resin and the carbomer gel during the DIW process. The composite was then pressed into moulds for casting or forced through a metal mesh with holes 355 μm × 385 μm and then loaded into syringe barrels for DIW extrusion.
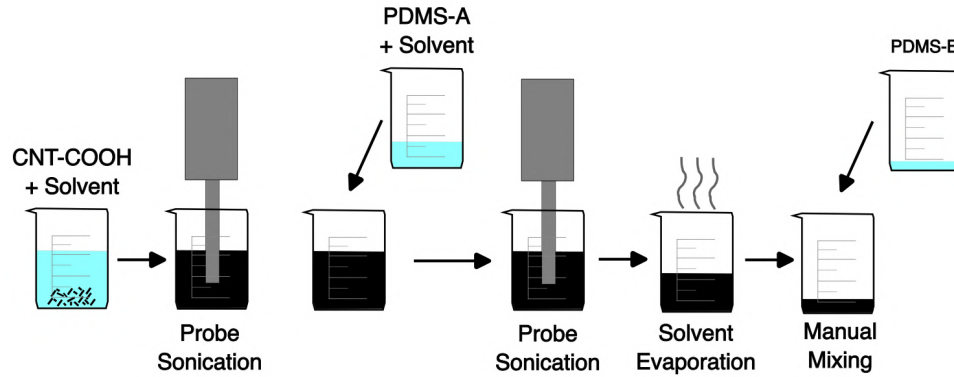
Figure 5.1: The PDMS-CNT composite material is prepared by probe sonication of CNT-COOH in chloroform, while PDMS-A is dissolved in chloroform by magnetic stirring. The PDMS-chloroform solution is then added to the CNT-COOH dispersion, followed by further probe sonication. Finally, chloroform is removed from the material by heating on a hotplate and PDMS-B is manually mixed in to the composite to initiate curing.

5.1.3 Electrical characterization

The electrical conductivity of cast samples was evaluated using a Keithley 2611 source measure unit (SMU) and a custom apparatus to clamp the sample between two glass plates equipped with copper film electrodes. Two-point conductivity measurements were then taken across the length of the sample. Where the two-point conductivity (σ) is given by the equation:

$$\sigma = \frac{I \cdot L}{V \cdot A} \tag{5.1}$$

Where I is the set current, V is the measured potential difference, L is the sample length, and A is the cross-sectional area of the specimens.

5.1.4 Tensile specimen preparation and characterization

Tensile specimens (ASTM D1708) were prepared by scraping the viscous PDMS-CNT paste into a 3D printed mould with 1 mm depth for each concentration. Samples were cured in an oven at 80 °C overnight. Samples were released from the mould

and washed with IPA. Using a universal test stand (ESM303, Mark-10), tensile specimens were then cyclically strained between 4.5 % to 14.5 % strain at a rate of 10 mm · min^{-1} for 100 cycles. The grips of the tensile tester were covered with a layer of polyimide tape to electrically isolate the sample. The copper tape was then applied to both sides of the grips to act as electrodes once clamping the sample. The resistance of samples was measured throughout dynamic testing using the Keithley 2611 SMU and a custom MATLAB script. To analyze the sensitivity of the piezoresistive PDMS-CNT strain sensors the gauge factor (GF) for the prepared sensors was determined by:

$$GF = \frac{\Delta R / R_0}{\epsilon} \tag{5.2}$$

Where ΔR is the change in resistance, R_0 is the initial measured resistance, and ϵ is the applied strain.

5.1.5   Direct ink writing of 3D PDMS-CNT structures

The process employed for DIW of 3D PDMS-CNT structures was based upon that developed in chapter 4. The process parameters were adapted to suit the higher viscosity of the CNT-PDMS composite. All models were printed at 10 mm · s^{-1} with a 600 µm diameter steel nozzle 38 mm in length. A 0.5 % (w/w) carbomer gel was used for all prints.

5.1.6   3D PDMS-CNT sensor testing

3D piezoresistive sensors were fabricated by DIW of single-walled circular tube model with a diameter of 8 mm and length of 25 mm using the 6 % (w/w) CNT-COOH composite formulation. Electrodes were applied to the PDMS-CNT tube by applying 2 strips of silver epoxy along the length of the tube at 180° relative to each other. Copper wires were then embedded in the silver epoxy to provide connection points.

Finally, the silver epoxy was cured at 60 °C for 2 h. The 3D PDMS-CNT sensor was then connected in-line with a closed pneumatic system, using custom-modelled barb adapters, where the Ultimus V (Nordson EFD) was used to apply a range of input pressures and a differential pressure sensor (MPX53DP) provided feedback on the transient pressure signal. The differential pressure signal was amplified using an AD623 instrumentation amplifier, read via an Arduino Nano microcontroller, and logged to a connected PC via serial communication. Two-point resistance was obtained separately using the Keithley 2611 SMU and custom MATLAB script. Pressures from 1 psi to 8 psi were applied in increments of 1 psi to the sensor in 2 s step inputs at 0.2 Hz for 25 cycles.

5.1.7   Microscopy

All optical microscopy images were obtained utilizing the VHX-7000 digital microscope (Keyence). Scanning electron microscopy was conducted using the SU3500 Variable Pressure SEM (Hitachi).

5.2   Results and discussion

5.2.1   Cast PDMS-CNT electrical characterization

Early tests of composite formulations consisting of pristine MWCNTs resulted in open-loop resistance measurements being recorded, this indicated the SMU was not able to accurately measure the conductivity of the samples. Similarly, PDMS-CNT composites with 2 % (w/w) CNT-COOH yielded open-loop resistance measurements. The percolation threshold is expected to fall between 2 % to 4 % based on the transition from open-loop resistance at 2 % to $0.054\,\text{S} \cdot \text{m}^{-1}$ at 4 %. This estimated percolation threshold is higher than that reported in similar works sug-

gesting either a change in measurement equipment is needed to measure higher resistance values or improvements to the dispersion process are required. The electrical conductivity of cast PDMS-CNT composite specimen consisting of CNT-COOH samples is summarized in fig. 5.2 and table 5.1. It can be seen that with increasing CNT-COOH loading fraction the conductivity of the sample increases on the semi-log plot. Conventional percolation theory states that the electrical conductivity of nanocomposite materials can be estimated using a power law model given by (Stauffer and Aharony, 2014):

$$\sigma = \sigma_f(\phi_f - \phi_p)^b \tag{5.3}$$

where σ_f represents the filler conductivity, ϕ_f is the volume fraction of filler, and ϕ_p is the percolation volume fraction and the exponent b is a function of properties of both the conductive filler and matrix material (Zare and Rhee, 2018). While the close agreement with previously reported coefficient values using this model is not expected in this work due to insufficient knowledge of the percolation threshold a general agreement with the trend was demonstrated through curve fitting of a power-law relationship to the experimental data which yielded an R^2 value of 0.860. Disagreement with the model can be attributed to the increased variance seen in conductivity measurements for 8 % (w/w) CNT-COOH. This variance demonstrates the challenges associated with creating CNT dispersions of consistent quality at high-loading fractions due to the preference of CNTs to re-agglomerate during solvent removal (Gupta et al., 2013).

To examine the impact of CNT morphology on the electrical conductivity, CNT-COOH of higher aspect ratio with dimensions 8 nm to 15 nm diameter and 10 µm to 50 µm length were used to fabricate 6 % (w/w) PDMS-CNT cast specimen. The average conductivity of these samples was found to be $0.305 \cdot 10^{-1}\,\mathrm{S \cdot m^{-1}}$ which
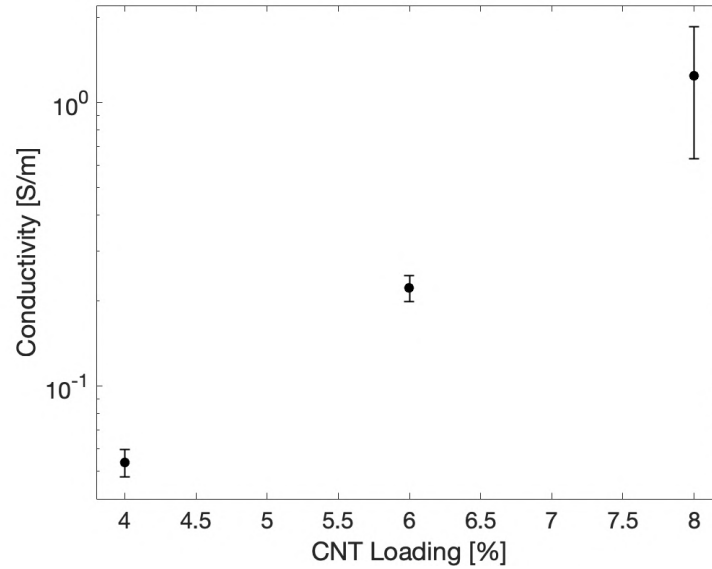
Figure 5.2: Conductivity values for cast ASTM D1708 tensile specimen of PDMS-CNT with varying CNT-COOH loading fraction shows an increase in conductivity with CNT loading fraction.

CNT-COOH Loading	Electrical Conductivity ±SE (S/m)
2 % (w/w)	No percolation
4 % (w/w)	$(5.30 \pm 0.60) \cdot 10^{-2}$
6 % (w/w)	$(2.20 \pm 0.23) \cdot 10^{-1}$
8 % (w/w)	1.24 ± 0.61

Table 5.1: Summary of electrical conductivity for cast PDMS-CNT-COOH composite tensile specimen.

is comparable to that of the originally employed CNT-COOH. While the higher aspect ratio CNTs theoretically reduce the percolation threshold as well as decrease the average CNT-CNT distance in the composite. Improvements to the electrical conductivity were not observed experimentally potentially due to destruction during sonication reducing the CNT length or the preference to reagglomerate of the higher aspect ratio CNTs (Li et al., 2007; Rijk and Lang, 2021).

The cross-section of a cast PDMS-CNT sample with 6 % (w/w) CNT-COOH was imaged via SEM to examine to the quality of the CNT dispersion in the composite (fig. 5.3). Figure 5.3(a) shows that while some agglomerations are visible, the dispersion is relatively uniform thus confirming the developed material fabrication procedure is suitable. Figure 5.3(b) provides a higher magnification view of a region containing an agglomeration of CNTs with an approximate diameter of 20 μm. Additionally at higher magnifications the physical dimensions of individual CNTs can be investigated. Given the high density of CNTs it is difficult to ascertain exact dimensions of individual CNTs, however, there are visible fragments with lengths below the reported lengths of the supplied CNT-COOH of 10 μm suggesting damage during the sonication process. Physical destruction of CNTs can occur during the dispersion process by sonication at higher amplitude, resulting in reduced aspect ratio and a commensurate loss in electrical conductivity which may be contributing to the higher observed percolation threshold for the CNT-PDMS composite (Arrigo et al., 2018; Wu et al., 2019).

5.2.2   PDMS-CNT composite mechanical testing

Prior to the development of 3D transducers from the PDMS-CNT composite tensile samples (ASTM D1708) were cast in custom dogbone moulds to characterize the performance of planar specimens. Tensile specimens dynamic testing was initiated at 0 % strain up to 14.5 % strain but was only relaxed to 4.5 % strain, and subsequent
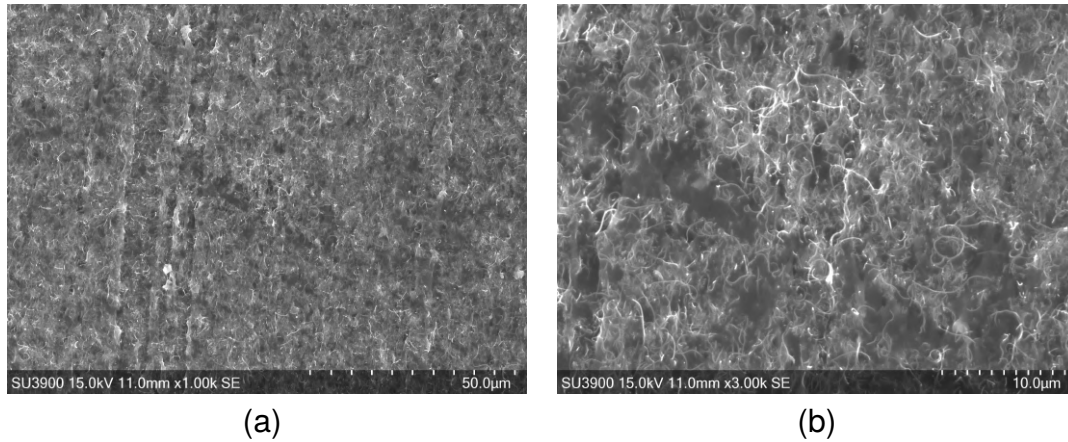
Figure 5.3: SEM images of a the cross section of cast specimen containing 6 % (w/w) CNT-COOH at (a) 1000× and (b) 3000× magnification show some regions of CNT agglomerates with higher magnification revealing individual CNTs.

cycles occurred between 4.5 % to 14.5 % strain. The stress-strain plot for the first cycle is shown in fig. 5.4, and demonstrates both the increased stiffness of the material with increased CNT-COOH loading fraction as well as the hysteresis effect commonly observed in elastomers (Sanli and Kanoun, 2020). Due to the non-linearity observed in approximately the first 2 % strain, the Young's modulus was measured between 5 % to 14.5 %. The Young's moduli were found to be 2.70 MPa, 3.44 MPa and 4.15 MPa for 4 %, 6 % and 8 % CNT-COOH respectively, with all linear regression R^2 values being greater than 0.997. Tensile testing was also conducted on pristine Sylgard 184 resulting in a Young's modulus of 1.58 MPa and a linear relationship is observed between Young's modulus and CNT-COOH loading fraction demonstrating a significant stiffening effect of the CNT-COOH in the composite.

The piezoresistive properties of the PDMS-CNT composite was examined by dynamic cyclic testing, and the resistance response throughout the 100 strain cycles is shown in fig. 5.5. Prior to initiating the test stand motion, the resistance was recorded for 300 s to ensure the sample resistance a steady measurement was achieved. In the initial cycles there is a distinct exponential decay that is more
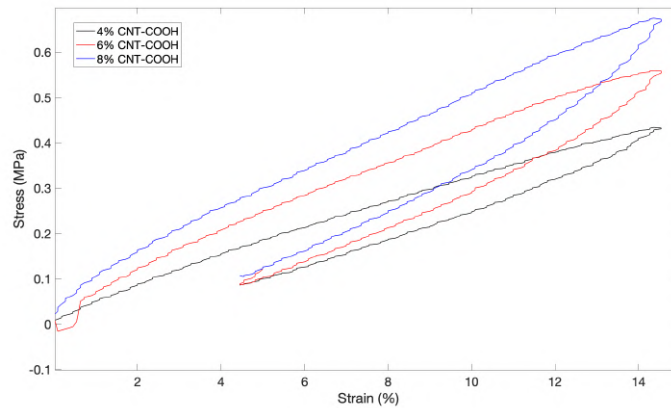
Figure 5.4: The mechanical data for the initial extension and relaxation cycle of dynamic piezoresistive testing is shown for cast PDMS-CNT tensile specimen at each CNT-COOH loading fraction, a distinct hysteresis effect is observed in all samples as well as an increased Young's modulus with CNT-COOH loading fraction.

dramatic for the 4 % sample. This decay could be attributed to the tunnelling effect between adjacent CNTs where the lower concentration formulations have a larger distance between adjacent CNTs amplifying the tunnelling effect (Bosque et al., 2022; Simmons, 1963). Another factor contributing to the exponential resistance decay can be attributed to the viscoelasticity of the PDMS elastomer. Examination of the stress-softening behaviour during the initial 10 cycles indicated that a reduction in stress is occurring due to the mechanical Mullins effect (Mullins, 1948). However, during the initial 10 cycles for the 8 % (w/w) PDMS-CNT specimen a 7.6 % reduction in stress at the peak strain is accompanied by a 30.6 % reduction in electrical resistance at the same strain. The disparity in these changes suggests while the mechanical Mullins effect is playing a role in the electrical response the interaction between adjacent fill particles also has a significant role. Further investigation is required to identify the role of the mechanical Mullins effect on the percolation network. This future work should investigate the effect of strain amplitude, strain rate, and filler concentration to elucidate the role of the polymer matrix viscoelasticity on the percolation network (Beutier et al., 2022).

Further examination of the cycle testing is shown in fig. 5.6 where the normalized resistance response over time for the first 10 and last 10 cycles for each CNT-COOH loading fraction is shown along with the applied strain signal. Normalizing the resistance measurement to the initial resistance recorded for each samples allowed for more direct comparison in the relative performance for each formulation. The first observation to note is the improved stability in resistance measurement as the CNT-COOH loading fraction is increased, this can be attributed to the higher concentration of conductive filler having more reliable conduction pathways that are less impacted by deformation of the PDMS matrix. Through comparison of the first and last 10 cycles for each loading fraction it can be seen that in each case the exponential decay present in the early cycles has been significantly reduced by the last 10 cycles suggesting a steady state has been achieved and underlying phenomena occurring during extension and relaxation can be isolated. Examination of a single cycle, shown in fig. 5.6(f), starting at peak extension and moving towards the relaxed state there is the expected decrease in resistance as the spacing between adjacent CNTs decreases. However, at a point during the relaxation period there is an observed increase in resistance which peaks at the most relaxed state and is followed by a decrease in resistance in the early stage extension, as the sample is stretched further an increase in resistance is again observed as expected. The result of this response is an observed peak in resistance at the maximum tensile strain point with a secondary resistance peak of a lower value at the minimum tensile strain point (fig. 5.7. This secondary resistance peak is observed in all samples, independent of CNT-COOH loading fraction, and is more pronounced at lower filler concentrations. A proposed explanation for this phenomenon is the combination of Poisson's ratio and the impact of anisotropy of the CNTs. A typical Poisson's ratio for PDMS will be in the range of 0.45 to 0.5 meaning the applied longitudinal strain will result in a lateral strain, whereby the CNT-CNT distance will decrease

in the direction perpendicular to the applied tensile strain (Johnston et al., 2014). This out-of-plane compression may be causing an initial decrease in the measured resistance until the longitudinal strain increases to a point where the in-plane tensile strain becomes the dominant factor in determining the electrical response of the material and the associated increase in resistance with tensile strain is observed. The secondary resistance peak has previously been observed in nanocomposites composed of graphene nanoplatelets where the 2D nature of the filler creates increased tunnelling area in preferential directions, while this effect is not observed in piezoresistive sensors composed of carbon black nanoparticles (Bosque et al., 2022; Hu et al., 2021). Given the 1D geometry of CNTs the anisotropy of the filler may play less of a role in the electrical response but based on the observations seen here there appears to be a significant effect. Additionally, disorder effects of the polymer chains on the mobility of the percolation network may also be contributing to this unexpected response and requires further investigation (Beutier et al., 2022).

Due to the nonlinear response observed during cyclic testing the stability of the sensor GF could not be analyzed as was intended. However, examining the initial extension of the CNT-COOH 4 % (w/w) and 8 % (w/w) sensors showed highly linear response and yielded GFs of 8.29 and 4.58 with linear regression R^2 values of 0.997 and 0.988 over 14 % strain. This decrease in GF at higher loading factor is expected, as closer to the percolation threshold there becomes reduced probability for conductive pathways and a higher sensor sensitivity.

5.2.3   DIW of 3D PDMS-CNT structures

Following characterization of the cast, planar specimen, 3D structures were fabricated using the DIW process developed in chapter 4. During the development of the preparation procedure for the PDMS-CNT composite initially all of the chloroform solvent was removed. This solvent-free formulation resulted in a high viscosity paste
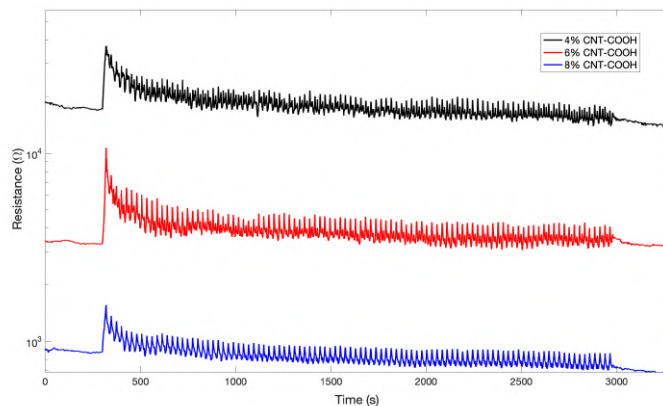
Figure 5.5: Resistance response plots over time for cast PDMS-CNT specimen undergoing 10 % strain cycling for 100 cycles demonstrate a exponential decay in each sample with the higher conductivity loading fractions being less effected.

that proved difficult to extrude due to both the high viscosity of the material as well as the formation of reagglomerations, these factors contributed to regular clogging of the nozzle and the inability to fully complete printed models. To overcome these obstacles, approximately 10 % (w/w) of solvent was allowed to remain in the formulation to reduce the viscosity and prevent reagglomeration of the CNTs. Additionally, following solvent removal the PDMS-CNT paste was manually pressed through a metal mesh to remove any reagglomerated particles that may have formed during solvent evaporation, and further reduce the likelihood of nozzle clogging during extrusion. The residual solvent in the PDMS-CNT paste did not introduce any issues during normal casting of specimen however, when the PDMS-CNT paste was extruded into the carbomer gel, curing times were either longer than anticipated or inhibited altogether. This inhibition was not observed in cases without additional solvent so it is possible that the chloroform provided increased mobility of the curing agent resulting in its dissolution out of the PDMS-CNT formulation and into the carbomer gel. To overcome this issue, additional Ashby-Karstedt catalyst was added to the Slygard 184 formulation to reduce the curing time and limit the potential for interaction with the carbomer gel. Following the addition of this supplementary catalyst
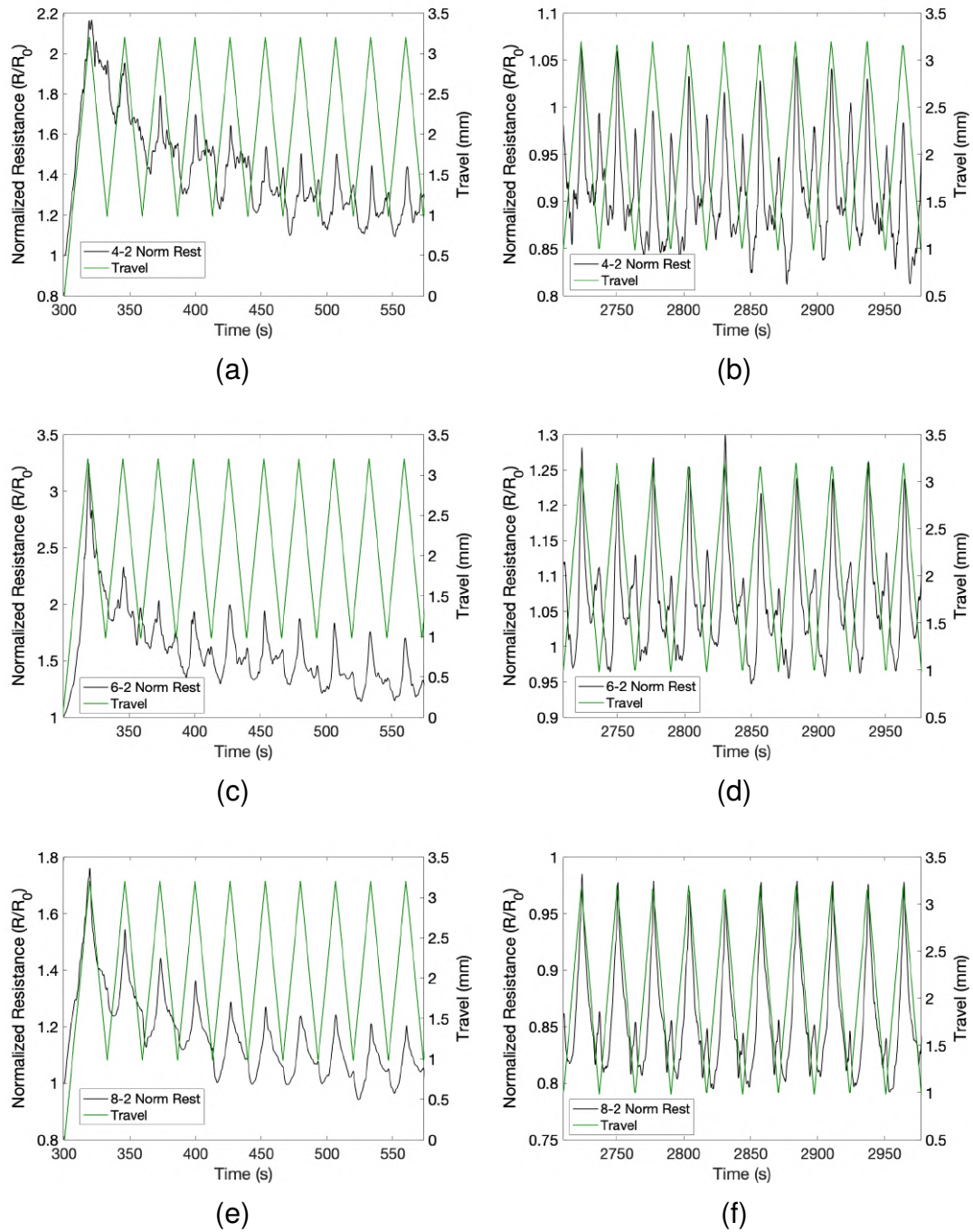
Figure 5.6:   Normalized resistance plots for cast CNT-PDMS tensile specimen with 4 % (w/w), 6 % (w/w) and 8 % (w/w) CNT-COOH during the first 10 cycles (a,c,e), and last 10 cycles show more stable resistance response in last 10 cycles of 100 cycles.
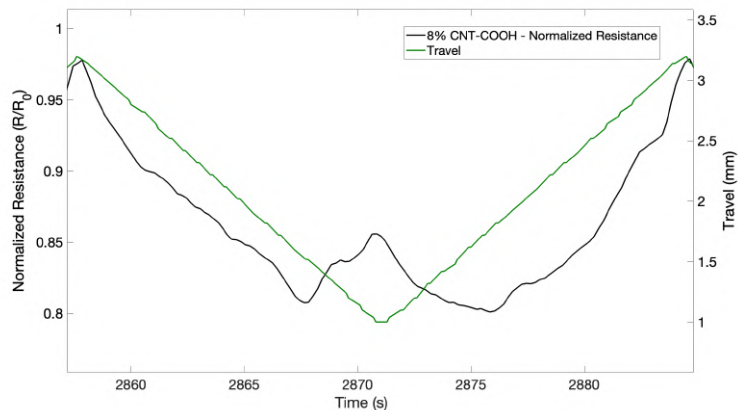
Figure 5.7: The normalized resistance response for a single relaxation and extension cycle for a cast PDMS-CNT tensile specimen with 8 % (w/w) CNT-COOH shows a secondary resistance peak the minimum extension point, this phenomenon is observed in specimen at each CNT-COOH loading fraction which is potentially introduced by the anisotropic nature of CNTs.

no further curing-related issues were observed.

In development of the process parameters of the DIW process for the CNT-PDMS composite a single extrusion spiral model was fabricated to examine the cross-section of a single extrusion which yielded a z-dimension of approximately 600 μm at 65 psi extrusion pressure and $10 \, \text{mm} \cdot \text{s}^{-1}$ print speed. This informed future GCODE files to be produced using a layer thickness of 350 μm allowing for sufficient overlapping between adjacent layers, while the degree of overlapping can be adjusted by increasing and decreasing the extrusion pressure. Empirical results demonstrated that for a layer thickness of 350 μm extrusion pressures in the range of 70 psi to 75 psi provided sufficient layer adhesion to provide a solid wall, free of major defects. This is demonstrated in fig. 5.8(a), where a 8 mm × 25 mm single-walled tube was successfully fabricated using the 6 % PDMS-CNT composite formulation. Figure 5.8(b) provides a higher magnification view of the layer effects as a result of the additive DIW process. The observed average layer thickness of the sample shown in fig. 5.8(b) was determined by image processing to be $(348.7 \pm 4.4) \, \mu\text{m}$ ($n = 12$). Given the uniform average layer thickness, and suitable surface quality for

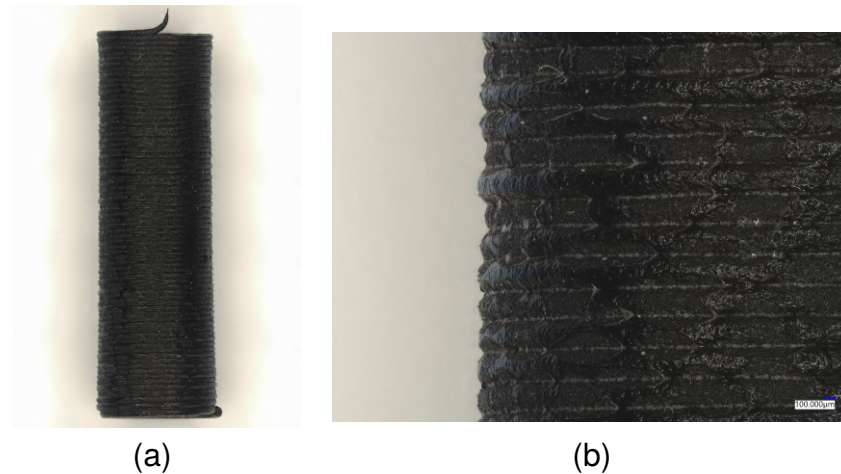<div align="center">(a)   (b)</div>

Figure 5.8: Optical images show the ability of the DIW system to produce a 8 mm × 25 mm single-walled circular tube using the 6 % (w/w) CNT-COOH PDMS composite formulation free of major wall failures (a) and with visible layer effects expected for additive manufacturing processes (b).

the modelled parameters, the DIW process for PDMS-CNT was determined to be sufficiently refined to prepare models consisting of more complex features.

Following successful recreation of a straight tube without any overhanging features the constricted tube and simplified bifurcated artery models developed in chapter 4 were fabricated. Figure 5.9 shows the progression of the model from a 3D representation of the toolpath (a), to the printed structure suspended in the carbomer gel (b), and finally the constricted tube structure following removal from the gel under optical microscopy (c and d). This structure demonstrates the ability to produced true overhanging features that would not be possible without the support gel to maintain the extruded position of the PDMS-CNT composite. Dimensions of the constricted tube as-modelled is 20 mm in height with a larger opening of 15 mm constricting down to 7.5 mm, fig. 5.9(c) shows the print fidelity is consistent with the modelled geometries where a slight reduction in printed part could be attributed to the evaporation of solvent after extrusion. This shrinkage could be accounted for in the 3D modelling process in future studies. Figure 5.10(a), shows the fabrication of
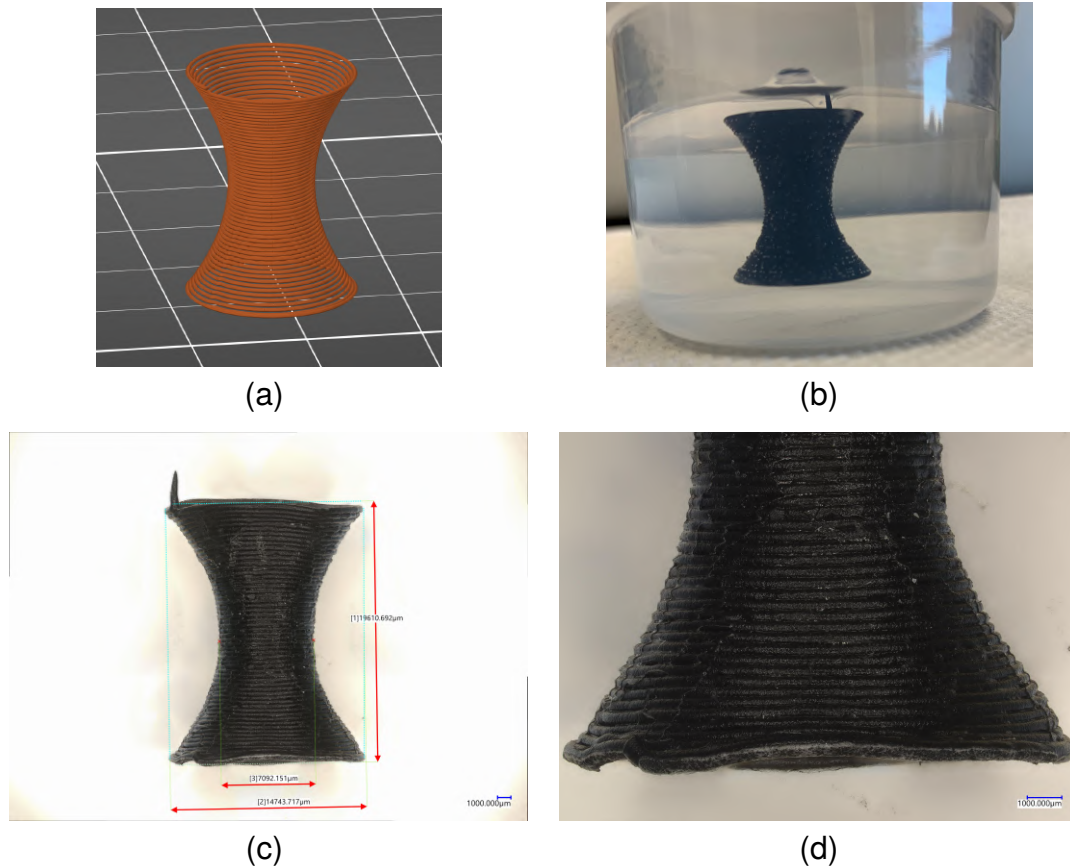
Figure 5.9: Optical images show the ability of the DIW system to produce 3D overhanging features using 6 % (w/w) CNT-COOH, PDMS-CNT composite demonstrated by the constricted tube model (a), suspended in carbomer gel following extrusion (b), and following removal from carbomer demonstrating successful recreation of the modelled structure (c,d).

a simplified bifurcated artery structure from 3D model. The purpose of this model is to demonstrate that more complex vascular networks are still achievable with the PDMS-CNT material (fig. 5.10(b,c,d). This presents the opportunity to create active regions in simulated arterial networks providing feedback as a sensor or controlling flow as a part of a bilayer actuator.

To examine the impact of the DIW fabrication process on the CNT network a section of a 10 mm × 20 mm straight tube model was imaged via SEM. Figure 5.11(a) shows the outer surface of a the tube wall where the distinct layers are visible as well
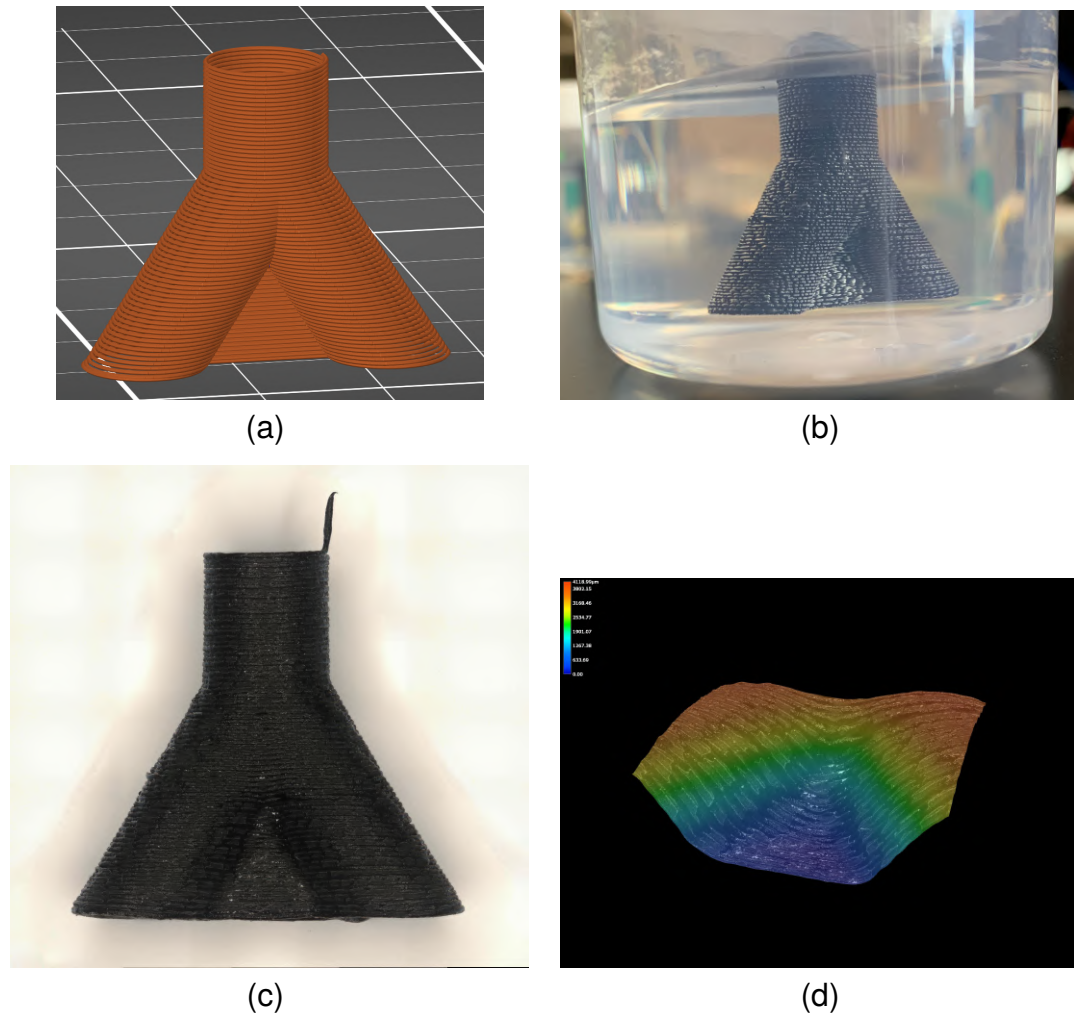
(a)

(b)

(c)

(d)

Figure 5.10: Optical images show the ability of the DIW system to produce 3D arterial structures using 6 % (w/w) CNT-COOH, PDMS-CNT composite demonstrated by the simplified bifurcated artery model (a), suspended in carbomer gel following extrusion (b), following removal from carbomer demonstrating successful recreation of the modelled structure (c), and 3D topographical plot to visualize the curvature of the structure (d).

as areas on the surface where foamed morphologies are observed. These foamed regions are not seen on the surface of cast samples suggesting that this effect is likely due to residual carbomer adhered to the PDMS-CNT surface indicating further time is required in the washing solution (Piau, 2007). The cross-section of the tube model is shown in fig. 5.11(c),(d), and (e), from these images it can be seen that even without the ability to fully degas the high-viscosity PDMS-CNT paste a generally solid cross-section with only minor voids has been produced. While some agglomerations appear to show an alignment parallel to the printing direction in fig. 5.11(d), higher magnifications reveal a more disordered CNT network. While some alignment of the CNTs is possible due to the shear rates experienced during extrusion through the steel nozzle, the CNT distribution appears to be comparable to the cast specimen and further rheological investigation is required to determine potential for CNT alignment in future work (Goh, Ismail, and Ng, 2014).

5.2.4   3D piezoresistive pressure sensor

After examination of the capabilities of the DIW system to produce suitable PDMS-CNT structures the application of these structures as 3D piezoresistive sensors was explored. The sensor examined herein is a 8 mm × 25 mm straight tube composed of PDMS-CNT composite with 6 % (w/w) CNT-COOH, including two strips of silver epoxy along the length of the tube acting as electrodes (fig. 5.12). The electrode configuration was chosen as such to simplify the system in only examining hoop stress in the sensor but future tests could employ a multi-channel electrode configuration to better elucidate the piezoresistive performance of the sensor. The sensor was connected to the testing apparatus and air pressures of 1 psi to 8 psi were applied in 1 psi increments. Initial resistance of the sensor was measured to be 830 Ω and applied pressures of 1 psi to 3 psi did not result in a detectable change in resistance of the sensor. However, in the range of 4 psi to 8 psi a piezoresistive
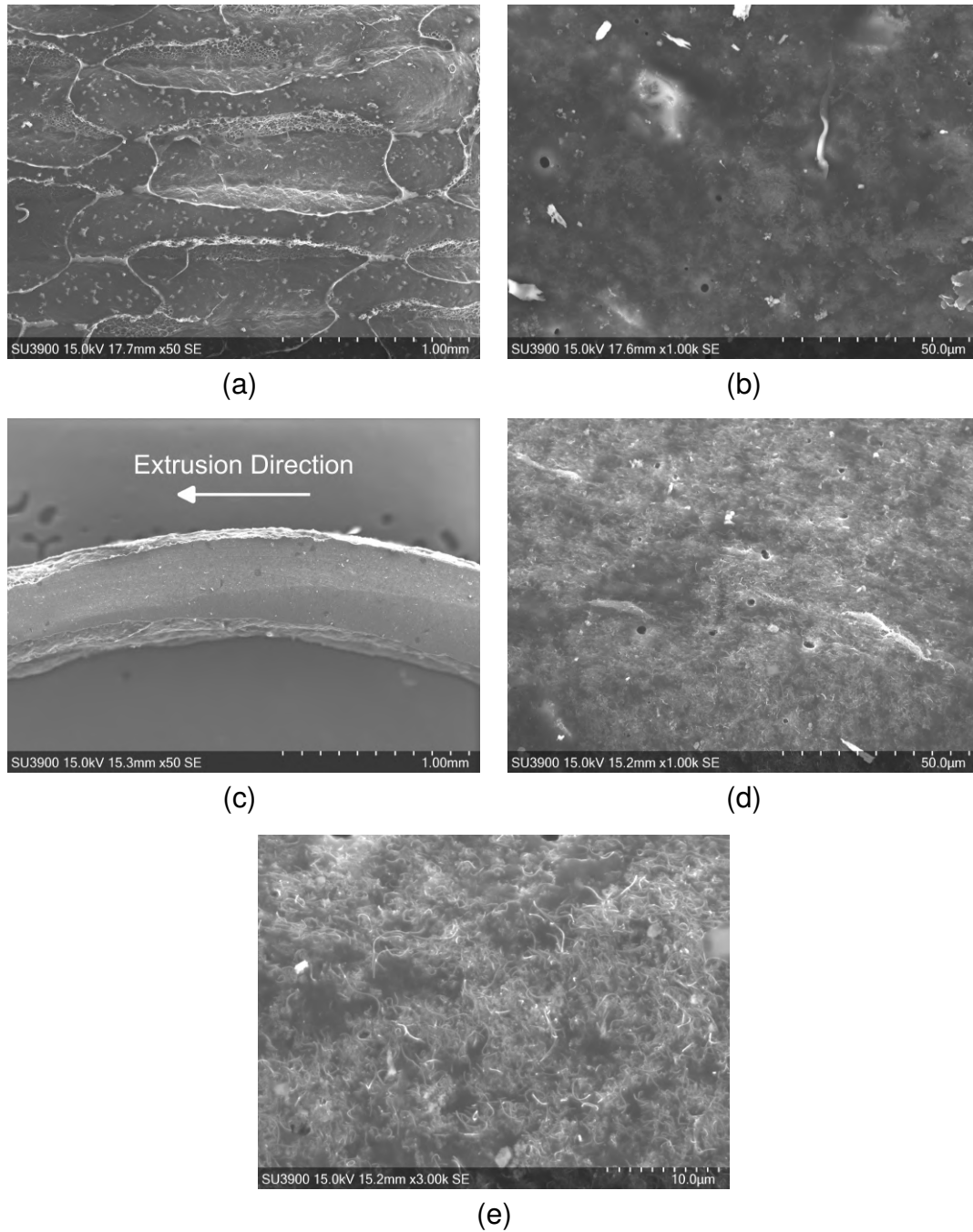
Figure 5.11: SEM images show the surface morphology of the 3D PDMS-CNT tube structures at (a) 50× display residual carbomer adhered to the surface and (b) 1000× show occasional hole defects and agglomerations. Images of the cross-section (c), show possible alignment of carbon nanotube agglomerations parallel to the extrusion direction (d), combined with regions of well-dispersed carbon nanotubes (e).
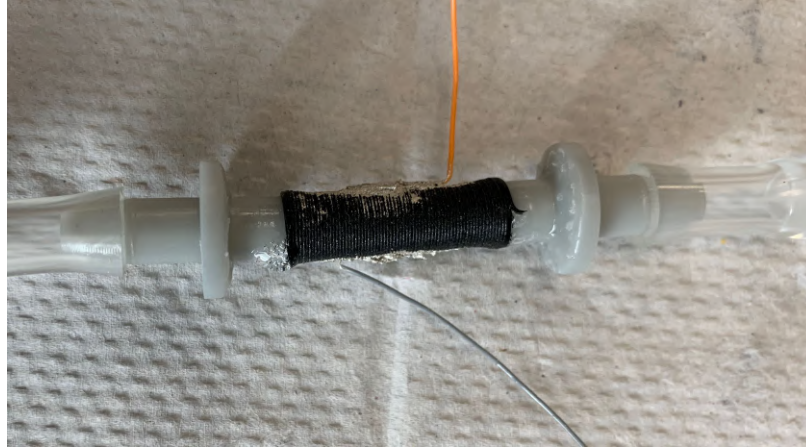
Figure 5.12: A DIW 3D PDMS-CNT straight tube piezoresistive sensor is connected in-line with a pneumatic system and equipped with silver epoxy electrodes to provide the resistance response to applied air pressure inputs.

response was detected. Figure 5.13(a) shows the resistance response over time as various pressures are applied for 25 cycles. Stable device performance is observed throughout the test at each pressure with consistent change in resistance for each successive applied pressure. However, fig. 5.13(b) shows the first cycle at each applied pressure and it can be seen that the initial resistance increases with each pressure. This increase in initial resistance may be attributed to the breakdown of contact between the silver epoxy electrode and the PDMS-CNT surface. Examining the normalized resistance of the first cycle at each pressure in fig. 5.13(c) an increase in normalized change in resistance is observed, where the initial resistance is taken as the resistance at the start of each pressure test, until the 7 psi test where the normalized resistance between 7 psi and 8 psi is not significant. Further development of the electrode attachment process is required to ensure a conformal contact is achieved and that a higher density of electrodes can be deposited to fully define the piezoresistive response. However, this initial investigation demonstrate the ability to fabricate 3D PDMS-CNT composite sensors that have the potential to be used as pressure sensors in pneumatic systems.
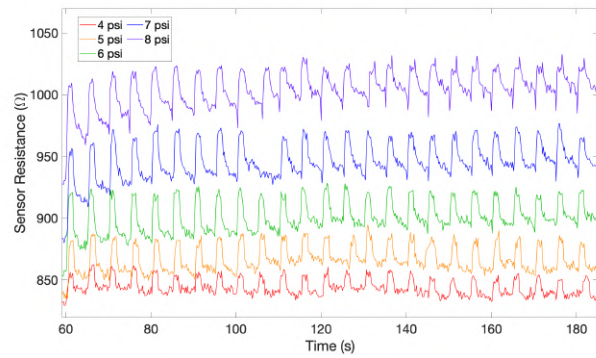
(a)
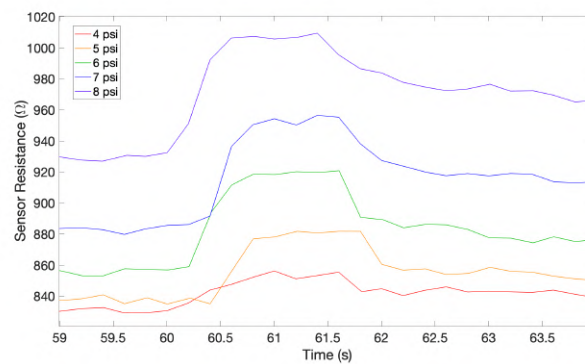
(b)
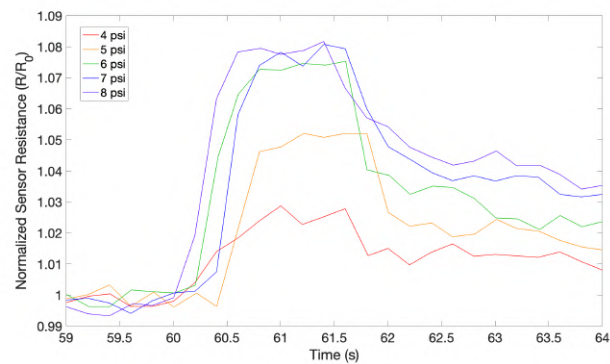
(c)

Figure 5.13: The resistance response of a 3D PDMS-CNT tube piezoresistive sensor to the application of step input air pressures of 4 psi to 8 psi for 2 s at 0.2 Hz over 25 cycles shows the stability of the response at each pressure (a). Closer analysis of the sensor resistance response for the first cycle shows the variation in initial resistance at each pressure (b). The normalized sensor resistance response accounts for variations in the initial sensor resistance and shows the sensor saturation above 6 psi (c).

5.3 Chapter summary

This chapter outlined the development of a PDMS-CNT nanocomposite for the application of DIW 3D piezoresistive tubular sensors. A preparation process was developed based upon CNT functionalization, geometry, and concentration to enable casting of conductive 2D films with a percolated CNT-COOH network. The electrical, mechanical, and piezoresistive proprieties of cast samples were examined. Challenges with creating uniform dispersions of CNTs at relatively high concentration were discovered and exhibited by variance in electrical conductivity at 8 % (w/w) CNT-COOH. Dynamic cycling of the PDMS-CNT tensile specimen exhibited GFs in an expected range for CNT-based piezoresistive sensors, however, nonlinear effects were observed, likely due to the anisotropy of the CNT filler. Following characterization of cast 2D specimen the PDMS-CNT formulation was integrated into the DIW fabrication process where the carbomer gel fully supported the extruded material enabling the fabrication of 3D structures exhibiting overhanging features and increased complexity. These 3D structures were then examined for the potential application of piezoresistive air pressure sensors in a pneumatic system, where the electrical response indicated a minimum detectable pressure of 3 psi and a detectable resistance response up to 8 psi. These initial results provide confidence that further development of the 3D sensor fabrication process can provide built-in sensor networks to complex fluid-carrying networks and as flexible 3D electrodes for the deposition of CP to further develop 3D EAP devices.

5.4   References

Arrigo, Rossella, Rosalia Teresi, Cristian Gambarotti, Filippo Parisi, Giuseppe Lazzara, and Nadka Tzankova Dintcheva (2018). "Sonication-Induced Modification of Carbon Nanotubes: Effect on the Rheological and Thermo-Oxidative Behaviour of Polymer-Based Nanocomposites." In: *Materials* 11.3, p. 383.

Beutier, Clémentine, Laurent David, Guillaume Sudre, Philippe Cassagnau, Patrick Heuillet, Bernard Cantaloube, and Anatoli Serghei (2022). "In-situ coupled mechanical/electrical investigations of EPDM/CB composite materials: The electrical signature of the mechanical Mullins effect." In: *Composites Science and Technology* 218, p. 109144.

Bosque, Antonio del, Xoan F. Sánchez-Romate, María Sánchez, and Alejandro Ureña (2022). "Ultrasensitive and highly stretchable sensors for human motion monitoring made of graphene reinforced polydimethylsiloxane: Electromechanical and complex impedance sensing performance." In: *Carbon* 192, pp. 234–248.

Diekmann, Astrid, Marvin C. V. Omelan, and Ulrich Giese (2021). "Influence of Carbon Nanotube-Pretreatment on the Properties of Polydimethylsiloxane/Carbon Nanotube-Nanocomposites." In: *Polymers* 13.9, p. 1355.

Goh, P.S., A.F. Ismail, and B.C. Ng (2014). "Directional alignment of carbon nanotubes in polymer matrices: Contemporary approaches and future advances." In: 56, pp. 103–126.

Gupta, Murari L, Stefanie A Sydlik, Jan M Schnorr, Dong Jin Woo, Sebastian Osswald, Timothy M Swager, and Dharmaraj Raghavan (Mar. 2013). English. In: *Journal of Polymer Science, Part B: Polymer Physics* 51.6, pp. 410–420.

Hu, Meifeng, Yang Gao, Yejia Jiang, Huidan Zeng, Songshan Zeng, Mengting Zhu, Gefan Xu, and Luyi Sun (2021). "High-performance strain sensors based on bilayer carbon black/PDMS hybrids." In: *Advanced Composites and Hybrid Materials* 4.3, pp. 514–520.

Jeon, Dae-Young, Heeju Kim, Min Wook Lee, So Jeong Park, and Gyu-Tae Kim (2019). "Piezo-impedance response of carbon nanotube/polydimethylsiloxane nanocomposites." In: *APL Materials* 7.4, p. 041118.

Johnston, I D, D K McCluskey, C K L Tan, and M C Tracey (2014). "Mechanical characterization of bulk Sylgard 184 for microfluidics and microengineering." In: *Journal of Micromechanics and Microengineering* 24.3, p. 035017.

Kim, Jeong Hun, Ji-Young Hwang, Ha Ryeon Hwang, Han Seop Kim, Joong Hoon Lee, Jae-Won Seo, Ueon Sang Shin, and Sang-Hoon Lee (Jan. 2018). "Simple and cost-effective method of highly conductive and elastic carbon nanotube/ polydimethylsiloxane composite for wearable electronics." In: *Nature Publishing Group*, pp. 1–11.

Li, J., P. C. Ma, W. S. Chow, C. K. To, B. Z. Tang, and J.-K. Kim (2007). "Correlations between Percolation Threshold, Dispersion State, and Aspect Ratio of Carbon Nanotubes." In: *Advanced Functional Materials* 17.16, pp. 3207–3215.

Liu, Chao-Xuan and Jin-Woo Choi (Oct. 2012). "Improved Dispersion of Carbon Nanotubes in Polymers at High Concentrations." In: *Nanomaterials* 2.4, pp. 329–347.

Mullins, L. (1948). "Effect of Stretching on the Properties of Rubber." In: *Rubber Chemistry and Technology* 21.2, pp. 281–300.

Piau, J M (June 2007). "Carbopol gels: Elastoviscoplastic and slippery glasses made of individual swollen sponges. Meso- and macroscopic properties, constitutive equations and scaling laws." English. In: *Journal of Non-Newtonian Fluid Mechanics* 144.1, pp. 1–29.

Ramalingame, Rajarajan, Dhivakar Rajendran, Amoog Lakshmanan, and Olfa Kanoun (Mar. 2018). "Effect of Organic Solvent on MWCNT-PDMS Nanocomposite Based Capacitive Pressure Sensors." In: *2018 15th International Multi-Conference on Systems, Signals & Devices (SSD)*, pp. 1208–1211.

Rijk, Tim Mike de and Walter Lang (2021). "Low-Cost and Highly Sensitive Pressure Sensor with Mold-Printed Multi-Walled Carbon Nanotubes Dispersed in Polydimethylsiloxane." In: *Sensors* 21.15, p. 5069.

Sanli, Abdulkadir and Olfa Kanoun (Mar. 2020). "Electrical impedance analysis of carbon nanotube/epoxy nanocomposite-based piezoresistive strain sensors under uniaxial cyclic static tensile loading." In: *Journal of Composite Materials* 54.6, pp. 845–855.

Simmons, John G (1963). "Generalized Formula for the Electric Tunnel Effect between Similar Electrodes Separated by a Thin Insulating Film." In: *Journal of Applied Physics* 34.6, pp. 1793–1803.

Stauffer, Dietrich and Ammon Aharony (2014). *Introduction to percolation theory: revised*. CRC Press.

Wu, Di, Mengni Wei, Rong Li, Tao Xiao, Shen Gong, Zhu Xiao, Zhenghong Zhu, and Zhou Li (2019). "A percolation network model to predict the electrical property of flexible CNT/PDMS composite films fabricated by spin coating technique." In: *Composites Part B: Engineering* 174, p. 107034.

Zare, Yasser and Kyong Yop Rhee (Dec. 2018). "A power model to predict the electrical conductivity of CNT reinforced nanocomposites by considering interphase, networks and tunneling condition." In: *Composites Part B: Engineering* 155, pp. 11–18.

Chapter 6

Vat polymerization of 3D PPy-BEMA-PEGMA transducers

This chapter investigates modifications to the PPy-BEMA-PEGMA resin to improve the electrical conductivity and electroactivity loss associated with the necessary introduction of the BEMA-PEGMA copolymers for mechanical stability as discussed in chapter 2. Herein the addition of CNTs as a conductive filler is investigated through a range of structures and functionalizations to achieve a stable dispersion in the resin formulation. This project focuses on the development of PPy functionalized CNTs to improve the CNT dispersion quality and stability. These PPy-CNTs are introduced to the resin formulation and the effects on the electrical and mechanical properties of the material on cast tensile specimen are analyzed. Finally, the suitability of the newly developed PPy-BEMA-PEGMA-CNT formulation for additive manufacturing by vat polymerization is explored through fabrication of the Organic Mechatronics and Smart Materials Laboratory logo.

6.1 Materials and methods

6.1.1 Chemicals

The PPy-based photopolymer formulation developed herein was based upon that described in by Cullen and Price (2019) and further developed in chapter 3. The PPy resin formulation contained the following reagents: Py, distilled prior to use (Fisher), multi-walled carbon nanotubes (MWCNTs) with an outer diameter of 20 nm to 30 nm, and length of 10 μm to 30 μm (MK Nano), silver nitrate (Fisher), diphenyl(2,4,6-trimethylbenzoyl)phosphine oxide (TPO), Tinuvin 477 (BASF), bisphenol A ethoxylate dimethacrylate (BEMA) and poly(ethylene glycol) methyl ether methacrylate (PEGMA) (Sigma Aldrich), were all used as received.

6.1.2 Polypyrrole functionalized CNTs

To improve the stability of carbon nanotubes in the PPy-BEMA-PEGMA formulation various MWCNTs were tested, including pristine, nitrogen doped, carboxyl acid doped CNTs. However, each exhibited a strong tendency to reagglomerate. To overcome this preference of CNTs to agglomerate a PPy coating was chemically adsorbed onto the surface of pristine MWCNTs following the process outlined by C.-X. Liu and Choi (2012). The functionalizataion procedure begins with 0.25 g of Py stirred in 3.2 mL of ethanol and 9.4 mL of 30 % hydrogen peroxide. Following preparation of this solution 0.25 g of MWCNT were added under stirring followed by 2 h of sonication in a bath sonicator. Finally, the solution was centrifuged and washed with deionized water repeatedly until the supernatant had a pH of 7.0. The functionalized PPy-CNT were then dried for at least 24 h to evaporate any remaining water. Characterization of the functionalized PPy-CNTs compared to pristine MWC-NTs by thermogravimetric Analysis (TGA) was conducted from 30 °C to 1000 °C at a

rate of $10\,°C \cdot min^{-1}$ under nitrogen gas flow. Finally, laser Raman spectroscopy (In-Via Reflex, Renishaw) was conducted to identify variations in the graphite bands and identify defects (Das et al., 2014).

6.1.3 Dynamic light scattering

Particle size analysis was conducted using the dynamic light scattering (DLS) function of the ZetaPlus zeta potential analyzer. Dispersions of pristine MWCNTS, and functionalized PPy-CNTs at a concentration of $3\,mg \cdot mL^{-1}$ were prepared in deionized water by sonication in an ultrasonic bath (VWR) for 1 h. Solutions were then diluted and mixed using a vortex mixer to redistribute the particles. Finally, the CNT solutions were analyzed for 5 cycles, 2 min.

6.1.4 Polypyrrole photopolymer formulation

Given the variety of compounds involved in the PPy-BEMA-PEGMA formulation, it was vital to ensure the components were well dispersed; to improve the stability, homogeneity and reactivity of the resin. In order to do so, the preparation of the formulation was divided into the fabrication of two dispersions which were then mixed together. Firstly, a 7:3 weight ratio of BEMA-PEGMA was mixed a vortex mixer, to achieve the desired resin viscosity. BEMA-PEGMA (40 %) was then homogenized with Tinuvin 477 (40 % (w/w)) in a test tube with a homogenizer (Fisher Scientific 150 Homogenizer). For the preparation of the second dispersion, Py (41.1 % (w/w)) was homogenized with silver nitrate in an 8:1 molar ratio to Py, and TPO (5 % (w/w)). In the next step both dispersions were combined, homogenized, and finally ultrasonicated for 10 min to further mix, and degas. In resin formulations containing PPy-CNTs the Py in the above process was replaced by Py solutions dispersed with the desired concentration of CNT-PPy. This dispersion was prepared by ultra-

sonicating concentrations of PPy-CNTs, ranging from $1\,mg \cdot mL^{-1}$ to $9\,mg \cdot mL^{-1}$ for 30 min.

6.1.5   Electrical characterization

Due to the limited working area of the vat polymerization apparatus of $9.6\,mm \times 5.4\,mm$ build plate, standard ASTM D1708 tensile specimen films were cast in custom fabricated PDMS moulds, of 1 mm depth, following the resin preparation method described above and cured under 405 nm LEDs for 20 min. Loading rates of PPy-CNTs in the samples were $0\,mg \cdot mL^{-1}$, $1\,mg \cdot mL^{-1}$, $3\,mg \cdot mL^{-1}$ and $9\,mg \cdot mL^{-1}$. The surface conductivity of the composite samples was measured by four-point probe technique using a Keithley 2611 SMU using 3 locations on 3 samples for each loading rate to obtain the average conductivity and standard error.

6.1.6   Piezoresistive characterization

Cast ASTM D1708 Tensile specimen were subjected to cyclic piezeoresitive characterization. Using an ESM303 universal test stand (Mark-10), samples were cyclically strained between 0 % to 2.3 % strain at $3\,mm \cdot min^{-1}$ for 60 cycles. The test stand jaws were equipped with a layer of polyimide tape for electrical isolation and a layer of copper tape to provide electrical contact to the sample when gripped. The copper tape electrodes were then connected to the SMU and custom Matlab script for capture of the electrical response.

6.1.7   Vat polymerization of polypyrrole composite

Fabrication of 3D PPy composite structures was achieved through the use of a previously developed vat polymerization system, employing a high resolution DLP light engine and free surface polymerization (Cullen and Price, 2019). Once the

resin was prepared, it was poured into a metallic vat and loaded into the vat polymerization system. A replication of the Organic Mechatronics and Smart Materials Laboratory logo and thin film models were produced by this technique using 50 µm layer thickness, and a curing time of 3 s. Additionally, a settling time of 20 s between layers was used to allow time for the free surface of the resin to flow into a flat layer.

6.2 Results and discussion

6.2.1 Polypyrrole functionalized CNTs

Previous attempts to introduce CNTs into the existing resin formulation resulted poor stability of the dispersion and significant reagglomeration of CNTs during the printing or casting processes. To improve the stability of the dispersion while maintaining the structural and electrical enhancements of CNTs the pristine MWCNTs were coated with PPy. This was achieved through immersion and sonication of CNTs with Py in an ethanol and hydrogen peroxide solution (S. Liu et al., 2014). To characterize the success of this chemical process both pristine MWCNTs and the functionalized PPy-CNTs were subjected to TGA. The thermal stability of each specimen is shown in fig. 6.1, where it can be seen that in the temperature range 0 °C to 100 °C both the pristine MWCNTs and PPy-CNTs show similar mass decay, this decay can be attributed to water evaporation which had not been removed from the specimen prior to testing, with an additional small change in mass observed in the PPy-CNT sample between 130 °C to 200 °C attributed to the evaporation of unpolymerized Py monomer (Jakab, Mészáros, and Omastová, 2007). However, in the 200 °C to 330 °C temperature range a greater mass loss is observed in the PPy-CNT specimen likely due to the degradation of PPy. Above 200 °C the PPy-CNT specimen exhibited 3.5 % greater mass loss than the pristine MWCNT specimen
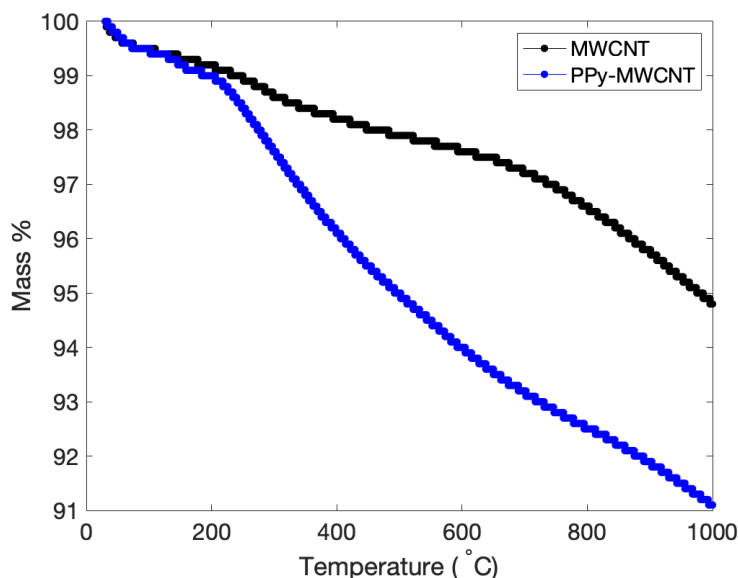
Figure 6.1: Mass loss observed during TGA analysis of pristine multi-walled carbon nanotubes and polypyrrole functionalized multi-walled carbon nanotubes.

which can be attributed either to PPy loss, or contaminants introduced during the treatment process. The TGA results suggest the presence of PPy in the specimen but further analysis by transmission electron microscope is required to ensure it has been adsorbed to the surface of the MWCNT.

Raman spectroscopy was conducted on both PPy-CNT and pristine MWCNT specimen as shown in fig. 6.2. It can be seen that both specimen exhibit the expected pronounced D- and G-band peaks, associated with CNTs, at 1353 and 1583 respectively (Kim et al., 2010). Given the low mass percent of PPy estimated from TGA, the expected Raman peaks associated with PPy are difficult to detect, there may be small peaks present at 637, 930 and 1041 associated with the C-H out of plane vibration, PPy ring in-plane deformations, and the C-H in-plane vibrations respectively (Trchová and Stejskal, 2018; Zhang et al., 2011). However, these peaks are not pronounced, as-such further investigation is required to confirm the composition, and morphology of the functionalized PPy-CNT.
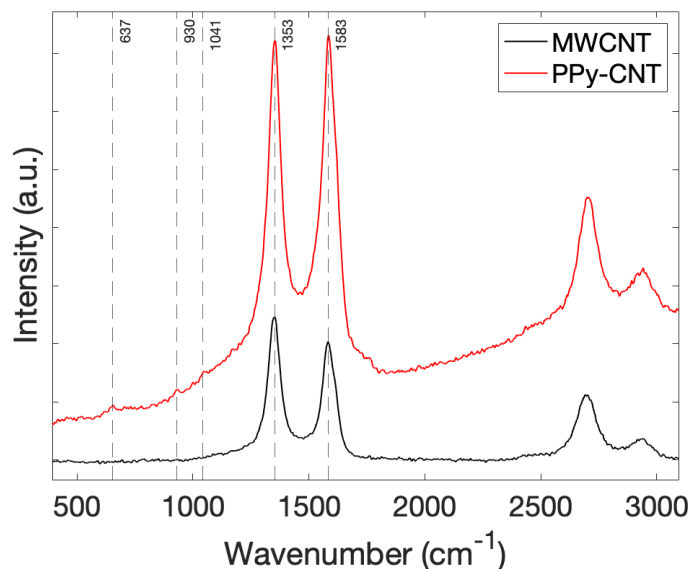
Figure 6.2: Room-temperature Raman spectra of pristine multi-walled carbon nan-
otubes, and polypyrrole functionalized MWCNTs.

6.2.2   Raman spectroscopy

Investigation of TGA and raman spectroscopy provided sufficient indication of the

presence of PPy to proceed with characterization of the dispersion quality of func-

tionalized PPy-CNT. To test the stability of the functionalized PPy-CNT, dispersions

of $3\,mg \cdot mL^{-1}$ pristine MWCNTs, and PPy-CNT, in DI water, were analyzed by

DLS. DLS characterization confirmed substantial improvement in dispersion quality

with particle size effective diameters of $(41.25 \pm 4.33)\,\mu m$ for pristine MWCNT and

$(133.5 \pm 1.6)\,nm$ for the PPy-CNT. Additionally, the dispersion stability was examined

empirically by observing the dispersions 1 h and 24 h after sonication. Figure 6.3(i)

shows that after 1 h the MWCNT dispersion already shows severe reagglomeration

while fig. 6.3(ii), and (v), show that the dispersions of PPy-CNT in DI water remains

stable over 24 h. Finally, fig. 6.3(iii) and (vi), shows a dispersion of $3\,mg \cdot mL^{-1}$ PPy-

CNT in Py, this dispersion appears to remain stable 1 h following sonication, but

visible reagglomeration is observed at 24 h. The smaller mean effective diameter of

particles observed by DLS in combination with the improved stability of dispersions
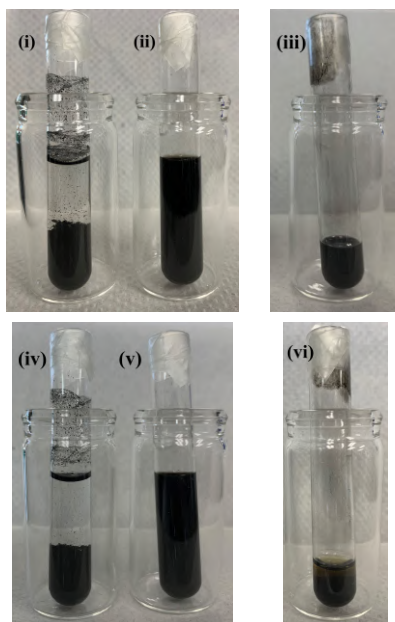
Figure 6.3: dispersions of $3\,mg \cdot mL^{-1}$ carbon nanotubes in water after 1 h following sonication show significant reagglomeration of pristine multi-wall carbon nanotubes (i) when compared with polypyrrole functionalized carbon nanotubes (ii). After 24 h further reagglomeration is seen for the pristine MWCNTs (iv) while the functionalized CNT dispersion remains stable (v). A stable dispersion of polypyrrole functionalized CNTs in pyrrole after 1 h (iii) showed signs of agglomeration after 24 h (vi).

demonstrates that functionalized PPy-CNT are a suitable option to investigate the performance of a PPy-BEMA-PEGMA composite with PPy-CNT additive.

6.2.3   Polypyrrole-BEMA-PEGMA composite

Following successful dispersion of the PPy-CNTs in Py, the conductivity of the resin formulation was investigated by casting samples of PPy-BEMA-PEGMA with $0\,mg \cdot mL^{-1}$, $1\,mg \cdot mL^{-1}$, $3\,mg \cdot mL^{-1}$, $5\,mg \cdot mL^{-1}$ and $9\,mg \cdot mL^{-1}$ of PPy-CNTs dispersed in Py. Given the PPy-BEMA-PEGMA formulation contains 41 % (w/w) Py, the final concentration of PPy-CNTs in the composite formulations are 0 % (w/w), 0.043 % (w/w), 0.129 % (w/w), 0.216 % (w/w) and 0.389 % (w/w) respectively. Figure 6.4 shows a distinct increase in conductivity, even at low loading rates of
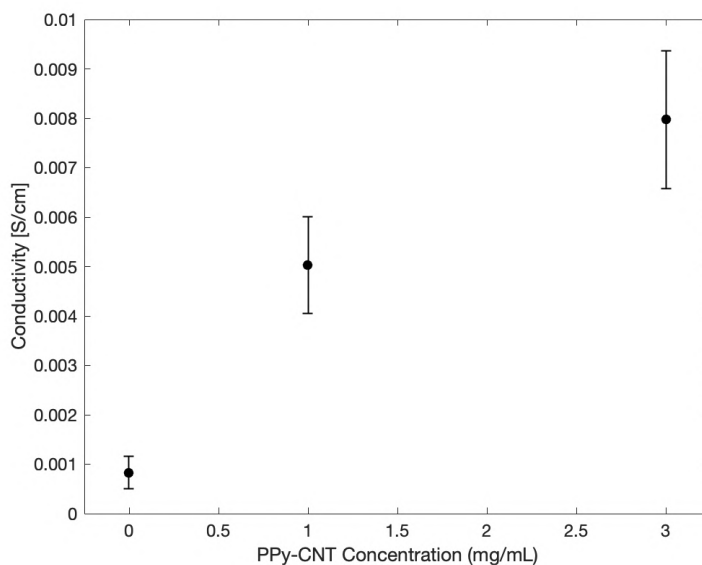
Figure 6.4: 4-point probe conductivity of polypyrrole-BEMA-PEGMA cast films using various loading rates of polypyrrole functionalized carbon nanotubes dispersed in pyrrole.

0.043 % (w/w). The maximum conductivity achieved was at a loading rate of 0.129 % (w/w) PPy-CNTs with $0.007\,97\,\mathrm{S\cdot cm^{-1}}$. A loading rate of 0.389 % (w/w) was also investigated to identify potential limitations at higher loading rates. This formulation still demonstrated sufficient stability as the other dispersions, but due to the high UV absorption of the CNTs the curing of the resin was significantly reduced, which greatly affected the conductivity. Future tests will further investigate the UV absorption of the PPy-CNTs to optimize the conductivity of resin formulations, however, 0.129 % (w/w) was identified as a suitable candidate loading rate for vat polymerization of 3D structures and PPy microstructure feature generation.

6.2.4 Piezoresistive characterization

Following characterization of the surface resistance of the samples, the impact of the addition of CNT-PPy to the composite on the piezoresistive and mechanical properties was evaluated. Dynamic tensile cycling was conducted on samples from

each CNT-PPy loading factor. An interesting observation was made regarding the electrical resistance of the tensile samples when measured by the 2-point method compared to the 4-point method described above. During this experiment it was observed that the measured resistance increased as loading factor of PPy-CNTs in the composite increased. Upon further investigation of the cross sectional areas of the tensile specimen, it was discovered that for PPy-CNT loading factors above 0.043 % (w/w) a hollow cavity was formed due to insufficient UV penetration as a result of the high UV absorbance of the PPy-CNTs (appendix A). This hollow cavity indicated under-curing of the BEMA-PEGMA polymer matrix and likely simultaneously reduced the efficiency of the PPy polymerization reaction. This effect is proposed to be exhibited during the 2-point resistance measurement due to the engagement of the bulk volume of the material in the measurement as opposed to the 4-point probe technique where a small section of the film surface is effected. Further evidence to support the effects of under-curing was obtained through analysis of the mechanical data collected during cyclic testing. This data showed a significant reduction in Young's modulus for samples prepared with 0.129 % (w/w) and 0.216 % (w/w) PPy-CNT dispersions, contrary to the expected stiffening effect of CNTs. A summary of the electrical and mechanical data for the tensile specimen is shown in table 6.1, accounting for the reduced area of samples at higher PPy-CNT loading fraction. It can be seen that in samples where a hollow cavity was found there is a significant effect on both electrical conductivity, and Young's modulus. However, in the 0.043 % (w/w) sample a solid cross-section was fabricated, and there appears to be a less significant impact on the mechanical properties. As a result, the piezoresistive response of this formulation can be compared to the original PPy-BEMA-PEGMA formulation.

The full resistance response to dynamic cycling testing for the 0 % (w/w) and 0.043 % (w/w) PPy-CNT samples are shown in fig. 6.5(a) where the resistance has

PPy-CNT loading	Electrical conductivity (S/cm)	Young's modulus (MPa)
0 % (w/w)	0.857	16.61
0.043 % (w/w)	0.395	15.57
0.129 % (w/w)	0.247	7.57
0.216 % (w/w)	0.046	3.08

Table 6.1: Summary of electrical conductivity and Young's modulus for PPy-BEMA-PEGMA composite cast specimen with various PPy-CNT loading fraction.

been normalized to the resistance measurement at the start of the test as well as to the area of the sample to account for partial under-curing discuss above. Similar to the piezoresistive response of the PDMS-CNT sensors developed in chapter 4 there is an exponential decay in the 0.043 % (w/w) sample likely due to tunnelling effects introduced by the PPy-CNT or stress-relaxation due to viscoelastic effects. Closer examination of the last 10 cycles shown in fig. 6.5(b) demonstrates stable, and linear responses following the expected increase in resistance during extension and returning to a stable value upon relaxation after sensor break-in has occurred. Average GFs for the last 3 cycles were calculated to be 2.66 for the unmodified PPy-BEMA-PEGMA composite and 4.45 for the 0.043 % (w/w) PPy-CNT formulation. The increase in GF can be attributed to the high aspect ratio of the CNTs in the composite whereas the piezoresistivity of the unmodified formulation depends only on the deformation of the silver nanoparticle dispersion and the deformation of the PPy network.

6.2.5   Vat polymerization of polypyrrole composite

While issues during the casting of bulk samples revealed the impact of UV absorption on the under-curing of thick samples this is not anticipated to be an issue in the vat polymerization process, due to the formation of successive thin films. As such, the 0.129 % (w/w) PPy-CNT formulation was identified as a suitable choice for vat
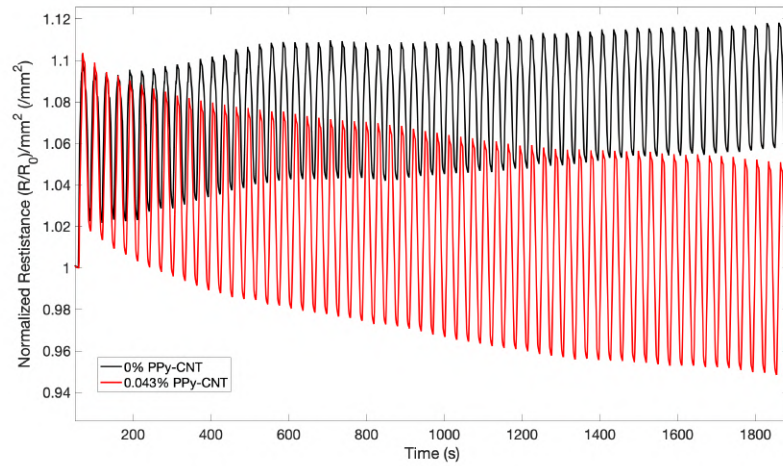
(a)
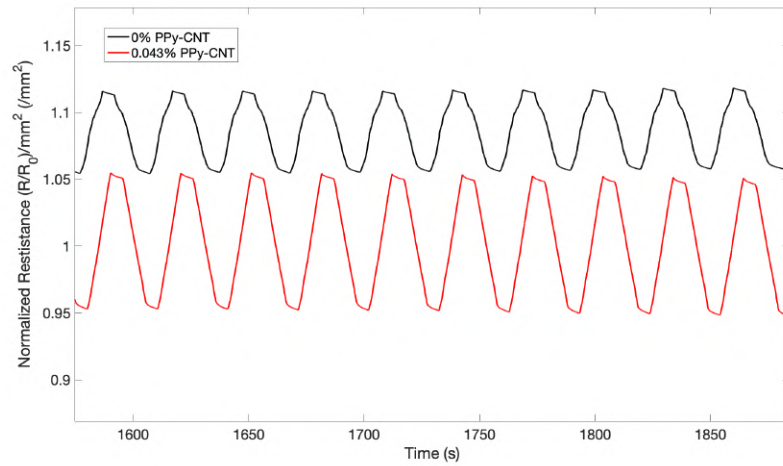
(b)

Figure 6.5: The full-scale (a) and last 10 cycles (b) of the piezoresistive response for cast tensile CNT-PPy-BEMA-PEGMA specimen at 2.3 % strain show a stable, linear response where introduction of polypyrrole functionalized carbon nanotubes at low loading fractions enhances the piezoresistive response.
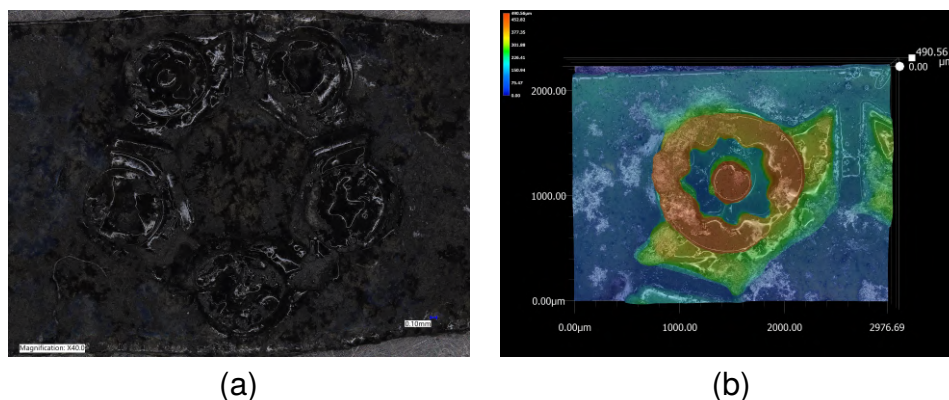
(a)   (b)

Figure 6.6: Optical microscopy images of 3D polypyrrole-BEMA-PEGA-carbon nanotube composite structures fabricated by vat polymerization demonstrating (a) lab logo model and (b) height chart of gear feature demonstrate the preservation of the fabrication system with the new material formulation.

polymerization process due the balance of conductivity and curing rate. Firstly, to demonstrate that the print resolution can be maintained with the PPy-CNT formulation a 3D model of the Organic Mechatronics and Smart Materials Laboratory logo was recreated in fig. 6.6. The logo model is approximately 5 mm × 5 mm and was printed at 50 µm layer thickness and cure time of 3 s per layer. Figure 6.6(a) displays the entirety of the printed logo model by optical microscopy. However, due to the lack of contrast in the sample the detail is difficult to resolve, to overcome this, a topographical plot was generated to highlight the detail in the gear section of the logo (fig. 6.6b). Future studies will aim to leverage the UV absorption characteristics of the PPy-CNT resin with the vat polymerization process settings to improve achievable resolution, while avoiding over-curing of areas surrounding the exposed region.

6.3   Chapter summary

This chapter presented the development of a PPy-BEMA-PEGMA composite resin formulation with improved electrical conductivity through the introduction of PPy fictionalized CNTs. Measurement of the surface conductivity by 4-point probe showed an increasing conductivity with PPy-CNT loading fraction until 0.043 % (w/w), where for higher loading fractions the dispersion quality and UV absorption of the CNTs resulted in reduced conductivity. Further analysis of cast tensile specimen demonstrated reduced conductivity of samples with increasing PPy-CNT loading fraction. This loss in conductivity is associated with the alteration in measurement engaging the bulk of the material, in combination with the under-curing of the thick samples. UV penetration depth issues were not observed for samples fabricated by vat polymerization. This was demonstrated by reproduction of the Organic Mechatronics and Smart Materials Laboratory logo with the 0.043 % (w/w) PPy-CNT, PPy-BEMA-PEGMA-CNT formulation. This resin development achieved the desired objective of improving the electrical conductivity of PPy-BEMA-PEGMA structures to aid in the post hoc deposition of hierarchical PPy features, which will be discussed in chapter 7.

6.4   References

Cullen, Andrew T and Aaron D Price (2019). In: *Smart Materials and Structures* 28.10, p. 104007.

Das, Rasel, Md. Eaqub Ali, Sharifah Bee Abd Hamid, M. S. M. Annuar, and Seeram Ramakrishna (2014). In: *Journal of Nanomaterials* 2014, pp. 1–9.

Jakab, Emma, Erika Mészáros, and Mária Omastová (2007). "Thermal decomposition of polypyrroles." In: *Journal of Thermal Analysis and Calorimetry* 88.2, pp. 515–521.

Kim, Yoong Ahm, Hiroshi Kakegawa, Kazunori Fujisawa, Daisuke Shimamoto, Hiroyuki Muramatsu, Jin Hee Kim, Yong Chae Jung, and Mildred Dresselhaus (2010). "Sensitive G-Band Raman Features for the Electrical Conductivity of Multi-Walled Carbon Nanotubes." In: *Journal of Nanoscience and Nanotechnology* 10.6, pp. 3940–3944.

Liu, Chao-Xuan and Jin-Woo Choi (Oct. 2012). "Improved Dispersion of Carbon Nanotubes in Polymers at High Concentrations." In: *Nanomaterials* 2.4, pp. 329–347.

Liu, Shinian, Cheng Wang, Zengfu Wei, Wangyan Lv, Shengping Fan, Shenglong Zhu, and Fuihui Wang (2014). "One-step surface modification of multi-walled carbon nanotubes by pyrrole." In: *Materials Letters* 134, pp. 91–94.

Trchová, Miroslava and Jaroslav Stejskal (2018). "Resonance Raman Spectroscopy of Conducting Polypyrrole Nanotubes: Disordered Surface versus Ordered Body." In: *The Journal of Physical Chemistry A* 122.48, pp. 9298–9306.

Zhang, Bin, Yiting Xu, Yifang Zheng, Lizong Dai, Mingqiu Zhang, Jin Yang, Yujie Chen, Xudong Chen, and Juying Zhou (2011). "A facile synthesis of polypyrrole/-carbon nanotube composites with ultrathin, uniform and thickness-tunable polypyrrole shells." In: *Nanoscale Research Letters* 6.

Chapter 7

Improved 3D-polypyrrole device performance via hierarchical structures

This chapter outlines the development of a soft-template polymerization process for the post hoc deposition of PPy microstructures on PPy-BEMA-PEGMA composite structures produced by vat polymerization. The aim of this study is to improve the electrochemical performance of the PPy-BEMA-PEGMA formulation where the mechanical stability of the BEMA-PEGMA copolymers has a concomitant loss in electroactivity. The development of the soft-template polymerization method is initiated through the formation of flat and microstructured PPy films on stainless steel electrodes. Following process refinement on flat electrodes of high conductivity the PPy-BEMA-PEGMA formulation is substituted as the electrode for deposition. Deposition of PPy microstructures combines the unique ability to fabricate 3D electroactive structures with the improved electroactive performance of pristine PPy.

7.1 Materials and methods

7.1.1 Chemicals

In the fabrication of polypyrrole microstructures (-)-camphorsulfonic acid (CSA), sodium chloride (NaCl), sodium hydroxide (NaOH), and TRIS-HCl buffer pH 7.5 were used as received (Fisher). Pyrrole 98 % (Sigma Aldrich) was distilled prior to use, $1\,\text{mol} \cdot \text{L}^{-1}$ hydrochloric acid (HCl)(Fisher) was diluted to $0.1\,\text{mol} \cdot \text{L}^{-1}$, and ethanol (Sigma Aldrich) was diluted to 70 %. Additionally, the photopolymer formulation contained pyrrole, silver nitrate (Fisher), 2,4,6-Trimethylbenzoyl-diphenyl-phosphineoxide (TPO), Tinuvin 477 (BASF), BEMA and PEGMA (Sigma Aldrich), used as received.

7.1.2 Polypyrrole microstructure fabrication

Initially, flat PPy films were fabricated by electropolymerization using cyclic voltammetry (CV) in an electrochemical cell containing $0.5\,\text{mol} \cdot \text{L}^{-1}$ CSA, $0.2\,\text{mol} \cdot \text{L}^{-1}$ of Py. The working electrode (WE) and counter electrode (CE) were composed of SAE 304 stainless steel with a Ag/AgCl reference electrode. A custom MATLAB script was used to control the potential. A scan rate of $20\,\text{mV} \cdot \text{s}^{-1}$ was applied for all potential ranges used in this study (Qu, Shi, Chen, et al., 2003; Qu, Shi, Yuan, et al., 2004). The film deposition area was controlled by masking with polyamide tape. Working electrodes were masked to provide an exposed area of 10 mm × 20 mm. To investigate the impact of electrode orientation on the microstructured feature generation both vertical and horizontal electrode configurations were analyzed.

Vertical electrode configuration

The vertical electrode configuration, similar to that used by (Qu and Shi, 2004) had both the WE and CE positioned vertically, spaced approximately 5 mm apart. Initially, a flat film was deposited by applying a potential range from 0 V to 1.2 V for 2 cycles. PPy microstructures were then formed by first producing hydrogen gas bubbles on the surface of the working electrode in a potential range of −0.6 V to −1.2 V. These bubbles were then used as templates for PPy polymerization at 0 V to 1.2 V for either 7 cycles for closed spheres or 2 cycles for open bowl-like structures.

Horizontal electrode configuration

To create the horizontal electrode configuration, straight stainless steel electrodes were bent at 90°, 10 mm from the tip, enabling a horizontal, parallel-plate config-uration each with electrode areas of 10 mm × 20 mm. The electrode spacing was set to 5 mm with the CE placed above the WE for flat film fabrication and the WE above the CE for microstructured feature generation, (fig. 7.1). Similar to the vertical electrode configuration process, flat films were first fabricated by applying 0 V to 1.2 V potential range for 2 cycles. For microstructured PPy fabrication 1 cycle in the potential range 0 V to 1.2 V is applied to first create a flat film, subsequently, a cycle in the −0.6 V to −1.1 V potential range is applied to generate hydrogen bubbles on the WE surface. Finally, one additional cycle between 0 V to 1.2 V is applied to polymerize PPy around the gas bubble templates. Following fabrication, the PPy films are rinsed and stored in DI water to prevent drying and cracking of the thin PPy features.
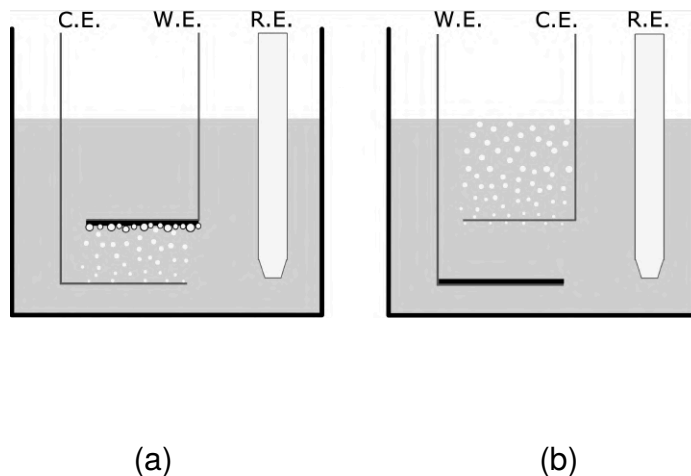
(a)   (b)

Figure 7.1: Schematic diagrams of the horizontal electrode configuration developed for the fabrication of microstructured (a) and flat (b) polypyrrole films by soft-template electropolymerization where the position of working electrode (W.E.) relative to the counter electrode (C.E.) dictates the gas bubble entrapment and control over the morphology of the produced polypyrrole film.

7.1.3   Microstructured 3D printed polypyrrole composite films

Flat and microstructured PPy films were deposited onto PPy composite films fabricated by the vat polymerization process described in chapter 6. Given the novelty of the deposition process, initial tests were conducted on planar films fabricated by vat polymerization. These films were modelled with planar dimensions of 5.4 mm × 9.6 mm and were fabricated by exposure of the PPy-BEMA-PEGMA composite for 3 s with 50 μm layer thickness for 5 layers.

7.1.4   Electrical properties

Electrical properties of flat and microstructures PPy films were analyzed using the four-point probe method to measure the respective sheet resistance of the films by:

$$R_s = \frac{\pi \cdot \Delta V}{\ln 2 \cdot I} \tag{7.1}$$

Where I is the supplied current and ΔV is the associated measured potential difference. The conductivity was measured following removal of the films from the stainless steel electrodes and allowed to dry overnight.

7.1.5   Microscopy

Optical microscopy and feature size measurements were conducted using the VHX-7000 digital microscope (Keyence). Prior to imaging, samples were rinsed with 70 % ethanol to preserve the morphology of the features, and allowed to dry. Feature measurement was conducted on four, $1\,mm^2$ sections using three-point edge selection method to approximate the diameter of microstructure features. SEM images of PPy films polymerized on stainless steel electrodes were obtained on the Hitachi S-3400N microscope. SEM images of PPy films deposited on PPy-BEMA-PEGMA films were obtained on the Hitachi TM4000 desktop SEM.

7.2   Results and discussion

7.2.1   Vertical electrode configuration

The fabrication of microstructured PPy films using the vertical electrode configuration was conducted by applying a negative potential difference between the CE and WE. This negative potential was applied up to −1.1 V to generate hydrogen

gas bubbles on the surface of the WE. Subsequently, the negative potential cycle was repeated to create higher density regions of bubbles as well as stacked bubbles. These bubbles were then used as soft-templates to polymerize PPy around. Closed spherical PPy microstructures were then fabricated in the vertical electrode configuration by cycling in the potential range 0 V to 1.2 V. Figure 7.2 demonstrates the effect of the number of cycles in the positive voltage range on feature morphology. Figure 7.2(a) shows that with 7 polymerization cycles fully enclosed spherical features can be produced, whereas in fig. 7.2(b) only 2 polymerization cycles are applied yielding open bowl-like structures. The work completed by Qu, Shi, Yuan, et al. (2004) showed that a wider potential range from 0 V to 1.4 V resulted in higher aspect ratio tube structures rather than spheres. However, in this work, fig. 7.3 shows that 3 cycles applied in wider potential ranges resulted in a greater variation of open and closed features without a significant change in the height of these features. This effect informed the parameter selection for future tests to maintain a positive potential range of 0 V to 1.2 V for the polymerization of flat PPy films and fabrication of microstructured PPy. In addition to the variability in the feature morphology, the feature density was relatively low and irregular. This low density is likely due to the vertical orientation of the electrodes. When the gas bubbles are formed on the WE, the buoyancy force often overcomes the electrostatic force keeping them attached to the electrode. Figure 7.2(a) highlights this observation where higher feature densities were observed at the bottom tip of the WE along the thickness of the sheet.

7.2.2   Horizontal electrode configuration

The observation of increased feature density at the WE tip inspired a modification to the electrode orientation to ensure as many gas bubbles were maintained at the WE surface. The WE and CE were bent at 90° to produce horizontal parallel

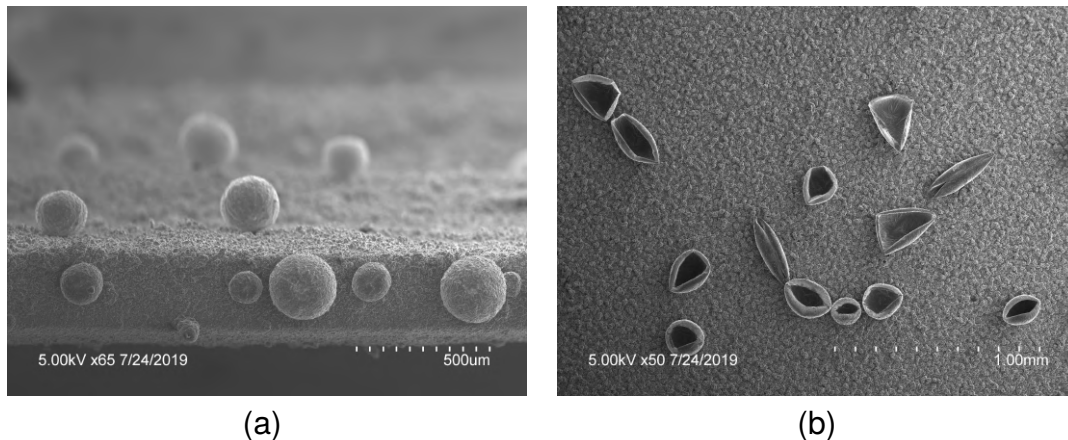(a)   (b)

Figure 7.2: The number of potential cycles applied informed the morphology of polypyrrole (PPy) microstructures produced during soft-template polymerization where following gas bubble production a polymerization potential range from 0 V to 1.2 V applied for 7 cycles produced closed PPy microspheres (a) compared to 2 cycles produced open bowl-like structures (b).
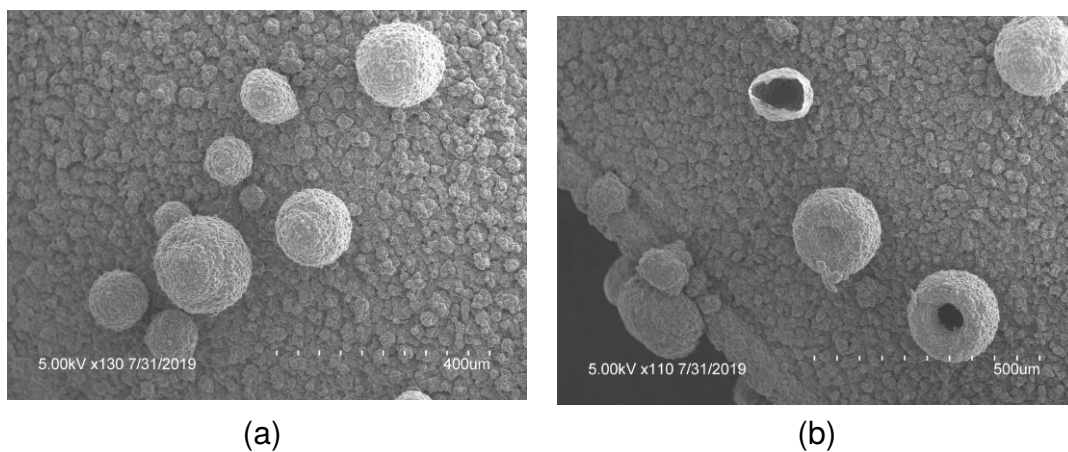

(a)   (b)

Figure 7.3: SEM images of a microstructure polypyrrole film demonstrated the variability in morphologies produced using a more narrow template generation potential range with a wider polymerization potential range of 0 V to 1.4 V where both close microspheres (a) and open bowl-like (b) structures were produced.

plates (fig. 7.1). In this configuration to produce microstructured films the WE is positioned 5 mm above the CE. Gas bubble creation occurs during the negative potential range. Due to the improved adhesion to the WE, instances of bubble coalescence would occur creating a contact between the WE and CE, as a result the negative potential range was appended at −1.1 V rather than the −1.6 V used in the vertical electrode process. Additionally, this coalescence resulted in larger bubbles forming that were undesirable for the production of microstructured films. Through the application of the horizontal electrode configuration and appended negative potential range, features of higher density and more uniform distribution were fabricated as shown in fig. 7.4. These films exhibited features in a similar size and shape to the vertical electrode method in the approximate range of 100 μm to 200 μm, however, an additional group of features was observed as a result of the horizontal configuration. This new class of features shown in fig. 7.5 have diameters in the range of 25 μm to 50 μm and are produced at the CE during the positive potential range. As a result, the microstructured films have a hierarchical structure where the larger templates produced during the negative potential range are polymerized first, and then can be used as attachment points for the smaller bubbles produced during the positive potential range. These smaller bubbles are likely produced due to the hydrolysis of water at the end of the positive potential range. The distribution of PPy microstructure feature size examined manually through the measurement of optical images similar to that in fig. 7.4(b). A summary of the feature distribution is shown in fig. 7.6 demonstrating a bimodal distribution with peaks centred around 10 μm to 30 μm and 90 μm to 110 μm. Also exhibited in the histogram is the existence of larger features of approximately 200 μm demonstrating the need for further control of feature size. However, the horizontal electrode configuration yielded improved feature density and consistency with the added benefit of a smaller regime of features further increasing the surface are of the microstructured films. Finally, the

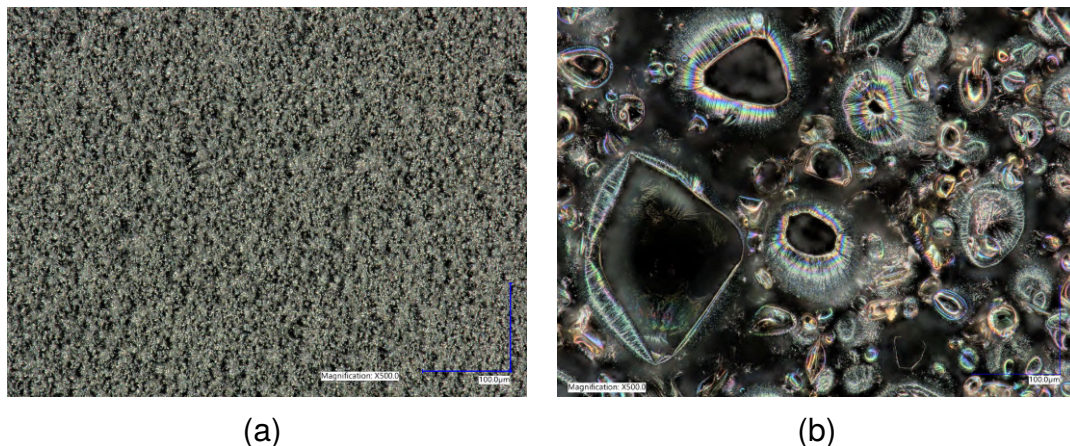(a)   (b)

Figure 7.4: The improved density of polypyrrole microstructures produced using the newly developed horizontal electrode configuration is shown by optical microscopy images of flat (a) and microstructured (b) polyprrole films at 500× magnification where the image shown in (b) is representative of the images used for feature size identification in fig. 7.6.

conductivity of flat and microstructured films were measured to identify the effect of the polymerization process on electrical conductivity. The 4-point probe resistance measurements demonstrated an average sheet resistance of $(408.56 \pm 40.21)\,\Omega/\square$ for flat films and $(252.30 \pm 49.72)\,\Omega/\square$ for microstructured films. This reduction in sheet resistance can be attributed to the increased surface area of the films fabricated by soft-template polymerization (Xiao et al., 2007).

7.2.3   Soft-template polymerization on polyprrole composite

PPy microstructures were deposited onto PPy-BEMA-PEGMA composite cast films or films fabricated by vat polymerization to assess the potential of the soft-template polymerization process to improve the electrochemical performance of the composite material. Prior to electropolymerization, the printed films were affixed to stainless steel electrodes using conductive silver epoxy. The exposed stainless steel and silver epoxy were then covered with polyamide tape to limit any contribution of these components during the electropolymerization reaction. Initial attempts to deposit

(a)   (b)

Figure 7.5: Optical microscopy images at (a) 250× and (b) 300×, demonstrate the hierarchical nature of microstructured polypyrrole films produced in the horizontal electrode configuration where stacked microspheres are observed at two distinct diameter ranges providing increased density of doping sites and capacity.
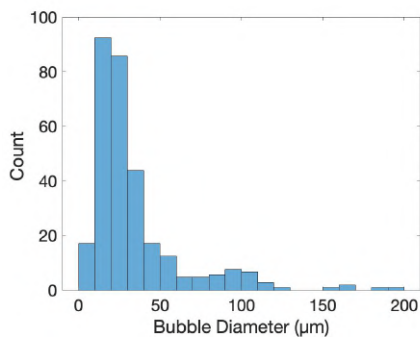

Figure 7.6: The bimodal distribution of polypyrrole feature size produced during soft-template polymerization using the horizontal electrode configuration is represented by a histogram where the feature size data was collected from four separate optical microscopy images totalling 1 mm^2.

hierarchical PPy structures via soft-template polymerization involved cast, and bulk cured PPy-BEMA-PEGMA films using the standard resin formulation. Due to poor conductivity of these samples, only a low number of features were able to be produced and the process was unreliable (appendix A). To examine if an increase in electrical conductivity would aid in the deposition of PPy microstructures, PPy-BEMA-PEGMA cast films were sputter coated with gold to create a high conductivity film on top of the PPy-BEMA-PEGMA composite. This test yielded promising results with a high density distribution of PPy micro-spheres along with larger, hollow tube structures (appendix A). Successful results with the gold coated PPy-BEMA-PEGMA films provided the motivation behind the development of the PPy-CNT dispersion process detailed in chapter 6 to enabled the deposition of hierarchical PPy structures directly on fabricated 3D structures without the need for additional coating procedures that may not be suitable for all geometries.

Following successful fabrication of PPy-BEMA-PEGMA-CNT composites with improved electrical conductivity, this formulation was implemented as a substrate for soft-template polymerization of PPy microstructures. For the formation of flat PPy films on printed PPy-BEMA-PEGMA-CNT films, the WE was placed in the lower position and a potential of 0 V to 1.2 V was applied for 4 cycles. For the formation of microstructures on printed films, the WE electrode was placed in the upper position and 2 cycles from 0 V to 1.2 V were applied to create an initial PPy thin film, this was followed by the application of 2 cycles from –0.6 V to –1.1 V to generate gas bubbles on the WE. Finally, 2 cycles from 0 V to 1.2 V were applied to initiate polymerization around the gas bubble soft-templates. In total 4 positive polymerization cycles were applied for both flat films and microstructured films to obtain similar weights of PPy deposited. Figure 7.7 provides optical microscopy images of the printed films in three states: (a) as-printed, (b) with a flat PPy film deposited, and (c) with microstructured PPy deposited. The as-printed film in fig. 7.7(a) exhibits a flat

PPy-BEMA-PEGMA structure with the bright spots indicating an even distribution of silver particles, a by-product of the Py photopolymerization reaction. These silver particles signify the successful polymerization of Py as well as contributing to improving the electrical conductivity of the printed samples (Cullen and Price, 2018). Figure 7.7(b) shows a thin PPy film deposited on the surface of the printed film by an even smooth black coating, some silver particles remain visible likely due to the thin PPy coating being insufficient to cover the roughness attributed to the larger silver particles. Future studies will investigate the thickness of these films as well as optimizing the deposition parameters. Finally, fig. 7.7(c) shows the microstructured surface as a result of the soft-template polymerization, both open bowl-like, and closed bubble-like features are visible with similar silver particles visible as seen in the flat PPy films. Closer examination of the PPy-coated PPy-BEMA-PEGMA films was conducted via SEM. Figure 7.8(a) shows the surface of a flat PPy film deposited on the PPy-BEMA-PEGMA which revealed the expected distribution of silver particles but also exhibited a wrinkled surface which can be attributed to a known shrinkage effect of the PPy-BEMA-PEGMA composite (Atai et al., 2007; Cook, Beech, and Tyas, 1985). Figure 7.8(b) and (c) provide further inspection of the surface morphology of microstructured PPy deposited on the PPy-BEMA-PEGMA composite, with some features on the scale of $100\,\mu m$ representing templates produced during the negative potential range and features in the proximity of $25\,\mu m$ associated with the templates created during the positive potential range. These structures exhibit similar size and morphology to those features previously produced on flat stainless steel electrodes. However, features deposited on the PPy-BEMA-PEGMA composite are lower density with a less uniform spatial distribution. These changes in feature distribution can likely be attributed to the lower conductivity of the composite compared to the stainless steel electrodes creating regions of preferred polymerization on the surface of the composite film. Further development
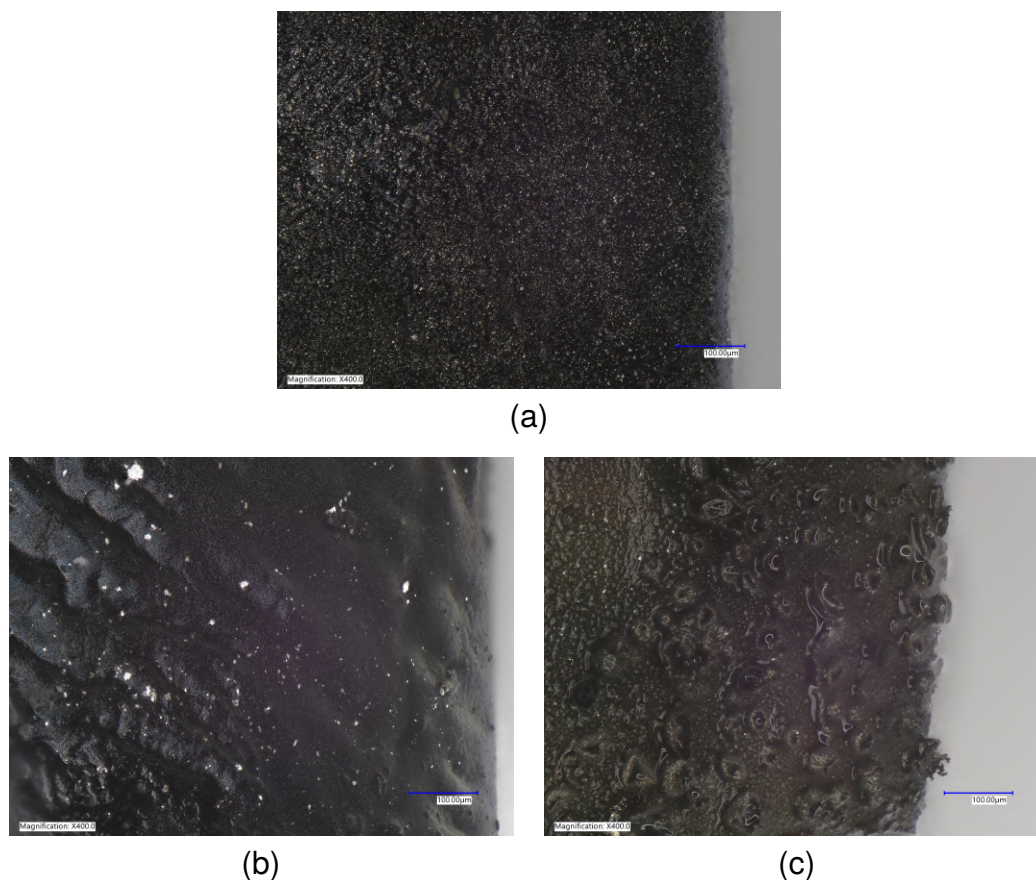
(a)

(b)   (c)

Figure 7.7: Optical microscopy images (at 400×) of vat polymerized PPy-BEMA-PEGMA-CNT films as-printed (a), and following post-hoc electrochemical deposition of polypyrrole flat film (b), and microstructured film using the soft-template polymerization method (c).

of the PPy-BEMA-PEGMA composite formulation should improve the density and uniformity of deposited hierarchical structures.

The electrochemical performance of the composite materials was tested through the analysis of the CV response of PPy-BEMA-PEGMA 3D printed films deposited either with a flat PPy film or microstructured PPy features. CV was conducted on printed PPy-BEMA-PEGMA-CNT composite films with 0.043 % (w/w) PPy-CNT with both flat and microstructured PPy films deposited on them. Each film was subjected to a potential range from –1 V to 1.5 V, compared to Ag-AgCl, at a scan rate of 20 mV $\cdot$ s^{-1} for 5 cycles. Results of the CV testing are shown in fig. 7.9 and

(a)

(b)

(c)
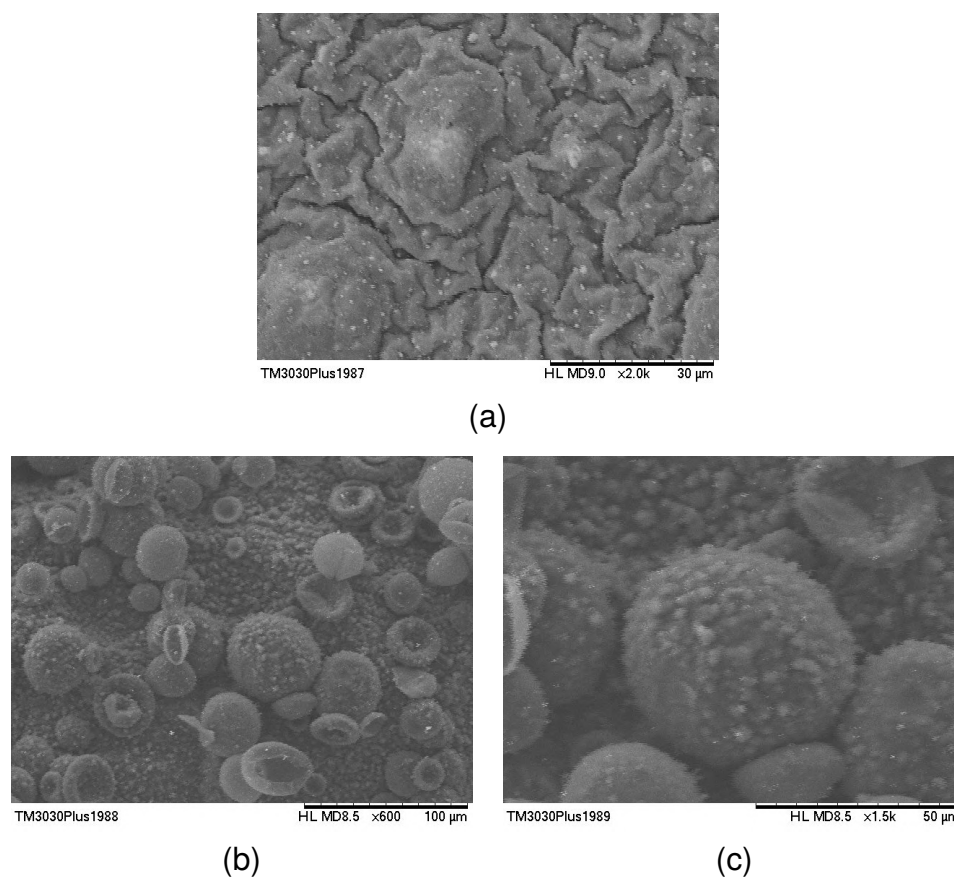
Figure 7.8: SEM images of vat polymerized PPy-CNT-BEMA-PEGMA films follow-
ing post hoc electrochemical deposition of polypyrrole flat film (a), and microstruc-
tured film using the soft-template polymerization method at 600× (b) and 1500× (c).

show relatively stable performance over the short cycle range. The microstructured film displays peaks with greater magnitude both in oxidation and reduction demonstrating improved doping capacity compared to the flat film. This is likely due to the increased surface area provided by the microstructured features providing an increased number and more accessible doping sites (Bajpai, He, and Dai, 2004). These results demonstrate that there is potential for these films to have improved performance in sensing applications (Wadhwa, Lagenaur, and Cui, 2006). While an effort was made to maintain identical polymerization conditions for both flat and microstructured PPy deposition to achieve similar mass of each film, there may be small variations in the mass of PPy deposited. The low weight of PPy deposited introduces difficulties in accurately measuring this mass, as such the CV results are not normalized with respect to mass but each film has the same deposition area available. However, small deviations in the mass of deposited PPy are not expected to have such significant contributions such that they could lead to the observed large differences in the electrochemical responses, thus suggesting the microstructures could have significant impact on the device performance. The deposition of hierarchical PPy microstructures on 3D structures unlocks the potential for improved performance of PPy-based devices for drug delivery, and sensing applications (Akkermans et al., 2016; Liubchak et al., 2020).
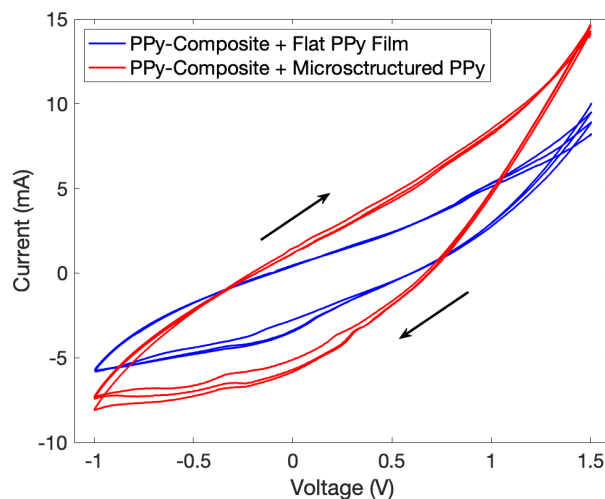
Figure 7.9: The cyclic voltammetry response of vat polymerized PPy-BEMA-PEGMA-CNT composite films deposited with flat PPy and microstructured PPy films show an increased electrochemical response for microstructured films.

7.3 Chapter summary

This study provided the development of a soft-template polymerization process for the deposition of PPy microstructures. The development of a horizontal electrode configuration allowed for the production of gas bubble templates in the $100\,\mu m$ range during the negative CV potential and also capitalized on the gas bubble templates produced during the positive potential range to create smaller scale $25\,\mu m$ PPy features. The fabrication of flat and microstructured PPy films on stainless steel electrodes demonstrated lower surface resistivity in the microstructured films and provided the basis for application of the deposition process to accommodate 3D printed PPy-BEMA-PEGMA composite substrates. Initial attempts to deposit hierarchical PPy structures on PPy-BEMA-PEGMA films yielded poor results due to the low electrical conductivity of the material. The integration of PPy functionalized CNTs into the PPy-BEMA-PEGMA composite improved the electrical conductivity, and enabled the first instance of PPy microstructure deposition on a PPy composite substrate fabricated by vat polymerization. PPy-BEMA-PEGMA films demonstrated

improved electrochemical performance with microstructured PPy films compared to

flat PPy films enabling future investigation into the effect of hierarchical structures

on 3D PPy device performance.

7.4 References

Akkermans, Onno, Mitch Spronck, Theo Kluskens, Fred Offerein, Ketie Saralidze, Jos Aarts, Pegah Keshaniyan, Erik Steen Redeker, Hanne Diliën, Bart van Grinsven, and Thomas J. Cleij (2016). "Application of electrodeposited piezo-resistive polypyrrole for a pressure-sensitive bruxism sensor." In: *physica status solidi (a)* 213.6, pp. 1505–1509.

Atai, Mohammad, Mehdi Ahmadi, Samal Babanzadeh, and David C. Watts (2007). In: *Dental Materials* 23.8, pp. 1030–1041.

Bajpai, Vardhan, Pingang He, and Liming Dai (2004). "Conducting-Polymer Microcontainers: Controlled Syntheses and Potential Applications." In: *Advanced Functional Materials* 14.2.

Cook, Wayne D., Derrick R. Beech, and Martin J. Tyas (1985). "Structure and properties of methaerylate based dental restorative materials." In: *Biomaterials* 6.6, pp. 362–368.

Cullen, Andrew T. and Aaron D. Price (2018). "Digital light processing for the fabrication of 3D intrinsically conductive polymer structures." In: *Synthetic Metals* 235.

Liubchak, Iryna, Matthew T. Lawrence, F. Benjamin Holness, and Aaron D. Price (2020). "Soft template electropolymerization of polypyrrole for improved ph-induced drug delivery." In: *International Journal of Molecular Sciences* 21.21.

Qu, Liangti and Gaoquan Shi (2004). "Hollow microstructures of polypyrrole doped by poly(styrene sulfonic acid)." In: *Journal of Polymer Science, Part A: Polymer Chemistry* 42.13.

Qu, Liangti, Gaoquan Shi, Feng'en Chen, and Jiaxin Zhang (2003). "Electrochemical Growth of Polypyrrole Microcontainers." In: *Macromolecules* 36, pp. 1063–1067.

Qu, Liangti, Gaoquan Shi, Jinying Yuan, Gaoyi Han, and Feng'en Chen (2004). "Preparation of polypyrrole microstructures by direct electrochemical oxidation of pyrrole in an aqueous solution of camphorsulfonic acid." In: *Journal of Electroanalytical Chemistry* 561 (SUPPL. 1).

Wadhwa, Reecha, Carl F. Lagenaur, and Xinyan Tracy Cui (2006). "Electrochemically controlled release of dexamethasone from conducting polymer polypyrrole coated electrode." In: *Journal of Controlled Release* 110.3.

Xiao, Yinghong, Jianfei Che, Chang Ming Li, Chang Q. Sun, Yek T. Chua, Vee S. Lee, and John H.T. Luong (2007). "Preparation of nano-tentacle polypyrrole with pseudo-molecular template for ATP incorporation." In: *Journal of Biomedical Materials Research Part A* 80A.4, pp. 925–931.

Chapter 8

Concluding remarks

8.1   Summary of conclusions

This thesis explored the issues surrounding the advancement of the fabrication methods currently developed for EAP transducers and investigate techniques for improving performance of these devices. The experience gained/knowledge ascertained through these activities has prompted the following conclusions:

1. An improved additive manufacturing approach for the fabrication of 3D passive support structures for use in EAP devices was achieved through the development of a DIW process with carbomer support gel to produced high resolution PDMS structures with complex geometries and true 3D overhanging features.

2. Successful fabrication of 3D CP transducers were achieved by adaptation of the DIW process for a custom PDMS-CNT formulation which was implemented to produce complex 3D structures of the conductive elastomeric composite and the application of tubular strain sensors demonstrated the potential of this process to fabricate complex structures for sensing and use as compliant electrodes in 3D CP devices.

3. Improvements to the electrical properties of a PPy-BEMA-PEGMA photosensitive resin formulation were achieved through optimization of photoinitiator selection and preparation procedure. Further improvements were achieved through the successful introduction of PPy functionalized CNTs to the PPy-BEMA-PEGMA formulation.

4. Finally, first instance of hierarchical PPy microstructures deposited on vat polymerized PPy-BEMA-PEGMA-CNT composite materials to demonstrate an improved electrochemical response of devices was reported by the post hoc deposition of hierarchical features by soft-template polymerization.

8.2   Summary of contributions

The most significant research contributions presented in this thesis are summarized as follows:

- Improvements made to the AM system and process settings enabled the fabrication of vascular-like structures that have applications in fluidics and as passive layers in 3D EAP actuators.

- *Development of 3D tubular piezoresistive PDMS-CNT sensors.* The first study demonstrating flexible, 3D PDMS-CNT strain sensor fabricated by DIW.

- *Improvement of PPy-BEMA-PEGMA composite electrical properties.* Developed an improved PPy-BEMA-PEGMA resin preparation process and incorporated PPy functionalized carbon nanotubes to regain the electrical conductivity lost due to the passive copolymers required for mechanical stability.

- *Developed a process for the post hoc electrochemical deposition of PPy onto 3D printed PPy-BEMA-PEGMA structures.* Flat films were deposited onto the surface of 3D printed PPy-BEMA-PEGMA films to improve the electrochemical performance of the device. Further improvements were made by applying the technique soft-template electropolymerization to create micro-spherical structures on the printed CP surface.

8.3   Recommendations for future research

The DIW process of the PDMS Sylgard 184 described in this work improved upon the surface quality of printed structures however instances of wall defects for more complex geometries suggest investigation of alternative custom PDMS formulations be investigated. The modification of the curing initiation is worthy of investigation, in situ UV cross-linking of a photosensitive PDMS formulation could reduce post-extrusion material flow and enable the fabrication of more complex structures. Finally, the deposition of high-quality PEDOT:PSS films on a 3D PDMS substrates is a complex process that requires further development.

The development of a PDMS-CNT composite for DIW of 3D structures established a path towards complex 3D integrated transducers for fluidic applications. Future studies should investigate the attachment of high-resolution, compliant electrodes to allow for multi-channel measurements of the piezoresistive response and the modelling of this response in 3 dimensions. Additionally the flexible, and conductive properties of the 3D PDMS-CNT structures are a promising candidate as substrates for the deposition of CP structures and the fabrication of 3D CP transducers.

The integration of PPy functionalized CNTs into the PPy-BEMA-PEGMA resin formulation resulted in an improved electrical conductivity sufficient to enable post

hoc deposition of PPy microstructures. However, casting of tensile specimen in moulds exhibited under-curing effects associated with the UV absorbance of CNTs. While this absorbance inhibited curing for thicker samples it may allow for the fabrication of vat polymerized samples with improved resolution by limiting the over-exposure of resin surrounding the exposed regions. Detailed depth of cure studies will elucidate the impact of CNT UV absorbance on the vat polymerization process. Finally, exploratory work identified onium salts as a potential addition to the PPy-BEMA-PEGMA formulation to create a dual-component photoinitiation system. A future study employing real-time FTIR spectroscopy throughout the polymerization reaction should improve understanding of the reaction kinetics for the PPy and BEMA-PEGMA polymerization composite as a function of the photoinitiation system.

The development of the soft-template polymerization process for the post hoc bulk deposition of hierarchical PPy structures on vat polymerized PPy-BEMA-PEGMA-CNT films unlocks the potential for the fabrication of novel 3D PPy-based devices. Future studies should further investigate how the ability to create 3D PPy-composite substrates can be leveraged to inform the development of gas bubble nucleation sites and improve control of the formation of hierarchical PPy structures. Further, the volume expansion effects during redox doping of these newly developed composite materials should be explored in greater depth to inform future 3D PPy device design.

Appendices

Appendix A

Development of PPy-BEMA-PEGMA Formulation
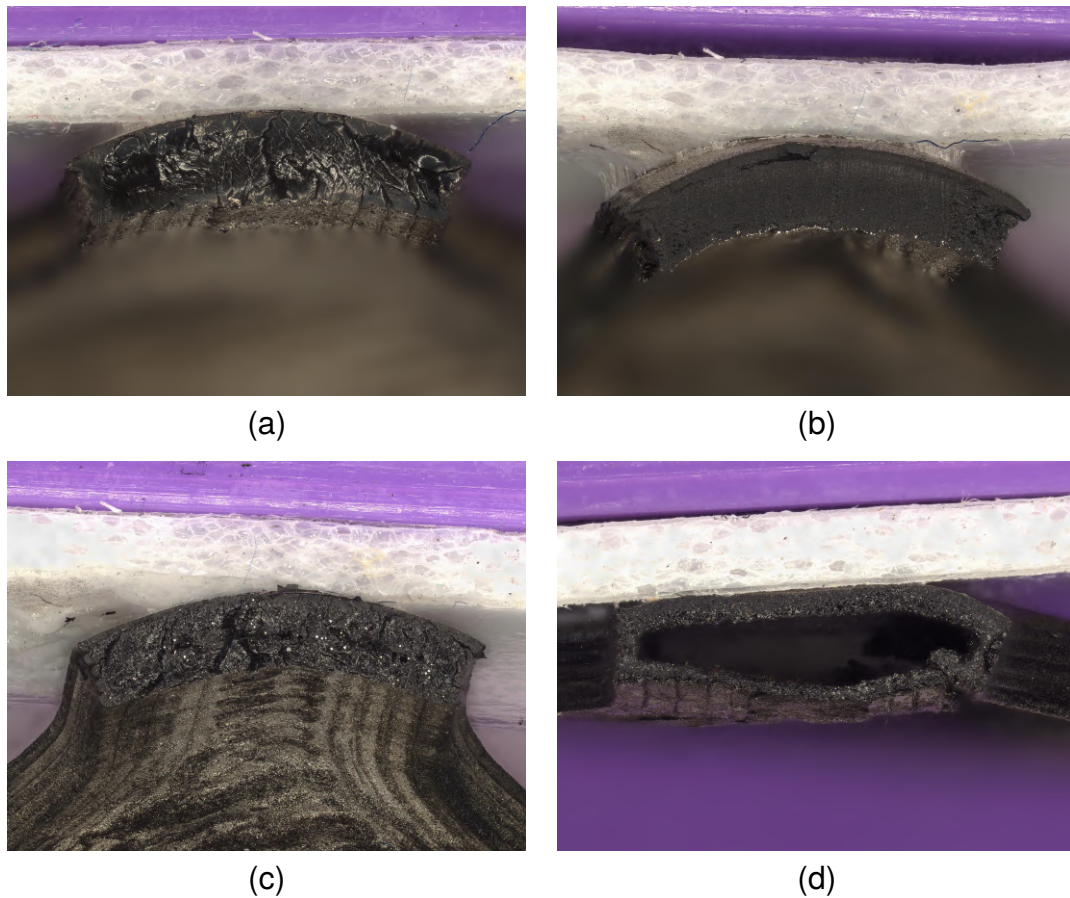
Figure A.1: Curing of PPy-BEMA-PEGMA cast tensile specimen exhibited reduction in cross-sectional area due to UV absorption at CNT concentrations of (a) 0 % (w/w), (b) 0.043 % (w/w), (c) 0.129 % (w/w), and (d) 0.389 % (w/w).
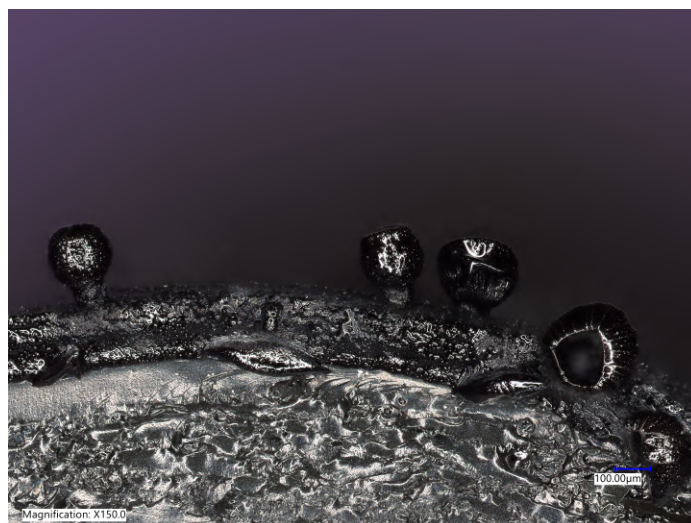
(a)

(b)
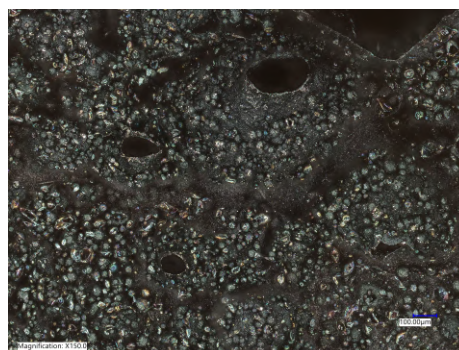
(c)

Figure A.2:   Optical microscopy images of cast PPy-BEMA-PEGMA films following post-hoc electrochemical deposition of microstructures on untreated PPy-BEMA-PEGMA film (a), and gold sputter coated PPy-BEMA-PEGMA at 50x (b) and 150x (c).

Appendix B

Copyright Permissions

The following pages provide confirmation of acquired copyright permissions for the appropriate referenced figures in this thesis. Table B.1 summarizes the copyright information, followed by excerpts of the relevant documentation. Permissions are presented in the order they appear in the thesis. Note that copyright permission from Open-Access publications is provided through the Creative Commons license (CCBY).

Table B.1: Summary of copyright permission information

Thesis Figure	Reference Title	Reference Figure	First Author	Publication	Publisher	License Number
2.1	Dispersion and functionalization of carbon nanotubes for polymer-based nanocomposites: A review	Figure 17	P. Ma	Composites: Part A	Elsevier	1288413-1
2.3	Evaluation of porous polydimethylsiloxane/carbon nanotubes (PDMS/ CNTs) nanocomposites as piezoresistive sensor materials	Figure 3	T. Michel	Microsystems Technologies	Springer	5424920244569
2.5	The chemical structure diagrams of a group conjugated polymers	Figure 2	S. Bhadra	Progress in Polymer Science	Elsevier	5424920572342
2.8	Thin film free-standing PEDOT:PSS/SU8 bilayer microactuators	Figure 2	S. Taccola	J. Micromech. Microeng	IOP	1288422-1
2.10	Fabrication of 3D conjugated polymer structures via vat polymerization additive manufacturing	Figure 13	A.T. Cullen	Smart Materials and Structures	IOP	1288494-1
2.11	Condensing Vapor Phase Polymerization (CVPP) of Electrochemically Capacitive and Stable Polypyrrole Microtubes	Figure 2	L.M. Santino	Applied Materials & Interfaces	ACS	N/A
2.12	Preparation of polypyrrole microstructures by direct electrochemical oxidation of pyrrole in an aqueous solution of camphorsulfonic acid	Figure 2	L. Qu	Electroanalytical Chemistry	Elsevier	5425130947109
2.13	A one-step electrodeposition of homogeneous and vertically aligned nanotubes with parahydrophobic properties	Figure 3	T. Darmanin	Materials Chemistry A	RSC	1288546-1

136

Figure B.1: Copyright permission for "Dispersion and functionalization of carbon nanotubes for polymer-based nanocomposites: A review" (fig. 2.1).

Figure B.2: Copyright permission for "Evaluation of porous polydimethylsiloxane/carbon nanotubes (PDMS/ CNTs) nanocomposites as piezoresistive sensor materials" (fig. 2.3).
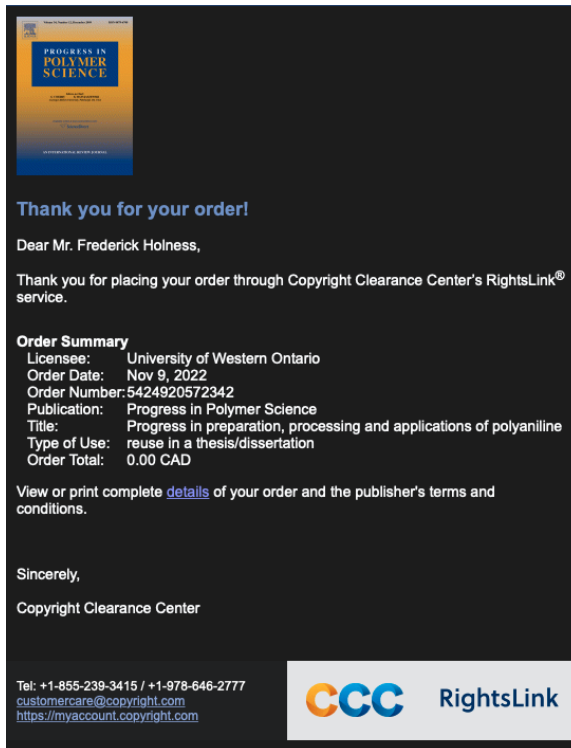
Figure B.3: Copyright permission for "The chemical structure diagrams of a group conjugated polymers" (fig. 2.5).

Figure B.4: Copyright permission for "Thin film free-standing PEDOT:PSS/SU8 bilayer microactuators" (fig. 2.8).

Order Number: 1288494
Order Date: 09 Nov 2022

Payment Information

Frederick Holness   **Billing Address:**   **Customer Location:**

Order Details

1. Smart Materials and Structures

Billing Status:
Open

Print License

Order License ID	1288494-1	**Type of use**	Republish in a thesis/dissert...
Order detail status	Completed	**Publisher**	IOP Publishing
ISSN	1361-665X	**Portion**	Image/photo/illustration

0.00 CAD
Republication Permission

View Details

Publisher Terms and Conditions

Total Items: 1

Subtotal: 0.00 CAD
Order Total: 0.00 CAD

Figure B.5: Copyright permission for "Fabrication of 3D conjugated polymer structures via vat polymerization additive manufacturing" (fig. 2.10).

ACS Publications
Most Trusted. Most Cited. Most Read.

Condensing Vapor Phase Polymerization (CVPP) of Electrochemically Capacitive and Stable Polypyrrole Microtubes
Author: Luciano M. Santino, Erica Hwang, Yifan Diao, et al
Publication: Applied Materials
Publisher: American Chemical Society
Date: Nov 1, 2017

Copyright © 2017, American Chemical Society

PERMISSION/LICENSE IS GRANTED FOR YOUR ORDER AT NO CHARGE

Figure B.6: Copyright permission for "Condensing vapor phase Ppolymerization (CVPP) of electrochemically capacitive and stable polypyrrole microtubes" (fig. 2.11).
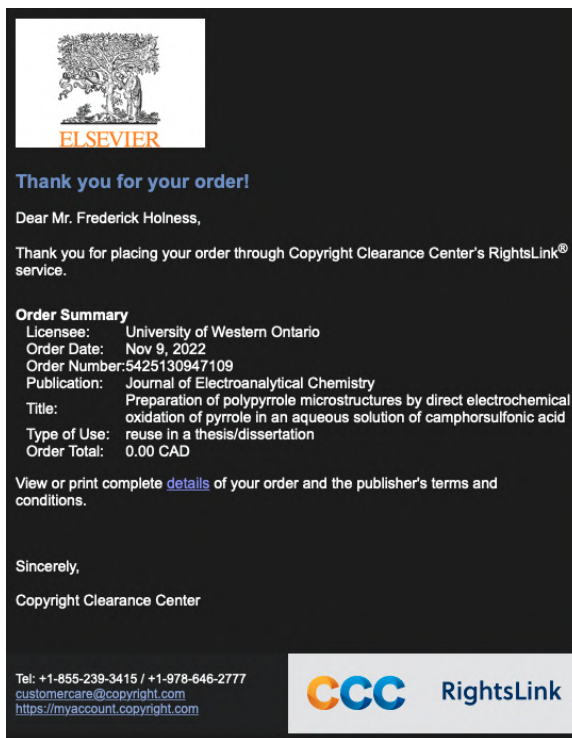
Figure B.7: Copyright permission for "Preparation of polypyrrole microstructures by direct electrochemical oxidation of pyrrole in an aqueous solution of camphorsulfonic acid" (fig. 2.12).
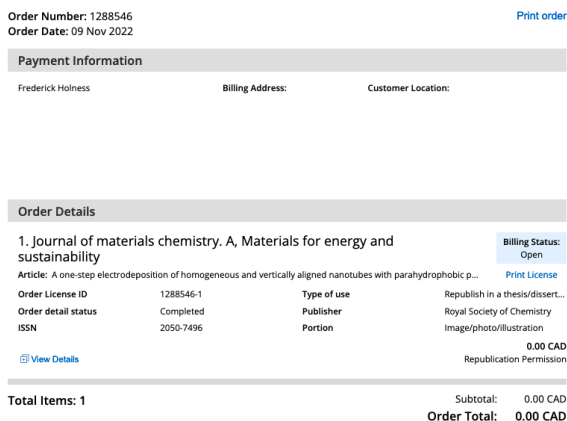

Figure B.8: Copyright permission for "A one-step electrodeposition of homogeneous and vertically aligned nanotubes with parahydrophobic properties" (fig. 2.13).

Curriculum Vitæ

Name: Frederick Benjamin Holness

Post-Secondary Education and Degrees: The University of Western Ontario
London, Ontario, Canada
2011 – 2015 B.E.Sc.
2015 – 2017 M.E.Sc.

Honours and Awards: Ontario Graduate Scholarship
2015 – 2016 (declined)
2020 – 2021

Natural Sciences and Engineering Research Council of Canada
Canadian Graduate Scholarship - Masters Program
2015 – 2016

Canadian Graduate Scholarship - Doctoral Program
2017 – 2020

Related Work Experience: Teaching Assistant
The University of Western Ontario
MME 4450: Control Systems: Theory and Practice
2015, 2016, 2017, 2018, 2019
MME 3350: System Modelling and Control
2016, 2017
MSE 3380: Mechanical Components Design for Mechatronic Systems
2018, 2019, 2020
MME 9612: Finite Element Methods
2019, 2020
MME 2259: Product Design and Development
2020
MME 9521: Systems and Control
2021

Elected Positions: MME Graduate Society - President
2018 – 2020

Journal Articles

Liubchak, Iryna, Matthew T. Lawrence, F. Benjamin Holness, and Aaron D. Price (2020). "Soft template electropolymerization of polypyrrole for improved ph-induced drug delivery." In: *International Journal of Molecular Sciences* 21.21.

Gao, Xuejie, Qian Sun, Xiaofei Yang, Jianneng Liang, Alicia Koo, Weihan Li, Jianwen Liang, Jiwei Wang, Ruying Li, Frederick Benjamin Holness, Aaron David Price, Songlin Yang, Tsun-Kong Sham, and Xueliang Sun (Feb. 2019). "Toward a remarkable Li-S battery via 3D printing." In: *Nano Energy* 56, pp. 595–603.

Holness, F Benjamin and Aaron D Price (Jan. 2018). "Direct ink writing of 3D conductive polyaniline structures and rheological modelling." In: *Smart Materials and Structures* 27, p. 015006.

Wang, Jiwei, Qian Sun, Xuejie Gao, Changhong Wang, Weihan Li, Frederick Benjamin Holness, Matthew Zheng, Ruying Li, Aaron David Price, Xuhui Sun, Tsun-Kong Sham, and Xueliang Sun (Nov. 2018). "Toward High Areal Energy and Power Density Electrode for Li-Ion Batteries via Optimized 3D Printing Approach." In: *ACS Applied Materials & Interfaces* 10.46, pp. 39794–39801.

Micolini, Carolina, Frederick Benjamin Holness, James A. Johnson, and Aaron David Price (Nov. 2017). "Assessment of Embedded Conjugated Polymer Sensor Arrays for Potential Load Transmission Measurement in Orthopaedic Implants." In: *Sensors* 17.12, p. 2768.

Conference Proceedings

Holness, F. Benjamin, Gerardo Patino Guillen, and Aaron D. Price (Mar. 2021). "Hierarchical electroactive polypyrrole-carbon nanotube composite microstructures by high resolution vat polymerization and soft template electropolymerization." In: *Electroactive Polymer Actuators and Devices (EAPAD) XXIII* 11587, p. 1158711.

Liubchak, Iryna, Matthew T. Lawrence, F. Benjamin Holness, and Aaron D. Price (Mar. 2021). "Soft-template electrochemical polymerization for the advancement of electroactive polymer drug delivery systems." In: *Electroactive Polymer Actuators and Devices (EAPAD) XXIII* 11587, pp. 1158712–1158712–7.

Holness, F. B., Tamie L. Poepping, and Aaron D. Price (Apr. 2019). In: *Electroactive Polymer Actuators and Devices (EAPAD) XXI* 10966, p. 1096606.

Holness, F. Benjamin and Aaron D. Price (Apr. 2017). "Design and fabrication of conductive polyaniline transducers via computer controlled direct ink writing." In: *Electroactive Polymer Actuators and Devices (EAPAD) 2017*, 101632O–101632O-8.

Micolini, Carolina, F. B. Holness, James A. Johnson, and Aaron D. Price (Apr. 2017). "Conductive polymer sensor arrays for smart orthopaedic implants." In: *Nanosensors, Biosensors, Info-Tech Sensors and 3D Systems 2017*, pp. 101670D–101670D-7.

Holness, F. Benjamin and Aaron D. Price (Apr. 2016). "Robotic extrusion processes for direct ink writing of 3D conductive polyaniline structures." In: *Electroactive Polymer Actuators and Devices (EAPAD) 2016*, 97981G–97981G-8.